Geometry does matter^2

Janbaz, Shahram

DOI
10.4233/uuid:f6d25575-d312-4c26-8560-2b9c2572d135

Publication date
2018

Document Version
Final published version

Citation (APA)
Janbaz, S. (2018). *Geometry does matter^2*. [Dissertation (TU Delft), Delft University of Technology]. https://doi.org/10.4233/uuid:f6d25575-d312-4c26-8560-2b9c2572d135

Geometry does matter^2

Geometry does matter^2

Proefschrift

ter verkrijging van de graad van doctor
aan de Technische Universiteit Delft,
op gezag van de Rector Magnificus Prof. dr. ir. T.H.J.J. van der Hagen,
voorzitter van het College voor Promoties,
in het openbaar te verdedigen op
donderdag 29 november 2018 om 15:00 uur

door

Shahram Janbaz

Master of Science in Mechanical Engineering (Applied Design),
Islamic Azad University, South Tehran Branch, Teheran, Iran.
geboren te Teheran, Iran.

Dit proefschrift is goedgekeurd door de promotor:
Prof. dr. A.A. Zadpoor

Samenstelling promotiecommissie:

Rector Magnificus	Technische Universiteit Delft, voorzitter
Prof. dr. A.A. Zadpoor	Technische Universiteit Delft, promotor

Onafhankelijke leden:

Prof.dr. F. Scarpa	University of Bristol, United Kingdom
Prof.dr.ir. P. Breedveld	Technische Universiteit Delft
Prof.dr.ir. J.L. Herder	Technische Universiteit Delft
Prof.dr.ir. L.J. Sluys	Technische Universiteit Delft
Prof.dr.ir. S. van der Zwaag	Technische Universiteit Delft
Dr. M.M.G. Kamperman	Wageningen University & Research

ISBN 978-94-6323-425-2
Een digitale versie van dit proefschrift is beschikbaar op
http://repository.tudelft.nl/.

Table of Contents

Chapter 1

Introduction: rationality in metamaterial design

The unique properties available in bio-systems are inspiring for designing synthetic materials with exceptional properties. The unusual properties in such systems is mainly related to their specific (geometrical) design rather than their chemical composition. Several classes of properties such as wave-like, structural, and bio-related properties are examples of the properties that could be devised by rationally designing such designer materials.

Geometry to implement functionality

Discovering the underlying designs of the biological materials with exceptional properties might provide the insights required for developing engineered materials with similar properties. There are numerous examples of unusual physical and mechanical properties in nature including the structural colors of insects [1,2], light scattering in butterfly wings [3], dry adhesive properties of gecko [4], superhydrophobicity in lotus (self-cleaning) [5], anti-fouling properties of sharkskin [6], shock absorption in woodpecker skull [7], and the zero Poisson's ratio of cork [8]. Geometry rather than the composition plays the primary role in creating such exceptional properties. In addition, there are instances in nature that material changes its geometry in response to external stimuli [9]. Such evolutions in cellular and extracellular matrix of living tissues could be mimicked by synthetic materials in order to imitate the transformations observed in nature, thereby creating novel functionalities [10].

Multiple approaches have been proposed for using geometrical design as a tool to achieve bio-inspired or otherwise interesting properties. In this thesis, I will be primarily focusing on two specific approaches including 1. design of soft periodic cellular structures in which geometry (in some cases together with the spatial distribution of material properties) defines the thresholds and patterns of instability [11] and 2. origami-based designs [12,13].

Soft cellular matter that is based on periodic arrangement of repeating unit cells could be used for design of soft metamaterials in which the thresholds and patterns of instability tune the mechanical behavior of the materials and the resulting functionalities [11,14]. Geometrical features (i.e., void geometry) might be used to harness the microscopic and macroscopic instabilities in such soft structures and, therefore, adjust the mechanical behavior of cellular structures. Soft periodic mechanical metamaterials are useful in the field of soft robotics as well as in other areas such as manipulation of wave-like phenomena [15]. To date, geometry has been the primary tool to tune the mechanical properties of soft cellular matter [14] including the critical values of strains and stresses [11] and instability patterns (i.e., "*buckling-modes*") [11]. Design-driven tuning of the above-mentioned phenomena enables engineers to program specific functions in soft robotic components such as soft actuators. Although a few previous studies have already demonstrated the effects of geometry on the critical behavior of soft cellular mater, the level of tuning achieved has been limited to date. I therefore aimed to combine geometry with other contributing factors such as the spatial distribution of material properties to achieve the ultimate tunability in the instability behavior of soft cellular matter. Ultimate tunability also requires decoupling the stiffness, critical values, and instability patterns as much as possible so as to facilitate creation of metamaterials with the desired properties.

Origami ("the ancient Japanese art of paper folding" [16]) is the other geometry-based approach used in this thesis to create materials with unprecedented properties. This approach is especially useful for materials in which full access to the surface is essential for (bio-)functionalization purposes. Starting from a flat shape means that the surface of the material could, for example, be nano-patterned or decorated with electronic devices using already available technologies such as electron beam nano-lithography or organic electronic printing. One specific application of origami techniques is the creation of porous biomaterials. When functionalized with appropriate nano-patterns, origami-based lattices might serve as meta-biomaterials in which nano-scale surface texture communicates with stem cells and determines the stem cell fate [17]. Many other properties such as hydrophilicity[5], anti-bacterial [18], surface adhesion [19], and permeability [20] could be adjusted or induced through a combination of surface nano-patterns and geometry. This is a novel approach with many open research questions of which a few are addressed in this thesis. In particular, practical folding of lattices that are based on various types of repeating unit cells from flat shape has been so far mostly illusive. Self-folding of materials from their flat state to the intended 3D geometry is the other research question addressed here.

Prospects and implementation

Reflecting the structure presented above, this thesis is organized into two parts. In the first part, rational design of geometry and spatial distribution of material properties within the structure of soft cellular matter are used to achieve higher levels of tunability in the instability behavior of soft mechanical metamaterials. Experimental and computational techniques are used in conjunction with each other to explore the feasibility of this type of material programming. The Part two focuses on realization of highly functionalized 3D materials. To create such a complex material, a rational solution is to form the desired 3D configuration from a flat material. In this scenario a 2D flat material is initially functionalized by using the available micro/nanolithography techniques and finally self-folding is used to create the desired 3D shape. To specifically enable fabrication of miniaturized 3D lattices, this part mainly focuses on the kinematic of folding of periodic polyhedral geometries and proposes various techniques that enable self-folding of (soft) flat matter.

Thesis outline

Part A: Soft cellular materials

Chapter 2 relates the geometrical design of 2D soft periodic cellular materials under compression to their critical (i.e., instability) behavior. A systematic methodology to generate symmetric void shapes provides a library of pore shapes varying from circle to n-fold symmetric shapes. Experimental results illustrate that two main modes of

global buckling (i.e., symmetric compaction and side-buckling) are the buckling modes. Computational models are then created, validated against experimental results, and used to relate the void geometry to the parameters describing the onset of instability. Additionally, instability maps are provided to relate the void geometry to the global mode of buckling. Using a number of hyperelastic material properties, we found that that the stiffness of this proposed class of mechanical metamaterials could be tuned independently from its instability strain.

Chapter 3

The effects of material properties on the critical behavior of 2D cellular materials has not been studied before. We designed three types of geometrical design where the repeating unit cells were divided into square and intermediate ligament-like elements with different material properties. Multi-material 3D printing was used to fabricate cellular specimens whose unit cells were divided into soft and stiff segments as described above. Validated computational models showed that the critical strain could be adjusted independently from the critical stress while keeping the ratio of the material elasticity (the elastic modulus of the ligament to that of the square element) constant. Within the stiffness ratio range of $(0.1 - 10)$, the critical strain showed a power-law relationship with the stiffness ratio of the soft and hard materials. While geometrical design altered the critical strain by up to 3-folds, the critical strain could be altered by up to 9-folds when the above-described ways of distributing materials properties were used. Moreover, the spatial distribution of materials properties changed the buckling mode for some of the void geometries.

Chapter 4

Chapter 4 takes the tunability in the instability behavior of soft cellular materials to the next level. The combination of geometrical design and spatial distribution of materials properties are used for adjusting the instability behavior of 3D cellular structures. To create 3D unit cells, 2D void shapes are first projected onto the six external tangential planes from the three major mid-planes of a hollow sphere and then loft cut through the internal and external void shapes. We divided the unit cells into two parts, namely the corner and central parts, each of which with a different set of mechanical properties (flexible or stiff). Cellular arrays were then made by BCC arrangement of the unit cells. Three geometrical designs with three different ratios of the stiffness of both parts (0.5, 1, and 2) were used to fabricate 9 specimens using multi-material 3D printing. Computational analysis was then used to understand the effects of geometrical design and spatial distribution of material properties on the critical behavior of 3D soft cellular matter. We found that the critical stress and critical strain could be adjusted both independently and concomitantly within wide ranges. Our designs also resulted in the emergence of a new lowest instability mode, i.e.

double-side buckling. Finally, we proposed a general approach that pre-disposes the cellular structures to specific buckling modes, enabling them to reliably actuate their higher instability modes without the need for additional boundary conditions or fixtures.

Chapter 5

The effects of geometrical design on a different functionality of cellular mechanical metamaterials, namely shape morphing, is studied in this chapter. Auxetic and conventional unit cells are combined with each other using a rational design approach such that the resulting cellular morphs pre-defined shape upon stretching. The combination of auxetic and conventional unit cells was guided by computational models. We demonstrate that the presented designs could match the arbitrary shapes defined by random curves defined using Fourier's functions. The capabilities of the presented approach were then further demonstrated through design and manufacturing of cellular structures that matched the contours of three real-world objects.

Part B: From flat shapes to 3D geometries

Chapter 6 describes how complex lattices could be folded starting from flat sheets. Three folding strategies have been proposed for different types of lattices depending on the type of their repeating unit cells. We used the proposed folding strategies to fold an auxetic mechanical metamaterial from flat sheets. Moreover, we demonstrated how flat materials could be programmed to sequentially self-fold into the desired lattice shape. Finally, we used two different surface patterning methods (i.e., laser micro-machining and electron beam induced deposition) to create micro- and nano-scale patterns on the surface of pure titanium sheets. Electron beam induced deposition is especially interesting as it allows for free-form surface ornamentation with features sizes that are as small as ≈10 nm. The folding patterns and the presented experimental techniques form the basis for a unique platform for fabrication of metamaterials with unprecedented combination of geometrical designs and surface-driven functionalities.

Chapter 7

This chapter presents a number of strategies for transforming the shape of functionalized 2D material into a complex 3D geometry. A number of basic modes of shape-shifting are proposed using bilayers of active (shape memory) and passive polymers. The effects of various programming parameters such as the geometry of the bi-layers and the activation temperature on the resulting 3D shape were studied experimentally. Furthermore, we demonstrated how simple modes of shape shifting (e.g., self-rolling and self-twisting) could be combined with each other to create more

complex 3D geometries. The possibility of incorporating arbitrarily complex surface patterns was demonstrated using ultraviolet-curing of photopolymers on a single piece of self-twisting material.

Chapter 8 presents a novel technique for programming a desired pattern of shape shifting in flat materials using widely available 3D printers that work on the basis of fused deposition modeling. In this approach, inexpensive shape memory polymers (i.e., polylactic acid) are printed and programmed in a single-step production process. The effects of various parameters such as the printing temperature, layer height, activation temperature, and printing pattern on the level of strain recovery were experimentally studied in single-ply constructs. Once triggered by high temperatures, the printed flat material changes its dimensions. Multi-ply and single-ply assemblies (or a combination of both) were then devised to convert flat shapes into pre-programmed 3D shapes. Active bending elements and buckling due to internal stresses were the main working mechanisms in the presented shape-shifting materials. A particularly interesting design approach demonstrated in chapter 7 is the use of heat transfer concepts (through the incorporation of porosity and varying the thickness of the constructs) to program time delays in the folding process, thereby enabling 'sequential shape-shifting'. To demonstrate the presented principles, we show how they could be used to enable sequential folding of Mimosa pudica and tulip from flat configurations.

Finally, **chapter 9** briefly discusses the results of the thesis, makes remarks regarding the potential applications of the designed metamaterials and proposed approaches, and suggests possible directions for future research.

References

[1] S. Kinoshita, S. Yoshioka, and J. Miyazaki, *Physics of structural colors*, Rep Prog Phys **71**, 076401 (2008).

[2] J. Y. Sun and B. Bhushan, *Structure and mechanical properties of beetle wings: a review*, Rsc Advances **2**, 12606 (2012).

[3] V. Saranathan, C. O. Osuji, S. G. Mochrie, H. Noh, S. Narayanan, A. Sandy, E. R. Dufresne, and R. O. Prum, *Structure, function, and self-assembly of single network gyroid (I4132) photonic crystals in butterfly wing scales*, Proc Natl Acad Sci U S A **107**, 11676 (2010).

[4] H. E. Jeong and K. Y. Suh, *Nanohairs and nanotubes: Efficient structural elements for gecko-inspired artificial dry adhesives*, Nano Today **4**, 335 (2009).

[5] B. Bhushan and Y. C. Jung, *Natural and biomimetic artificial surfaces for superhydrophobicity, self-cleaning, low adhesion, and drag reduction*, Prog Mater Sci **56**, 1 (2011).

[6] G. D. Bixler and B. Bhushan, *Biofouling: lessons from nature*, Philos Trans A Math Phys Eng Sci **370**, 2381 (2012).

[7] L. Wang, J. T. Cheung, F. Pu, D. Li, M. Zhang, and Y. Fan, *Why do woodpeckers resist head impact injury: a biomechanical investigation*, PLoS One **6**, e26490 (2011).

[8] S. P. Silva, M. A. Sabino, E. M. Fernandes, V. M. Correlo, L. F. Boesel, and R. L. Reis, *Cork: properties, capabilities and applications*, International Materials Reviews **50**, 345 (2005).

[9] L. Ionov, *Biomimetic 3D self-assembling biomicroconstructs by spontaneous deformation of thin polymer films*, J Mater Chem **22**, 19366 (2012).

[10] R. M. Erb, J. S. Sander, R. Grisch, and A. R. Studart, *Self-shaping composites with programmable bioinspired microstructures*, Nat Commun **4**, 1712 (2013).

[11] J. T. B. Overvelde, S. Shan, and K. Bertoldi, *Compaction Through Buckling in 2D Periodic, Soft and Porous Structures: Effect of Pore Shape*, Adv Mater **24**, 2337 (2012).

[12] Y. Chen, R. Peng, and Z. You, *APPLIED ORIGAMI. Origami of thick panels*, Science **349**, 396 (2015).

[13] D. M. Sussman, Y. Cho, T. Castle, X. Gong, E. Jung, S. Yang, and R. D. Kamien, *Algorithmic lattice kirigami: A route to pluripotent materials*, Proc Natl Acad Sci U S A **112**, 7449 (2015).

[14] S. Babaee, J. Shim, J. C. Weaver, E. R. Chen, N. Patel, and K. Bertoldi, *3D soft metamaterials with negative Poisson's ratio*, Adv Mater **25**, 5044 (2013).

[15] Y. Zarate, S. Babaee, S. H. Kang, D. N. Neshev, I. V. Shadrivov, K. Bertoldi, and D. A. Powell, *Elastic metamaterials for tuning circular polarization of electromagnetic waves*, Sci Rep **6**, 28273 (2016).

[16] M. Schenk and S. D. Guest, *Geometry of Miura-folded metamaterials*, Proc Natl Acad Sci U S A **110**, 3276 (2013).

[17] B. K. Teo, S. T. Wong, C. K. Lim, T. Y. Kung, C. H. Yap, Y. Ramagopal, L. H. Romer, and E. K. Yim, *Nanotopography modulates mechanotransduction of stem cells and induces differentiation through focal adhesion kinase*, ACS Nano **7**, 4785 (2013).

[18] J. Hasan, R. J. Crawford, and E. P. Ivanova, *Antibacterial surfaces: the quest for a new generation of biomaterials*, Trends Biotechnol **31**, 295 (2013).
[19] J. Genzer and K. Efimenko, *Recent developments in superhydrophobic surfaces and their relevance to marine fouling: a review*, Biofouling **22**, 339 (2006).
[20] H. Montazerian, E. Davoodi, M. Asadi-Eydivand, J. Kadkhodapour, and M. Solati-Hashjin, *Porous scaffold internal architecture design based on minimal surfaces: A compromise between permeability and elastic properties*, Mater Design **126**, 98 (2017).

Part A
Soft Cellular Materials

Chapter 2

Geometry-based control of instability patterns in cellular soft matter

RSC Advances (2016, 6, 20431)

Recent research has shown the potential of rationally designed geometrical features for controlling the functionality of advanced materials. Of particular recent interest has been the use of geometry for controlling the buckling behavior of soft materials under compression. However, the effects of geometry are may be mixed with those of the mechanical properties. In this paper, we present a specific class of 2D cellular soft matter for which the geometry, independent from the mechanical properties of the bulk material, activates the instability pathways of the material, thereby controlling the instability threshold and the instability mode (instability pattern). The geometrical parameters include those characterizing the shape of the voids and the porosity of the cellular solid. A critical strain that solely depends on the geometry controls the transition to instability. Depending on the above-mentioned geometrical parameters, the onset of instability is followed by either symmetric compaction or side buckling. We provide instability maps that relate the geometrical parameters to the critical strain and the instability mode of the presented cellular soft material. These open up the possibility of using geometry for programming the functionalities of programmable materials.

The relationship between geometry and functional properties of (soft) materials has recently received increasing attention. For example, magnificent mechanical and physical properties of natural materials such as iridescent and lightweight structures may be achieved via certain arrangement of the microstructures forming a cellular solid [1-3]. Using similar principles, some creatures disguise themselves by switching their structural color in response to environmental factors [1,4]. A major theme within this line of research is rational geometrical design of materials so as enable them exhibit the desired and occasionally unprecedented properties and functionalities.

An important example, which defines the context for the current study, is the case of soft cellular solids that exhibit sudden transformation in their original structural patterns under compression, when a certain loading threshold is reached [5,6]. The geometry of pores and mechanical properties of the materials can regulate buckling instability in this kind of periodic structures so as to make them show specific behaviors in response to diverse stimuli [7-10]. For example, soft cellular solid composed of an array of repetitive unit cells may display reversible and repeatable pattern switching [6,7,11-13]. This type of behavior could be used for a variety of applications where artificial responsive materials change their configuration in response to diverse stimuli such as loads, moisture, etc. [9,14,15]. Equipped with cellular configuration, activated structures can exhibit shape shifting that could be of tremendous value in soft robotics and smart bodies [16,17]. Moreover, cellular configuration of materials in combination with optimization techniques opens an avenue towards design of optimal materials [18-21]. Notably, Bertoldi and co-workers have extensively explored 2D periodic cellular materials [5,7,8,12,13,22-25].

In this paper, we use both experimental and computational approaches to study how n-fold symmetric voids, a square array of soft hyperelastic porous unit cells, control the critical strain of 2D soft periodic structures under compression, where n (the number of folds) is an even number. The pore shapes considered here conform to a modified version of an analytical angular function that was originally used to formulate the shape evolutions caused by deposition of graphene monolayers on Cu foils [26]. That original function was modified and re-written as a polar vector (V) to generate n-fold symmetric shapes:

$$V(\theta) = c\left((1+r) - d(-1)^{\frac{n+2}{2}}(r-1)cos(n\theta)\right) \quad (1)$$

where, $0 \leq \theta \leq 2\pi$ scalar coefficient c is used to control the porosity in the unit cell, r controls the sharpness of folds, $d = \pm 1$ adjusts the orientation of the voids, and n determines the number of folds (Fig 1a). As r decreases from 1, the pore shape evolves from a circular geometry to shapes with sharper folds/edges (Fig. 1a). For a given porosity, α, the scale factor c is calculated, independent from the number of folds, as follows:

$$c = \frac{\sqrt{2\pi(3+3r^2+2r)\phi}L}{\pi(3+3r^2+2r)} \quad (2)$$

where L_0 is the edge length in the 2D square unit cells. Moreover, α and L_0 are chosen such that $V(\theta) < L_0/\left(2cos\left(\theta - \frac{n\pi}{2}\right)\right)$, $n = 0.1$ to maintain the integrity of the unit cells.

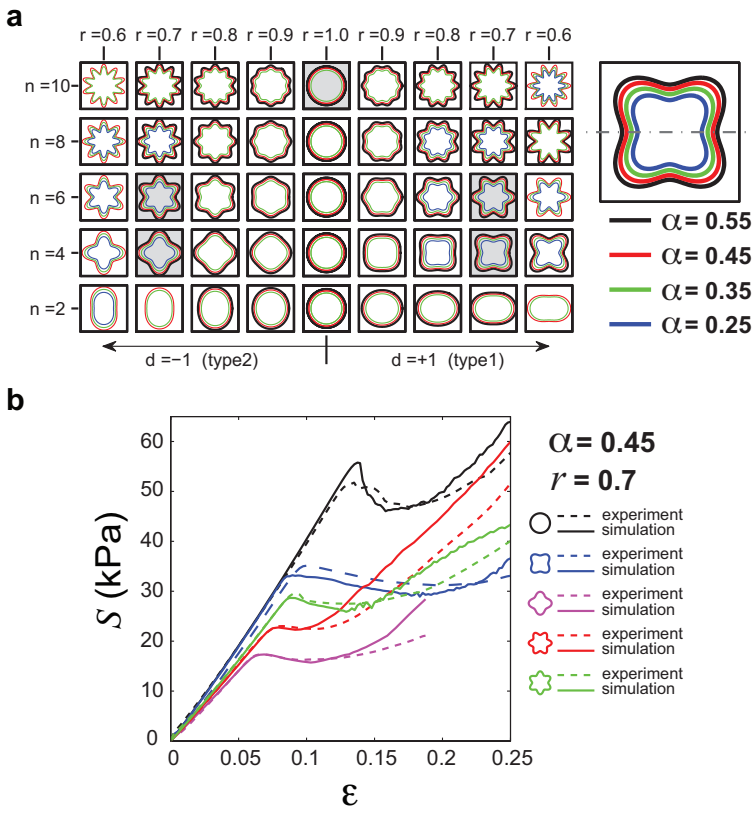

Figure 1
(a) The pore shape of the cellular soft materials studied here and the parameters that define their geometry. Five of these pore shapes (painted in grey) were selected for the experimental study. Different colours of the pore contour indicate different pore sizes and, thus, porosities. (b) Comparison between the experimental and computational stress-strain curves of the five selected structures. Even though the actual dimensions were used in the simulations, the nominal values are presented in the caption of this figure.

All geometries depicted in Fig. 1a were included in our computational study. The geometries were chosen so as to preserve the integrity of the structure while ensuring that the size of voids allows for pattern transition. Five sample structures were chosen for an experimental study to validate our computational findings. In both

computational and experimental studies, the specimens comprised arrays of 7 by 7 repeating unit cells with two additional half unit cells on both sides of the specimens (Fig. 2d). This arrangement of unit cells is the minimum size that finite structures need for symmetric pattern transition. The actual dimensions of the pores in the experimental specimens were measured and used for creating the computational models whose results were compared with the experimental observations. That involved offsetting the boundaries of the pores inwards by 250 μm (the approximate deviation of the dimensions of the actual specimens from the designed dimensions).

Specimens were compressed uniaxially in the vertical direction with a deformation rate of 2~10 mm/min. A digital camera was used to follow the deformation and instability patterns as loading progressed. The height and cross-section area of the structure were respectively used for calculating the nominal strain and nominal stress values.

The incompressible Neo-Hookean material model with a material parameter $C_{10} = 105kPa$ was used to describe the mechanical behaviour of the bulk material. An implicit nonlinear finite element solver (Abaqus/Standard) was used to solve the governing equations of deformation. An explicit nonlinear solver (Abaqus/Explicit) was used when the contact between the internal sides of the closing pores was taken into account. A mesh convergence study was conducted to select the appropriate mesh density. Based on the convergence study, a maximum seed size equal to 3.5% of the length of the unit cell edges was selected, resulting in 800-1350 elements per unit cell. Triangular quadratic plane strain hybrid elements (CPE6H) were used for the implicit solutions, while the modified type of the same element (CPE6M) was used for explicit analysis. To detect the instability patterns, eigenvalue buckling analysis (subspace technique) was performed. The post-bulking simulations included an initial geometric imperfection equal to 0.01 of the magnitude of the deformation in the first buckling mode of the structure. The finite element simulations were quasi-static. Clamped boundary conditions were used on both sides of the specimens.

There was generally good agreement between the experimentally determined stress-strain curves and the corresponding computational curves except for the very final stages of deformation where the experimental and computational curves started to deviate from each other (Fig. 1b). The predicted instability patterns very well matched the experimentally observed instability patterns for all the structures for which both experimental and computational data were available (Fig. 2).

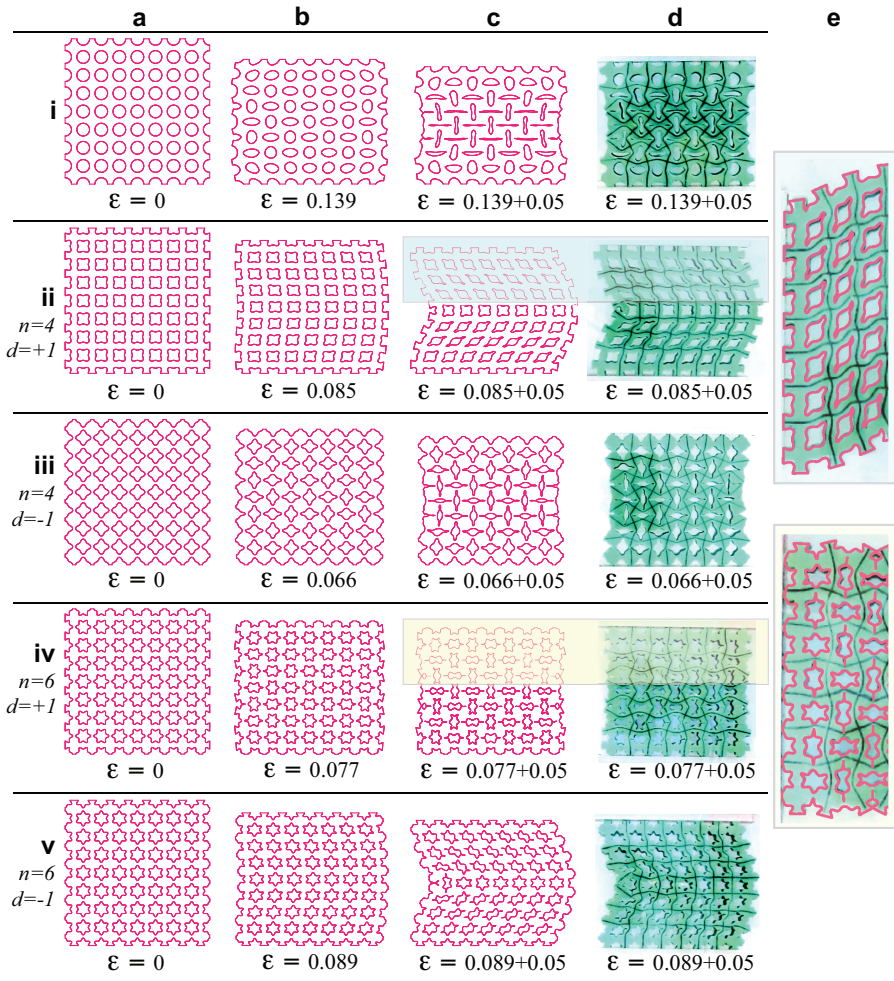

Figure 2
(a-c) The computationally predicted configuration of the five cellular structures for which experiments were performed before loading, at the critical state, and when loaded beyond the critical state (i.e. $\varepsilon_{cr} + 0.05$). (d) The experimentally observed configuration of the five cellular structures for which experiments were performed when loaded beyond the critical strain (i.e. $\varepsilon_{cr} + 0.05$). (e) The two magnified sections highlight that the microscopic deformations from computational analysis are in good agreement with experiments.

The stress-strain curves generally showed an initial linear behaviour followed by a stress plateau region where the stress did not substantially increase (Fig. 1b). The stress finally started to increase due to the closing pores and the resulting contact between the internal walls of the pores (Fig. 1b). For every cellular structure, the transition from the linear region to the stress plateau occurred after a specific level of strain that is called the critical strain in the current study (Fig. 1b). We defined the

critical strain as the strain for which the maximum stress at the end of the linear region was recorded (Fig. 1b), unless there was no clear stress peak in which case the maximum radius of curvature in the stress-strain curve was used as a criterion for detecting the critical strain. A parametric study showed that the computational results are not over-sensitive to the magnitude of the imperfections and do not drastically change when the imperfection size is perturbed around the chosen values. Once the loading progressed beyond the critical strain, a rapid transformation in the pattern of the cellular structures occurred, which was considered as the hallmark of buckling (Fig. 2). Depending on the geometry of the pores, e.g. the number of folds and the porosity of the cellular structures, two different types of instability patterns were observed, namely side buckling (Fig. 2ii, v) and symmetric compaction (Fig. 2i, iii, iv). To study the material effect on the critical strain of soft cellular structures, in addition to the material used in our experiments, the mechanical properties of three different types of polydimethylsiloxane (PDMS) elastomers were taken from [27]. The difference between the mixing ratio of the base polymer and the curing agent causes a great difference in the mechanical properties of PDMS elastomers. Three different material models (Neo-Hookean, Yeoh, and Ogden (order 3) were chosen to evaluate the effect of constitutive equation on the response of the considered structures. The material model constants of PDMS elastomers were obtained by fitting the uniaxial stress-strain curves up to the point where the stress started to increase as a result of bond stretching (Material constants and related uniaxial stress-strain curves are provided in the supplementary information file.). This led to closer material properties for all the three models, especially in compression. Three extreme geometries (circular as well as four-fold types 1 and 2, all having porosities of 0.45 and fold sharpness of $r = 0.7$) were used to study the effects of material properties on the buckling behaviour. All considered cases showed pattern transition at relatively large strains. Numerical results clearly showed that the critical strain remains the same regardless of the material properties (Fig. 3). This independency from material properties held also for the type of instability, i.e. side buckling vs. symmetric compaction. The sole effect of the material properties was shifting the load at which pattern transition occurred (Fig. 3). Microstructures experience both tensile and compressive stresses when the structures are compressed uniaxially.

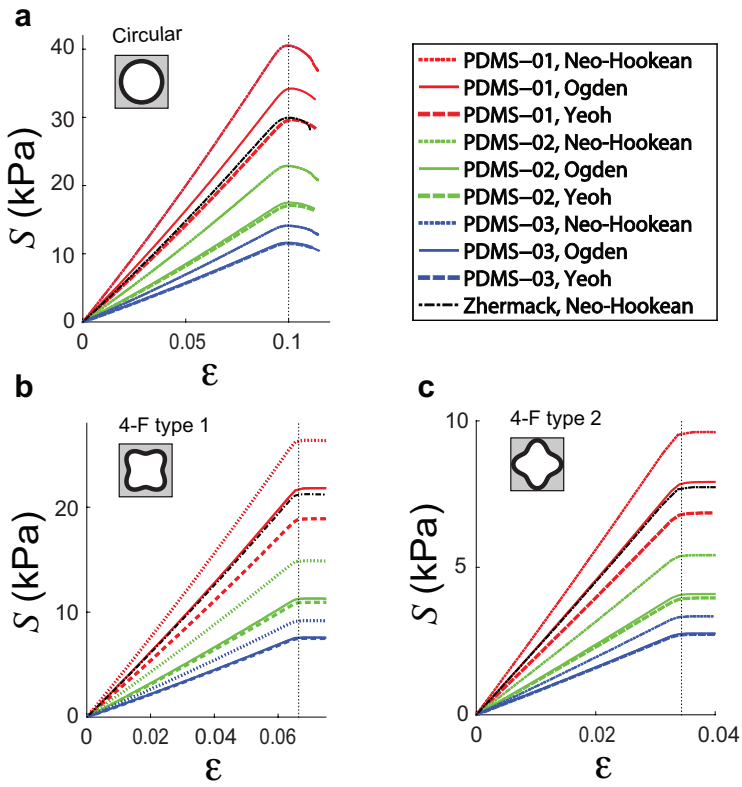

Figure 3
Stress-Strain curves of the cellular structures when four different material properties where used for modelling the bulk material. The structures with circular and 4-fold type two voids follow symmetric compaction instability (a, c), and the structure 4-fold type one experience side buckling (b). Each structure shows the same critical strain for different elastomers independent of material.

Geometry of pores influences both the pattern instability and critical strain. For the circular pores, the instability pattern was symmetric compaction for larger (i.e. > 0.35) porosities and side buckling for smaller (i.e. <0.35) porosities (Fig. 4). For 2-fold structures, the instability pattern was similar to that of the structures with circular pores when $r \approx 1$ (Fig. 4). For $r \ll 1$, side buckling was the instability pattern of the 2-fold structures (Fig. 4). For n-fold structures ($n > 2$), three distinct regions could be observed in the maps of the instability patterns (Fig. 4). In the first region (painted yellow in Fig. 4), the instability pattern was side buckling. In the second region (painted magenta in Fig. 4), the instability pattern was symmetric compaction. In the third region (painted blue in Fig. 4), the instability pattern was dependent on the

convexity/concavity of the curve that defines the pore shape at the location where the curve meets the horizontal symmetry line (see Fig. 1a). When the curve defining the pore shape was convex/concave at its intersection with the horizontal symmetry line, the instability pattern was always side buckling/symmetric compaction (Fig. 4). The concavity/convexity were defined with respect to the observer standing at the centre of the unit cell.

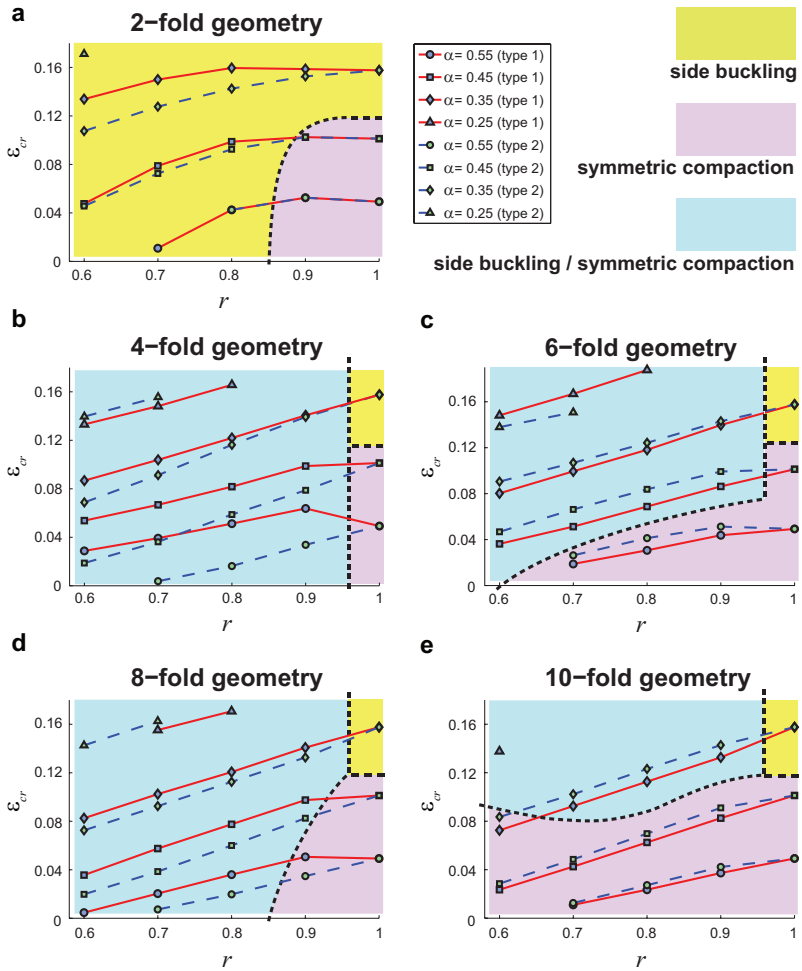

Figure 4

The critical strains calculated for the different types of cellular structures with different pore shapes. The colour codes show the type of instability pattern that resulted from any given type of pore geometry.

In side buckling, the middle row of the specimens experienced relatively small deformation (Fig. 2) that means specific areas that are protected from excessive deformation could exist even when the other areas experienced excessive deformation. This type of areas may need to be included in the positions within the structure that require protection from excessive deformation. Even before reaching the critical strain, pre-cursors to the instability patterns could be identified both for side buckling and symmetric compaction (Fig. 2b). In the case of side buckling, the pre-cursors were manifested in terms of curvy boundaries, while the boundaries between the unit cells exhibited increasing levels of waviness in the case of symmetric compaction (Fig. 2d-i,iii, iv). In symmetric compaction, the contact between the inner walls of closing pores, which occurs for very large strains, induced some levels of geometric frustration that elicited side buckling in addition to symmetric compaction. As r approaches 1, the pore shapes approach a circle (Fig. 1a). A sudden shift in the type of the instability pattern was therefore detected for some structures somewhere between $r = 0.9$ and $r = 1$ (Fig. 4).

Except for structures with 2-fold pores, the critical strains of all other types of structures more or less linearly increased as r increased from 0.6 to 1.0 (Fig. 4). The same linear behaviour was observed for all porosities and both orientations of the pores (i.e., $d = \pm 1$) (Fig. 4). One could therefore conclude that the critical strain values are smaller when pores with sharper folds are used in the cellular structure. In general, the difference between the critical strains of structures with different orientation of pores (i.e., $d = \pm 1$) tended to decrease, as the number of folds, n, increased. This can be attributed to the more symmetry lines in pore shapes with larger number of folds that minimizes the effect of orientation (i.e. rotation) of pores on the stress distribution of the cellular structures.

In summary, we presented a specific class of cellular soft matter whose instability patterns and instability thresholds (i.e. critical strains) are exclusively controlled by the geometry of the pores. The possibility of decoupling instability patterns and instability thresholds from the properties of the bulk material opens new avenues for utilizing geometry as a tool for programing and controlling the state of the so-called 'programmable materials'. Despite the rich mechanical behaviour that the presented cellular structures exhibit, in most cases, their critical strains linearly change with the sharpness of the folds and are simple functions of the other geometrical parameters. These relatively simple relationships together with the instability maps (Fig. 4) provide us with some design rules that could be potentially used in development of programmable materials that exploit geometry as a way of controlling the buckling behaviour.

References

[1] J. Huang, X. Wang, and Z. L. Wang, *Controlled replication of butterfly wings for achieving tunable photonic properties*, Nano Lett **6**, 2325 (2006).

[2] U. G. K. Wegst, H. Bai, E. Saiz, A. P. Tomsia, and R. O. Ritchie, *Bioinspired structural materials*, Nat Mater **14**, 23 (2015).

[3] K. Muamer, B. Tiemo, S. Robert, and W. Martin, *Metamaterials beyond electromagnetism*, Rep Prog Phys **76**, 126501 (2013).

[4] H. Wang and K.-Q. Zhang, *Photonic Crystal Structures with Tunable Structure Color as Colorimetric Sensors*, Sensors **13**, 4192 (2013).

[5] T. Mullin, S. Deschanel, K. Bertoldi, and M. C. Boyce, *Pattern transformation triggered by deformation*, Phys Rev Lett **99**, 084301, 084301 (2007).

[6] T. Mullin, S. Willshaw, and F. Box, *Pattern switching in soft cellular solids under compression*, Soft Matter **9**, 4951 (2013).

[7] J. T. B. Overvelde, S. Shan, and K. Bertoldi, *Compaction Through Buckling in 2D Periodic, Soft and Porous Structures: Effect of Pore Shape*, Adv Mater **24**, 2337 (2012).

[8] S. H. Kang, S. Shan, W. L. Noorduin, M. Khan, J. Aizenberg, and K. Bertoldi, *Buckling-Induced Reversible Symmetry Breaking and Amplification of Chirality Using Supported Cellular Structures*, Adv Mater **25**, 3380 (2013).

[9] C. R. Tipton, E. Han, and T. Mullin, *Magneto-elastic buckling of a soft cellular solid*, Soft Matter **8**, 6880 (2012).

[10] J. Shen, Y. M. Xie, S. Zhou, X. Huang, and D. Ruan, *Water-responsive rapid recovery of natural cellular material*, J Mech Behav Biomed Mater **34**, 283 (2014).

[11] S. Babaee, J. Shim, J. C. Weaver, E. R. Chen, N. Patel, and K. Bertoldi, *3D soft metamaterials with negative Poisson's ratio*, Adv Mater **25**, 5044 (2013).

[12] J. Shim, S. C. Shan, A. Kosmrlj, S. H. Kang, E. R. Chen, J. C. Weaver, and K. Bertoldi, *Harnessing instabilities for design of soft reconfigurable auxetic/chiral materials*, Soft Matter **9**, 8198 (2013).

[13] K. Bertoldi, M. C. Boyce, S. Deschanel, S. M. Prange, and T. Mullin, *Mechanics of deformation-triggered pattern transformations and superelastic behavior in periodic elastomeric structures*, J Mech Phys Solids **56**, 2642 (2008).

[14] G. Wu, Y. Xia, and S. Yang, *Buckling, symmetry breaking, and cavitation in periodically micro-structured hydrogel membranes*, Soft Matter **10**, 1392 (2014).

[15] X. Zhao, J. Kim, C. A. Cezar, N. Huebsch, K. Lee, K. Bouhadir, and D. J. Mooney, *Active scaffolds for on-demand drug and cell delivery*, Proc Natl Acad Sci U S A **108**, 67 (2011).

[16] X. Yao, Y. Hu, A. Grinthal, T.-S. Wong, L. Mahadevan, and J. Aizenberg, *Adaptive fluid-infused porous films with tunable transparency and wettability*, Nat Mater **12**, 529 (2013).

[17] Y. Cho *et al.*, *Engineering the shape and structure of materials by fractal cut*, Proc Natl Acad Sci U S A **111**, 17390 (2014).

[18] P. G. Coelho and H. C. Rodrigues, *Hierarchical topology optimization addressing material design constraints and application to sandwich-type structures*, Struct Multidiscip Opt **52**, 91 (2015).

[19] M. P. Bendsøe and O. Sigmund, *Material interpolation schemes in topology optimization*, Arch Appl Mech **69**, 635 (1999).
[20] J. C. Álvarez Elipe and A. Díaz Lantada, *Comparative study of auxetic geometries by means of computer-aided design and engineering*, Smart Mater Struct **21**, 105004 (2012).
[21] H. A. Eschenauer and N. Olhoff, *Topology optimization of continuum structures: A review*, Appl Mech Rev **54**, 331 (2001).
[22] J. T. B. Overvelde and K. Bertoldi, *Relating pore shape to the non-linear response of periodic elastomeric structures*, J Mech Phys Solids **64**, 351 (2014).
[23] K. Bertoldi, P. M. Reis, S. Willshaw, and T. Mullin, *Negative Poisson's ratio behavior induced by an elastic instability*, Adv Mater **22**, 361 (2010).
[24] P. Wang, J. M. Shim, and K. Bertoldi, *Effects of geometric and material nonlinearities on tunable band gaps and low-frequency directionality of phononic crystals*, Phys Rev B **88**, 014304 (2013).
[25] S. H. Kang, S. Shan, A. Kosmrlj, W. L. Noorduin, S. Shian, J. C. Weaver, D. R. Clarke, and K. Bertoldi, *Complex ordered patterns in mechanical instability induced geometrically frustrated triangular cellular structures*, Phys Rev Lett **112**, 098701 (2014).
[26] L. Fan *et al.*, *Topology evolution of graphene in chemical vapor deposition, a combined theoretical/experimental approach toward shape control of graphene domains*, Nanotechnology **23**, 115605, 115605 (2012).
[27] T. K. Kim, J. K. Kim, and O. C. Jeong, *Measurement of nonlinear mechanical properties of PDMS elastomer*, Microelectron Eng **88**, 1982 (2011).

Supplementary information

Table S1
Material model constants of three different PDMS (polydimethylsiloxane) and Zhermack (Elite Double 22) elastomers. The numbers in the parenthesis denote the ratio of base polymer to curing agent.

Material model		PDMS-01 (5:1)	PDMS-02 (10:1)	PDMS-03 (15:1)	Zhermack (1:1)
Neo-Hookean	$C_{10}(MPa)$	0.136	7.674×10^{-02}	4.732×10^{-02}	0.105
Yeoh	$C_{10}(MPa)$	9.631×10^{-02}	5.578×10^{-02}	3.871×10^{-02}	
	$C_{20}(MPa)$	1.210×10^{-02}	7.650×10^{-03}	-9.430×10^{-04}	
	$C_{30}(MPa)$	3.011×10^{-02}	7.276×10^{-03}	1.052×10^{-03}	
Ogden	$\mu_1(MPa)$	-0.628	-1.137	-0.689	
	$\mu_2(MPa)$	0.415	0.591	0.253	
	$\mu_3(MPa)$	0.435	0.661	0.514	
	α_1	4.464	4.199	4.177	
	α_2	5.979	5.063	4.867	
	α_3	-7.564×10^{-02}	2.927	3.478	

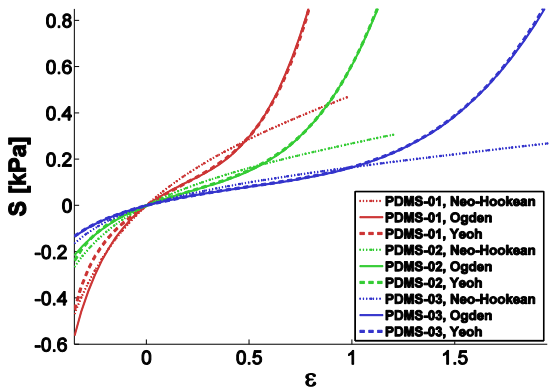

Figure S1
Uniaxial stress-strain curves resulted from the material constants given in Table S1.

Chapter 3

Multi-material control of instability in soft mechanical metamaterials

Physical Review Applied (2018, 9, 064013)

Soft mechanical metamaterials working on the basis of instability have numerous potential applications in the context of "machine materials". Controlling the onset of instability is usually required when rationally designing such metamaterials. We studied the isolated and modulated effects of geometrical design and material distribution on the onset of instability in multi-material cellular metamaterials. We used multi-material additive manufacturing to fabricate cellular specimens whose unit cells were divided into void space, a square element, and an intermediate ligament. The ratio of the elastic modulus of the ligament to that of the square element, E_L/E_S, was changed by using different material types. Computational models were also developed, validated against experimental observations, and used to study a wide range of possible designs. The critical stress could be adjusted, independently from the critical strain, by changing the material type while keeping E_L/E_S constant. The critical strain showed a power-law relationship with E_L/E_S within the range $E_L/E_S = 0.1$-10. Void shape design altered the critical strain by up to 3-fold, while the combined effects of void shape and material distribution caused up to 9-folds change in the critical strain. This highlights the strong influence of material distribution on the onset of instability and buckling mode.

Mechanical metamaterials [1,2] are usually designed to exhibit unusual mechanical behavior such as negative [3,4] or ultrahigh [5] values of mechanical properties. Most mechanical metamaterials are architectured [6], meaning that their large-scale properties originate from the design of their small-scale architecture. Rational design [7] techniques based on computational and analytical models are often used to devise the small-scale architectures that give rise to the desired set of mechanical properties. The geometrical basis for designing such architectures may be lattice structures [5,8,9], origami [7,10,11], or kirigami [12-14], among others.

The very concept of "architectured" metamaterials implies the presence of more than one material, as geometrical patterns particularly those relevant for metamaterial design generally require at least two types of material properties. In cellular or lattice structures, those materials include the matrix material with finite properties and the "voids" with negligibly low properties. The rational design of cellular structures then reduces to devising a plan for spatially distributing the matrix material and leaving the remainder of the space for the "voids". Milton and Cerkaev have shown that any thermodynamically admissible elasticity tensor could be realized by combining a matrix material with a void material [15]. When dealing with large deformations of soft matter, the "void" material plays an important role in guiding the deformation path. The soft metamaterials working on the basis of buckling instability [16-18] are perhaps the best examples for showcasing the role of the voids. Voids enable local buckling, control the instability threshold, and guide the post-buckling behavior of such materials [19-21].

Additive manufacturing (AM) has enabled arbitrarily complex spatial distributions of the matrix and void materials for several years. Recent advances in multi-material additive manufacturing techniques have, however, enabled us to go much further and spatially distribute practically unlimited number of materials in a single-step manufacturing process, thereby opening many novel avenues for the design of architectured materials [22]. In this study, we explored how the spatial distribution of multiple materials could be used to rationally design soft cellular metamaterials that work on the basis of buckling instability. Those materials have numerous potential applications in the context of "machine materials" [23,24] that span areas as diverse as soft robotics, flexible electronics, and medical implants. In particular, we considered multiple void geometries and different types of material distributions to study the isolated and modulated effects of geometrical design and material combination on the instability behavior of such materials.

The cellular structures were based on square unit cells whose void geometry was described using the following relationship [20]:

$$V(\theta) = c\left((1+r) - d(-1)^{\frac{n+2}{2}}(r-1)cos(n\theta)\right) \quad (1)$$

where $c = \frac{\sqrt{2\pi(3+3r^2+2r)\phi L}}{\pi(3+3r^2+2r)}$, $0 \le \theta \le 2\pi$, ϕ denotes the void fraction per unit cell area, r determines fold sharpness, $d = \pm 1$ defines the xy symmetry style, n regulates the number of folds, and L is the length of the unit cell. Three types of void shapes including circular ($(\phi, r, d, n) = (0.45, -, -, -)$), four-fold type one ($(\phi, r, d, n) = (0.45, 0.7, +1, 4)$), and four-fold type two ($(\phi, r, d, n) = (0.45, 0.7, -1, 4)$) were considered (Figure 1).

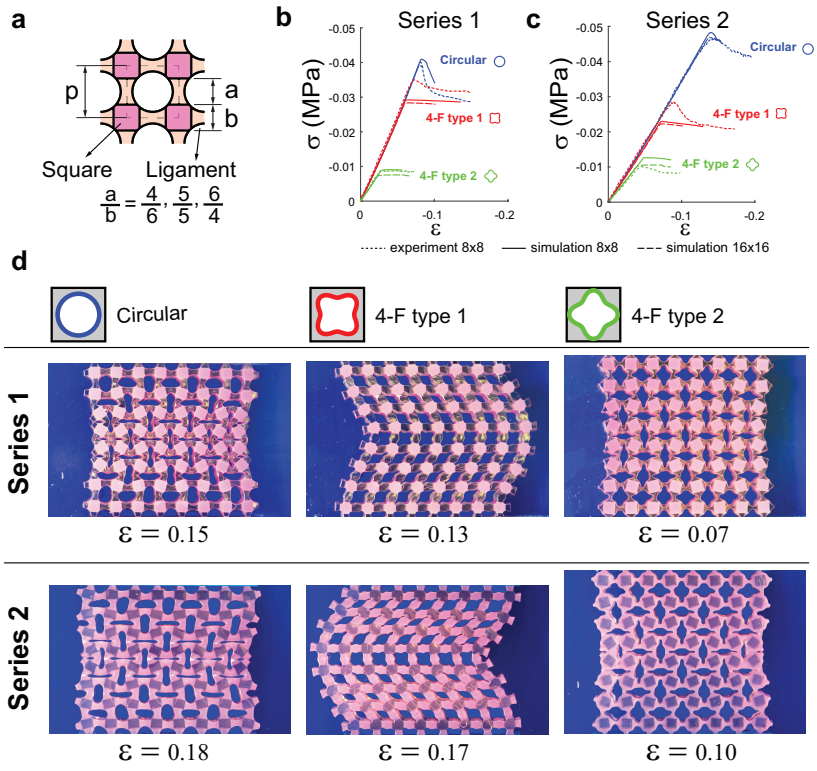

Figure 1
The geometry of the unit cells used in the design of the metamaterials and the division of the unit cells into ligaments and square elements (a). Comparison between experimentally determined and computationally predicted stress-strain curves for two different combinations of material properties and three different void shapes (b, c). The instability modes of two different types of multi-material metamaterials with three different void shapes (c d). Series 1 and 2 represent the structures in which ligament material is softer and stiffer than square material respectively.

The unit cells were partitioned symmetrically into ligaments and square-shaped elements (Figure 1a). Three different ratios of ligament length, a, and squares side, b, were considered: $\frac{a}{b} = \frac{4}{6}, \frac{5}{5}, \frac{6}{4}$. For each of the three void shapes, two different types of specimens (Figure 1d) were additively manufactured using a multi-material 3D

printer (Stratasys Object 350 Connex3, US) that works on the basis of jetting UV-curable photopolymers. During the printing process, all specimens were oriented such that the printing direction was in parallel with the loading direction. In the first series of the specimens, the ligament material (TangoPlus, nominal shore hardness A = 27) was softer than the square material (digital combination of Vero and TangoPlus, nominal shore hardness A = 60). The opposite held for the ligament (digital combination of Vero and Agilus, nominal shore hardness A = 60) and square (Agilus, nominal shore hardness A = 30) materials in the second set of specimens. The specimens included 8×8 cross-like unit cells and were designed with equal lengths of ligament and square (i.e. $\frac{a}{b} = \frac{5}{5}$). Two hard clamps (material name = Vero) were printed at both ends of the specimens to ensure consistent load application. A nominal unit cell length, L, of 10 mm and an out-of-plane thickness of 15 mm were considered for the design of the specimens. The specimens were mechanically tested under compression using a Lloyd test bench (LR5K) equipped with a 100 N load cell. A constant deformation rate of 1 mm/min was used. Two acrylic plates were placed on both sides of the specimens to preserve the plan strain conditions. Both sides of the specimens were polished and sprayed with a lubricant (Multi Spray 1000, Innotec) to minimize their friction with the acrylic plates. A digital camera (Sony A7R with a Sony FE 90 mm f/2.8 macro OSS lens) captured the deformations of the specimens during the mechanical tests. In addition, tensile strips with rigid rectangular end-clamps were produced to obtain an initial estimation of the mechanical properties of the different types of the polymers used in this study. A Neo-Hookean hyperelastic model was fitted to the results of the tensile test experiments and fine-tuned using the results of the compression tests. The following material parameters were obtained: $C_{10}^{\text{Soft}} = 0.13$ MPa, $C_{10}^{\text{Hard}} = 0.23$ MPa for the first series of the specimens and $C_{10}^{\text{Soft}} = 0.07$ MPa, $C_{10}^{\text{Hard}} = 0.20$ MPa for the second series of the specimens. The superscripts "Soft" and "Hard" refer to the softest and hardest materials among the ligament and square materials.

The instability behavior of the designed metamaterials was also analyzed computationally. The computational models were first validated against experimental results and were then expanded to analyze the effects of material choice and $\frac{a}{b}$ values on the instability behavior of the specimens. The geometry of the computational models included 8×8 unit cells and were discretized using six-node triangular hybrid plane strain elements (CPE6H, Abaqus/Standard). The polymers were considered to be nearly incompressible. The computational models were solved using an implicit solver (Abaqus/Standard, Version 6.13). Full Newton's method was used (default option) as a solution technique in Abaqus standard. A convergence study was performed to determine the size of the elements, resulting in an average density of 995 to 1017 elements per unit cell. The buckling modes were determined using linear

buckling analysis and a small imperfection of 0.01 from the buckling analysis was introduced into the models. The top and bottom nodes of the models were constrained to move together with their respective reference points, thereby ensuring consistent deformation of the clamped nodes. The elastic modulus, E, and Neo-Hookean material parameter, C_{10}, for an incompressible elastomer were assumed to be related through the following relationship: $E = 6C_{10}$ (because of the consistency with linear elasticity $G = 2C_{10}$ in which G is initial shear modulus of hyperelastic rubber and the relationship $E = 3G$). Five different ratios of the elastic modulus of the ligament material, E_L, to that of the square material, E_S, within the range of 0.1 to 10 were considered for performing the instability analyses. To evaluate whether a computational analysis with 8×8 unit cells is sufficient to predict the behavior of cellular structures with larger number of unit cells, additional analyses were performed using 16x16 unit cells.

The onset of instability could be clearly seen as a local maximum in the stress-strain curves of the specimens from both categories (Figure 1b-c). The instability patterns of all specimens were either compaction or side buckling (Figure 1d). For all the designs, the computational models could accurately predict the linear part of the stress-strain curve, the onset of instability, and the type of instability (Figure 1b-c). Analysis with 16×16 unit cells confirmed the use of 8×8 cellular structures is sufficient to predict the behavior of cellular structures with larger number of unit cells (Figure 1b-c). For all void shapes, the critical strain was higher when the ligament material was harder than the square material (i.e. the critical strains are higher in the second series of the specimens compared to the first series) (Figure 1b-c). Numerically estimated maximum stress and the critical strain values for the structures with the void shape four-fold type one, regardless of the ratio $\frac{E_L}{E_S}$, deviated from those observed in the experiments (Figures 1b-c, the stress-strain curves highlighted in red). The mismatch between the numerical and experimental results may partly be attributed to the friction between the samples and acrylic plates preventing out of plane buckling, use of an idealized material model in simulations without consideration of imperfection from production process, but mismatch is expected to be mainly due to viscosity effects during the fast pattern transformation coincident with the onset of instability. The geometrical design of the experimentally studies structures with four-fold type one voids result in general buckling (i.e. side buckling) happening with faster deformation rates compared to the two other types of structures. Viscosity consequently resist the rapid pattern transformation and postpones the occurrence of peak in the stress strain curves and increases the strain at which the local maximum stress happens (see the red curves in figure 1b-c).

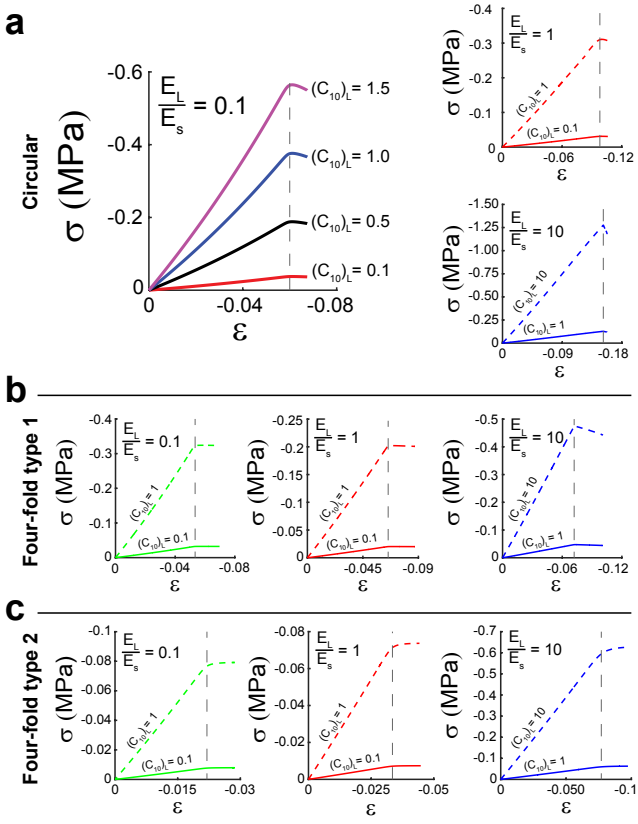

Figure 2

The stress-strain curves of metamaterials based on circular (a), four-fold type 1 (b), and four-fold type 2 (c) void shapes. The different values of the elastic modulus do not change the critical strain as long as E_L/E_S remains constant. Critical stresses are, however, scaled by the changes in the absolute values of the elastic moduli.

Computational analyses show that, as long as the ratio of the elastic modulus of the ligament material to that of the square material, $\frac{E_L}{E_S}$, was constant, the critical strain remained constant regardless of the absolute values of the elastic modulus of both materials (Figure 2). That same observation held for all types of void shapes and for all considered values of $\frac{E_L}{E_S}$ between 0.1 and 10 (Figure 2). The only difference was the altered critical stress values, i.e. the stress values at which instability commences (Figure 2). This implies that the critical stress values could be adjusted independently from the critical strain simply by changing the absolute values of the material properties, while keeping their ratio constant. From the practical viewpoint, the multi-

material additive manufacturing technique used here allows for combination of up to three materials at the voxel level to achieve several hundreds of different material properties. It is therefore perfectly feasible to change the absolute values of the material properties, while satisfying additional constrains such as a constant $\frac{E_L}{E_S}$ value. The critical strain of the metamaterial increases with $\frac{E_L}{E_S}$, while the ratio of the elastic modulus of the metamaterial to that of the ligament material, $\frac{E^*}{E_L}$, decreases with $\frac{E_L}{E_S}$ (Figure 3). In the rage of $\frac{E_L}{E_S}$ values between 0.1 and 10, the trend-line of changes in the critical strain and $\frac{E^*}{E_S}$ could be described using a power law (Figure 3). The power law exponents were different for the different void shapes considered here. While studying the change in the critical strain, the four-fold type 2 showed the highest power law exponents and the four-fold type 1 showed the lowest exponents (Figure 3). This suggests that geometrical features such as void geometry modulate the effects of material distribution on the critical strain of multi-material metamaterials. The plots in figure 3a-c show the strain distributions in four unit cells at the middle part of each structure for the lowest and highest values of $\frac{E_L}{E_S}$. The contours indicate that the vertical ligaments, the vertical ligaments aligned along the compressive load directions, experience high strain when the stiffness of ligaments is considerably lower than squares ($\frac{E_L}{E_S} = 0.1$). In contrast, squares experience high strains when the ligaments are stiffer. However, the results for the structures with four-fold type two voids illustrates that the slenderness of the ligaments can highly influence the level of strains in the ligaments even when the ligaments are stiffer than squares. Supplementary videos V1-3 [27] display the strain evolution and the precedence of instability in the studied structures while $\frac{E_L}{E_S} = 0.1, 1.0, 10$. When the shape of the ligaments can preserve the mode of buckling in the structures with voids four-fold type one and two (i.e., respectively side buckling and symmetric compaction), increasing the stiffness ratio ($\frac{E_L}{E_S}$) can transform the mode of buckling from symmetric compaction to side buckling in the structures with circular voids. Figure 3d depict the buckling modes for the give ratios of material properties ($\frac{E_L}{E_S} = 0.1, 0.32, 1, 3.2, 10$) and void shapes. The influence of geometrical imperfection in the transition from symmetric compaction to side buckling in the structures with circular voids has been proposed in form of a color ramp in figure 3d.

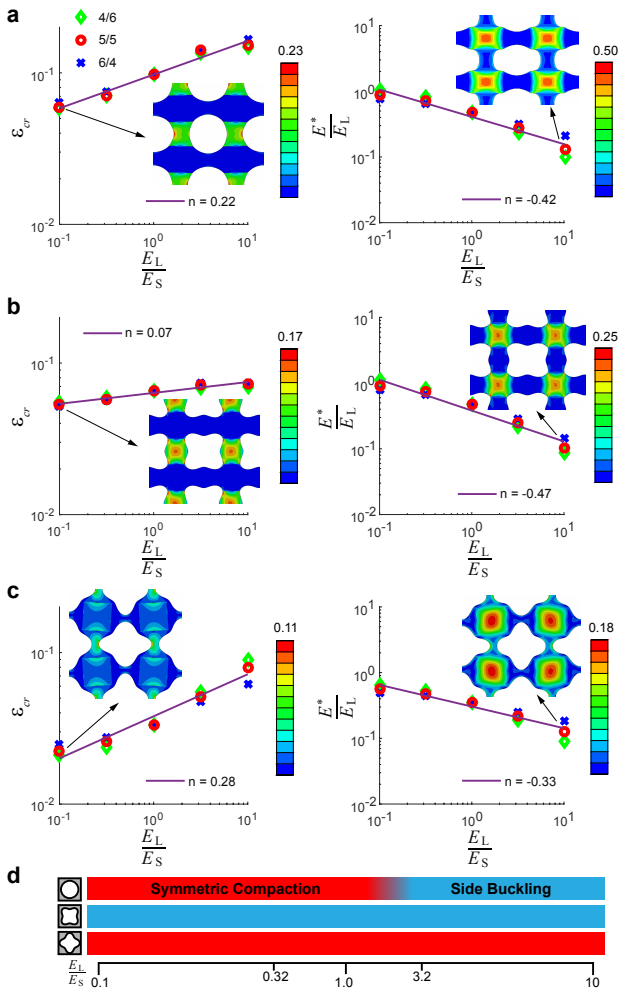

Figure 3

The critical strain and normalized elastic modulus of the metamaterials based on circular (a), four-fold type 1 (b), and four-fold type 2 (c) void shapes. The strain distributions are also depicted for the smallest and largest E_L/E_S values. The instability modes for different void shapes are presented in subfigure d. The color ramp in 3d highlights the influence of geometrical imperfection in the transition from symmetric compaction to side buckling in metamaterials with circular voids.

Quantitatively speaking, void shape alone could change the critical strain by up to 3-folds, while up to 9-fold difference in the critical strain was achieved when the effects of void shape were combined with those of material distribution.

To better understand the changes in the critical strain with $\frac{E_L}{E_S}$, we used the first-order approximations available from the linear theory of stability [25,26]. There are two competing modes of instability, namely symmetric compaction and side buckling. Symmetric compaction is caused by the buckling of individual ligaments and is, thus, a specific type of local buckling. Side buckling, on the other hand, is the global buckling of the cellular structures as a whole.

The critical load of individual ligaments is given by:

$$P_{cr,L} = \frac{\pi^2 E_L w^3 t}{12(k_L a)^2} \tag{2}$$

where w is the equivalent width of the ligament, t is the thickness of the ligament, a is the length of the ligament, and k_L is a factor dependent on the boundary conditions. The critical load of the entire cellular structure per unit cell, P_{cr}^*, is:

$$P_{cr}^* = \frac{\pi^2 E^* L^3 t}{n12(k^* L)^2} \tag{3}$$

where L is the length of the cellular structure, E^* is the elastic modulus of the cellular structure, t is the thickness of the cellular structure, n is the number of the unit cells along each edge of the specimen, and k^* is a factor dependent on the boundary conditions of the cellular structure.

Replacing $n = 8$ and $L = 16a$ in Equation (3) and assuming $k_L \approx k^*$, the ratio of the side buckling critical load, P_{cr}^*, to that of symmetric compaction, $P_{cr,L}$, could be written as

$$\frac{P_{cr}^*}{P_{cr,L}} \approx 2\left(\frac{E^*}{E_L}\right)\left(\frac{a}{w}\right)^3 \tag{4}$$

It could therefore be concluded that either side buckling or symmetric compaction could occur depending on the stiffness of the cellular structure as compared to that of the ligament and the shape of the voids. Considering the facts that for the circular void shapes, $w \approx a$, for four-fold type 1, $w > a$ (due to the barrel-like shape of the ligaments), and for four-fold type 2, $w \ll a$ (due to the cut-outs in the ligaments) and replacing for $\frac{E^*}{E_L}$ from the values found in Figure 3, we found that the predictions buckling modes based on Equation (4) are in agreement with those found computationally (Figure 3d). To put Equation (3) in perspective, the term $\left(\frac{a}{w}\right)^3$ represents the effects of geometrical design on the onset of instability and instability mode. The cubic nature of this term highlights the strong effects that small changes in the geometrical design could have on the instability behavior of the metamaterial. The term $\frac{E^*}{E_L}$, on the other hand, represents the effects of material

distribution on the instability behavior. The power law relationship between $\frac{E_L}{E_S}$ and $\frac{E^*}{E_L}$ (Figure 3) shows that the spatial distribution of the different materials could also strongly influence the instability behavior. As is clear from the different power law exponents found for different void shapes, there are also modulations between the effects of geometrical design and those of material combination that cannot be captured by the simplified analytical models available from the linear theory of stability.

In summary, the presented design of multi-material metamaterials allows for adjustment of both critical stress and critical strain. Critical stress could be changed independently from the critical strain by keeping the ratio of the elastic modulus of the ligament material to that of the square material constant while changing the absolute values of the elastic moduli. A power law relationship between $\frac{E_L}{E_S}$ and critical strain was found for $\frac{E_L}{E_S}$ values between 0.1 and 10. We also found that geometrical features such as void geometry not only affect the critical strain themselves but also modulate the effects of the parameters describing material distribution (e.g. $\frac{E_L}{E_S}$ and $\frac{a}{b}$). To put those effects in perspective, geometrical features could change the critical strain by up to 3-folds while up to 9-fold change in critical strain could be achieved by combining the effects of geometrical features with those of material distribution.

References

[1] J. H. Lee, J. P. Singer, and E. L. Thomas, *Micro-/nanostructured mechanical metamaterials*, Adv Mater **24**, 4782 (2012).

[2] A. A. Zadpoor, *Mechanical meta-materials*, Mater Horiz **3**, 371 (2016).

[3] B. Florijn, C. Coulais, and M. van Hecke, *Programmable mechanical metamaterials*, Phys Rev Lett **113**, 175503 (2014).

[4] Z. G. Nicolaou and A. E. Motter, *Mechanical metamaterials with negative compressibility transitions*, Nat Mater **11**, 608 (2012).

[5] X. Zheng *et al.*, *Ultralight, ultrastiff mechanical metamaterials*, Science **344**, 1373 (2014).

[6] Y. Brechet and J. D. Embury, *Architectured materials: Expanding materials space*, Scripta Mater **68**, 1 (2013).

[7] J. T. Overvelde, J. C. Weaver, C. Hoberman, and K. Bertoldi, *Rational design of reconfigurable prismatic architected materials*, Nature **541**, 347 (2017).

[8] R. Hedayati, A. M. Leeflang, and A. A. Zadpoor, *Additively manufactured metallic pentamode meta-materials*, Appl Phys Lett **110**, 091905 (2017).

[9] L. R. Meza, S. Das, and J. R. Greer, *Strong, lightweight, and recoverable three-dimensional ceramic nanolattices*, Science **345**, 1322 (2014).

[10] J. T. Overvelde, T. A. de Jong, Y. Shevchenko, S. A. Becerra, G. M. Whitesides, J. C. Weaver, C. Hoberman, and K. Bertoldi, *A three-dimensional actuated origami-inspired transformable metamaterial with multiple degrees of freedom*, Nat Commun **7**, 10929 (2016).

[11] J. L. Silverberg, J.-H. Na, A. A. Evans, B. Liu, T. C. Hull, Christian D. Santangelo, R. J. Lang, R. C. Hayward, and I. Cohen, *Origami structures with a critical transition to bistability arising from hidden degrees of freedom*, Nat Mater **14**, 389 (2015).

[12] T. Castle, Y. Cho, X. Gong, E. Jung, D. M. Sussman, S. Yang, and R. D. Kamien, *Making the cut: lattice kirigami rules*, Phys Rev Lett **113**, 245502 (2014).

[13] B. G. Chen, B. Liu, A. A. Evans, J. Paulose, I. Cohen, V. Vitelli, and C. D. Santangelo, *Topological Mechanics of Origami and Kirigami*, Phys Rev Lett **116**, 135501 (2016).

[14] A. Rafsanjani and K. Bertoldi, *Buckling-Induced Kirigami*, Phys Rev Lett **118**, 084301 (2017).

[15] G. W. Milton and A. V. Cherkaev, *Which Elasticity Tensors are Realizable?*, J Eng Mater Technol **117**, 483 (1995).

[16] S. Babaee, J. Shim, J. C. Weaver, E. R. Chen, N. Patel, and K. Bertoldi, *3D soft metamaterials with negative Poisson's ratio*, Adv Mater **25**, 5044 (2013).

[17] K. Bertoldi, P. M. Reis, S. Willshaw, and T. Mullin, *Negative Poisson's ratio behavior induced by an elastic instability*, Adv Mater **22**, 361 (2010).

[18] J. T. B. Overvelde, S. Shan, and K. Bertoldi, *Compaction Through Buckling in 2D Periodic, Soft and Porous Structures: Effect of Pore Shape*, Adv Mater **24**, 2337 (2012).

[19] B. Florijn, C. Coulais, and M. van Hecke, *Programmable mechanical metamaterials: the role of geometry*, Soft Matter **12**, 8736 (2016).

[20] S. Janbaz, H. Weinans, and A. A. Zadpoor, *Geometry-based control of instability patterns in cellular soft matter*, RSC Adv **6**, 20431 (2016).
[21] J. T. B. Overvelde and K. Bertoldi, *Relating pore shape to the non-linear response of periodic elastomeric structures*, J Mech Phys Solids **64**, 351 (2014).
[22] J. Hiller and H. Lipson, *Tunable digital material properties for 3D voxel printers*, Rapid Prototyp J **16**, 241 (2010).
[23] C. Coulais, E. Teomy, K. de Reus, Y. Shokef, and M. van Hecke, *Combinatorial design of textured mechanical metamaterials*, Nature **535**, 529 (2016).
[24] D. Yang, B. Mosadegh, A. Ainla, B. Lee, F. Khashai, Z. Suo, K. Bertoldi, and G. M. Whitesides, *Buckling of Elastomeric Beams Enables Actuation of Soft Machines*, Adv Mater **27**, 6323 (2015).
[25] D. O. Brush and B. O. Almroth, *Buckling of bars, plates, and shells*, (1975).
[26] S. P. Timoshenko and J. M. Gere, *Theory of elastic stability*, (1961).
[27] See Supplemental Material at [https://doi.org/10.1103/PhysRevApplied.9.064013] for the *evolution of strain patterns in multi-material mechanical metamaterials.*

Chapter 4

Ultra-tunable buckling-driven soft actuators

(Submitted)

Buckling, which was once considered the epitome of design failure, has been harnessed during last few years to develop mechanical metamaterials with advanced functionalities. Soft robotics in general and soft actuators in particular could greatly benefit from such designer materials. Unlocking the great potential of buckling-driven actuators is, however, contingent on resolving the main limitation of the designs presented to date, namely limited tunability. Here, we present multi-material buckling-driven metamaterials with an unprecedented level of tunability. We combined rational design approaches based on predictive computational models with advanced multi-material additive manufacturing techniques to 3D print cellular materials with arbitrary distributions of flexible and stiff materials in the central and corner parts of their unit cells. Using the geometry and spatial distribution of material properties as the main design parameters, we developed actuators whose actuation force and actuation amplitude could be adjusted both independently and concomitantly within wide ranges. Our designs also resulted in the emergence of a new lowest instability mode, i.e. double-side buckling, in addition to the already known modes of side-buckling and symmetric compaction. Finally, we proposed a general approach that predisposes the actuators, enabling them to reliably actuate their higher instability modes without the need for additional boundary conditions or fixtures. To demonstrate this approach, we created a rotational actuator that clones the functionality of mechanical machines. The potential of the presented designs in robotics is then demonstrated by applying them as a force switch, kinematic controllers, and a pick and place end-effector.

Mechanical metamaterials [1-4] enable development of advanced materials with novel functionalities that originate from their unusual mechanical properties. The unusual mechanical properties often include either negative properties or extreme properties. Examples of negative properties are negative Poisson's ratio [5-7], negative thermal expansion coefficient [8-10], negative compressibility [11], and negative stiffness [12,13]. Extremely high stiffness to mass ratio [14-16] and extremely high (low) resistance against deformation in specific directions [17,18] are examples of the extreme properties. Such otherwise "impossible" material properties allow for new approaches to material design. Soft mechanical metamaterials [19-22] have been of particular interest in this regard, as the combination of large recoverable (asymmetric) deformations, nonlinearity, and instability provides a fertile ground for development of novel properties and functionalities for application in, among other areas, soft robotics.

Within the context of soft robotics, the usually undesired concept of instability could be harnessed to create tunable actuators. Soft actuators with certain levels of tunability such as the possibility to adjust the onset of instability or to switch between simple instability modes (e.g. side buckling vs. symmetric compaction) have been demonstrated before [19,23,24]. The level of tunability has, however, been limited and far below what would be required to make this a versatile design strategy for soft actuators. The main challenge lies in achieving complex activation modes in 3D with a highly adjustable onset of instability. This is, however, difficult to achieve as most designs presented to have been limited to 2D [6,23,24] and show a limited range of strains within which the onset of instability could be adjusted [23,24]. Even more difficult to achieve is a complex actuation pattern in 3D, as it would require activation of complex instability modes. Although soft mechanical metamaterials exhibit very complex activation patterns in their higher modes of instability, reliable activation of those modes is not easily achievable with simple forces and without imposing additional constrains that limit the applicability of the actuator.

Versatile application of buckling-driven soft actuators is possible only when they satisfy three major requirements. First, it should be possible to adjust the actuation force and actuation amplitude within wide ranges. Second, the designs should allow for both independent and concomitant adjustment of actuation force and actuation amplitude. Finally, the actuation modes should cover a large number of possible modes including not only simple actuation modes but also a rich set of more complex actuation patterns. These requirements are ordered according to their difficulty. For example, it is much more challenging to design buckling-driven actuators that actuate in novel modes as compared to adjusting the actuation force/amplitude of an already existing actuation mode. Here, we present a class of 3D mechanical metamaterials with an unprecedented level of tunability, enabling them to satisfy all the above-mentioned requirements.

We designed 3D cellular arrays made by repeating single unit cells (Figure 1a, S1) in all spatial directions. As a consequence of the voids, twelve compliant connections were formed within each representative unit cell (Figure 1a). We divided the unit cells into two parts, namely the corner and central parts, each of which with a different set of mechanical properties (flexible or stiff). The ratio of the mechanical properties of both parts were varied between values $\ll 1$ and values $\gg 1$. Nine different types of cellular mechanical metamaterials with three different types of unit cells and with three different ratios of the mechanical properties of the corner parts to the central parts were 3D printed using a multi-material additive manufacturing technique. The buckling and post-buckling behaviors of all nine types of the cellular structures were also studied using computational models. The computational models were extended to include a wider study of how unit cell types and spatial distributions of flexible and stiff materials influence the actuation force and actuation amplitude. Since the actuators work on the basis of buckling, the strain, ε_{cr}, and stress, σ_{cr}, at the onset of instability respectively regulate the actuation force and actuation amplitude, which is why we discuss our results in terms of those variables.

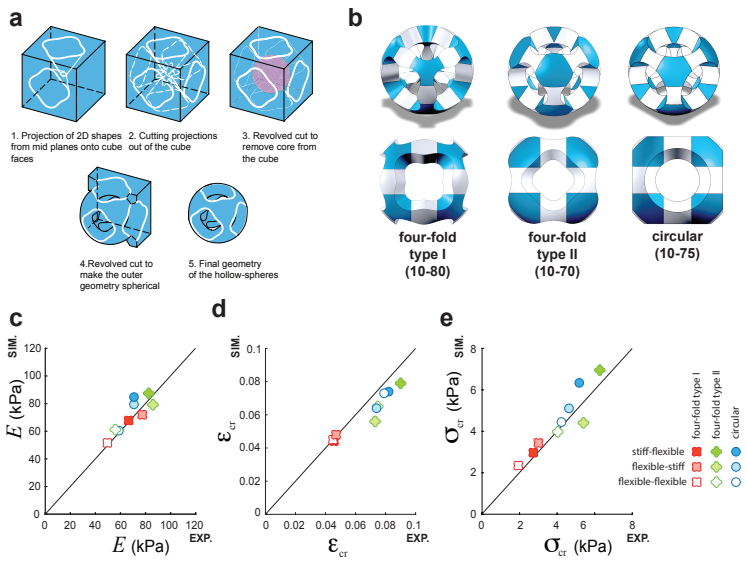

Figure 1
(a) Projection of 2D shapes to the six faces of a cube upon which the designs of the voids are based. (b) The representative unit cells of the cellular structures considered in this study. The translational unit cells, which could be repeated in different directions to create the cellular structure, are somewhat different (see Figure S1). The labels 10-70 to 10-80 specify the ratio of the projected shapes to the faces of reference cube, meaning that the projected geometries were scaled up to 7, 7.5, or 8 times of the 2D shapes on the mid-planes. (c-e) Comparison between the experimental and computational values of the Young's moduli, critical strains, and critical stresses for a selection of the designs considered here.

Regarding the first requirement, we found that varying the void geometry and spatial distribution of the material properties are effective tools for adjusting the stiffness of the actuators, E, the actuation force (critical stress, σ_{cr}), and the actuation amplitude (critical strain, ε_{cr}) (Figures 1-2). For the designs considered here, the stiffness, actuation amplitude, and actuation force respectively changed by 4 (35-146 kPa), 5 (0.018-0.086), and 16 (0.073-12.02 kPa) folds. Computational predictions were generally in good agreement with experimental data (Figure 1c-e), meaning that the behavior of the proposed actuators could be predicted in advance. Computational models were therefore used for the rational design of buckling-driven actuators, as demonstrated below.

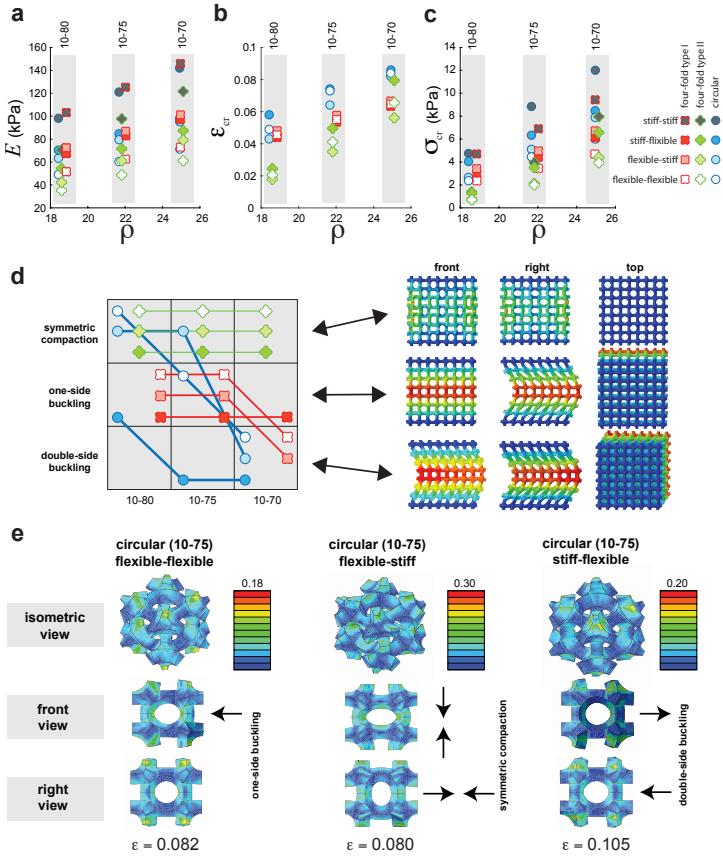

Figure 2
The effects of the spatial distribution of material properties and geometrical design including void shape and relative density, ρ, on the actuation behavior of multi-material metamaterials studied here: (a) total stiffness, (b) critical strain, and (c) critical stress. (d) A map of how different design parameters influence the first instability (actuation) mode of the metamaterials. The first instability modes include symmetric compaction, single-side buckling, and double-side buckling. (e) The strain distribution in the middle unit cells for the cellular structures with circular voids and with different combinations of material properties in the central and corner parts of the unit cells.

Independent as well as coupled adjustment of actuation force and actuation amplitude (second design requirement) is usually very challenging to achieve, when the only design variable is the void geometry. Multi-material additive manufacturing offers the additional freedom to arbitrarily distribute the stiff and flexible materials in space [25-27]. When applied in conjunction with geometrical design, multi-material designs form a firm basis for achieving the second design requirement. For example, the actuation force of the metamaterials with four-fold type one geometry substantially changed between stiff-flexible, flexible-stiff, and flexible-flexible designs while the actuation amplitude, remained practically the same (Figure 1d-e). On the other hand, simultaneous adjustment of the actuation force and actuation amplitude were possible when using the four-fold type II as the base geometry and by varying the spatial distribution of the flexible and stiff materials (Figure 1d-e). Taken together, these design parameters allow for designing a wide range of buckling-driven actuators. For example, combining large amplitude with small force is critical for applications where delicate objects such as soft tissues need to be manipulated. For such sensitive applications, the buckling could not only be used as the main actuation mechanism but may also serve as a safety switch preventing the actuation force to exceed the levels considered safe for the patient.

Designing novel as well as complex actuation modes was the most challenging design requirement and required unprecedented approaches that took full advantage of the form-freedom and material distribution-freedom offered by multi-material additive manufacturing techniques. The mere point of combining flexible and stiff materials in the central and corner regions resulted in the emergence of a new instability (actuation) mode, namely double-side buckling (Figures 2, 3). The cellular materials studied to date [19,23,24] usually exhibit one of the two instability modes of side buckling or symmetric compaction. One of the reasons has been that most such metamaterials have been studied in 2D where double-side buckling is not possible. However, even a handful of 3D designs [19,28,29] did not report double-side buckling. Our computational models clearly showed that not only geometrical design parameters such as the type of the unit cell and porosity but also the distribution of material properties influence the type of the instability mode (Figure 2d). That is because both types of design parameters could substantially change the distribution of strains in each of the 12 compliant links making up the unit cells (Figure 2e).

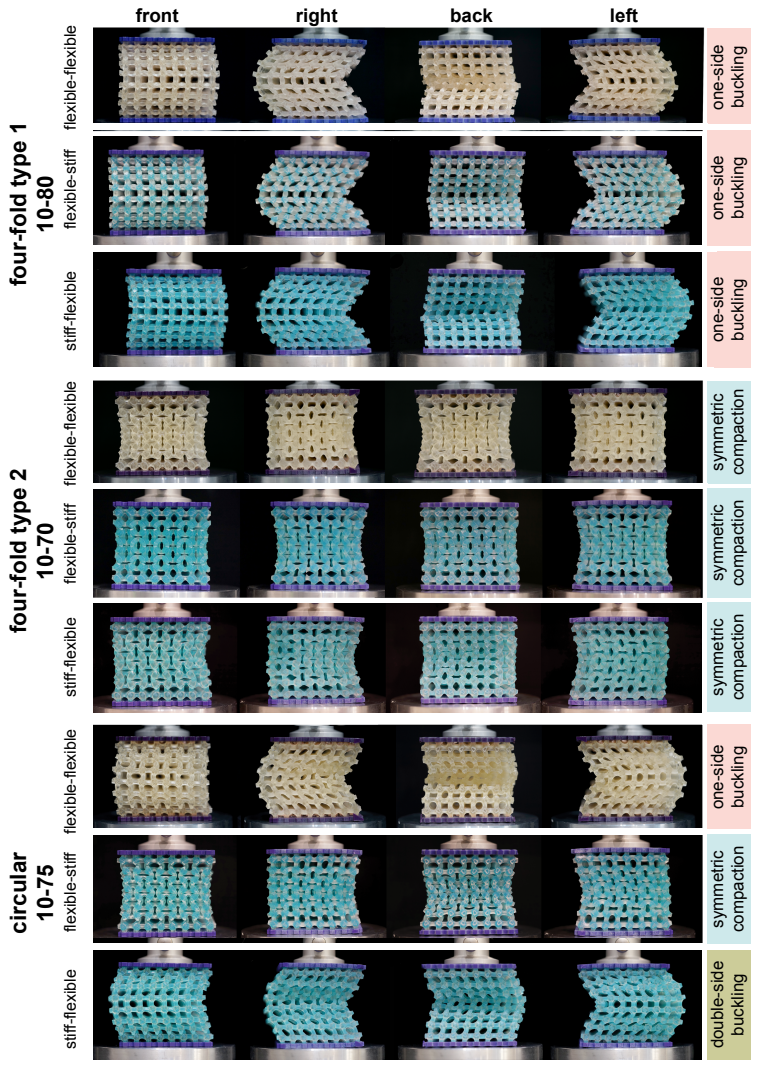

Figure 3
Different views of the first instability (actuation) modes observed experimentally. There are three types of instability modes including symmetric compaction, side-buckling, and double-side buckling. The nominal dimensions of all specimens were 90×90×90 mm. All photographs were taken at 20 mm axial displacement.

When trying to meet the third design requirement, even more important than the emergence of a new type of instability mode is actuating one of the higher modes of metamaterial instability. Our extensive computational study showed that multi-material metamaterials possess a very rich physics and very complex higher instability

modes. The problem, however, is that it is usually not possible to reliably actuate any of those modes, because the lower modes are activated before reaching the threshold required for activating the higher modes. Adding boundary conditions and designing fixtures that apply the actuation force in specific ways may enable activation of some of the higher instability modes [30,31]. However, that calls for a complex design process and mode-specific apparatus that will limit the practical application of such buckling-driven actuators. Here, we propose a simple and generally applicable technique for activating the higher modes of instability without any need for additional boundary conditions or fixtures. In this approach, we pre-dispose the mechanical metamaterials such that the first mode they activate is the desired mode of instability. We started off by computationally predicting the shape of the higher instability modes. The desired actuation mode was then selected from the computationally predicted modes of instability. We then introduced the computed mode shape into the geometry of our mechanical metamaterial as imperfections with different amplitudes (i.e. imperfection severity). This allowed for reliable actuation of the desired mode without any need for additional boundary conditions or clamping devices.

To demonstrate this general approach, we chose a rotational mode of actuation. Creating rotational actuation is generally challenging as highlighted by others [28]. However, rotational actuation is crucial for the concept of machine matter, as it bring us one step closer to the usual mode of mechanical machines, i.e. rotation [28]. We introduced the predicted mode shape as imperfections with different amplitudes to the original shape and studied how the imperfection amplitude as well as other design parameters affected the mechanical behavior and characteristic curves (rotational angle vs. axial strain) of the designed metamaterials. The measured stress-strain curves of the additively manufactured specimens (Figure 4a) closely matched those predicted computationally (Figure 4b). The specimens clearly showed a rotational behavior (supplementary video V1 [32], Figure 4a, c) with characteristic curves that were strongly dependent on the amplitude of the introduced imperfections and the projection ratio (Figure 4d-g). Not only the scale but also the general trend of the characteristic curve changed with the imperfection amplitude (Figure 4d). Smaller imperfections led to a two-stage actuation with limited rotations for the smaller values of axial strain followed by a second stage where the rotational angle sharply increased with axial strain (Figure 4d). Larger imperfections, however, made the rotation angles increase faster even for small axial strains and blurred the boundary between both stages (Figure 4d). The effects of material distribution on the characteristic curve were small in comparison (Figure 4e-g). The material properties of the central and corner parts, however, significantly influenced the actuation force (axial stress), meaning that the characteristic curves could be adjusted independently from the actuation forces.

The near-perfect decoupling of the actuation force from actuation kinematics presents a valuable tool for designing buckling-driven actuators for a multitude of applications.

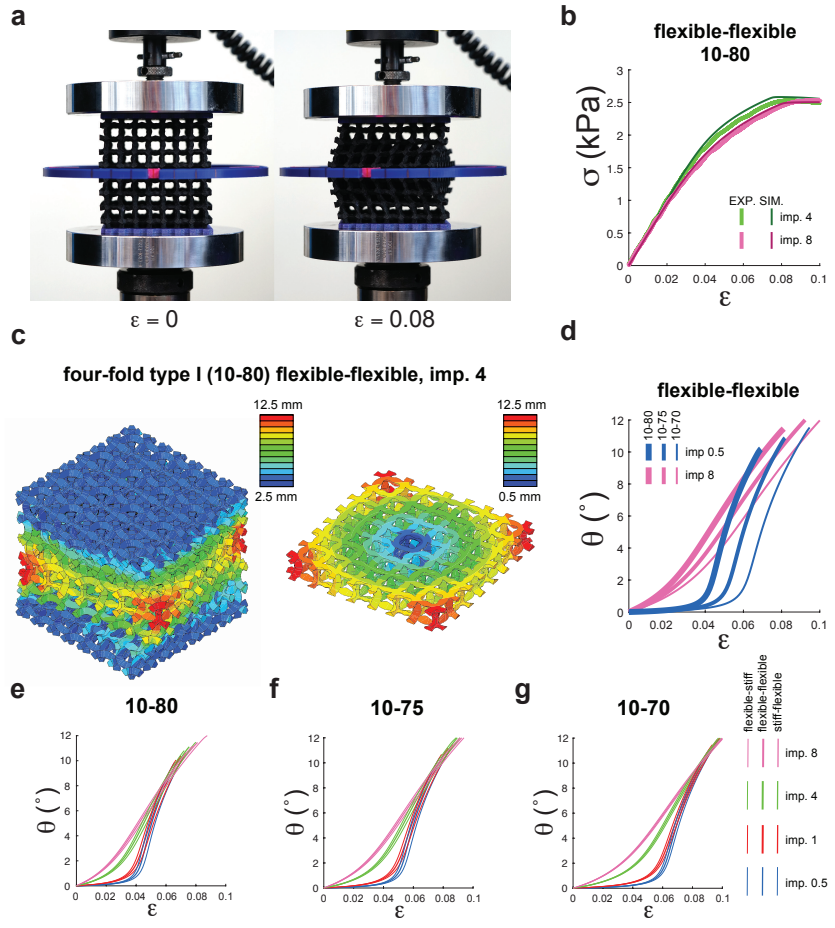

Figure 4
We actuated higher modes of instability by introducing imperfections that pre-disposed the cellular structure so that it would buckle under the desired mode. (a) To demonstrate this general approach, we fabricated a rotating actuator that was based on cellular structures with four-fold type I void geometry. In this case, imperfections (scale= 4) were introduced to a cellular structure with 10-80 projection ratio and flexible-flexible distribution of materials to make it buckle under third instability mode without any need for boundary conditions or fixtures. (b) Comparison between experimental and computational values of axial stress vs. axial strain for two specimens with imperfection scales of 4 and 8. (c) The third instability mode as predicted by our computational models. (d) The effects of geometrical design and imperfection magnitude on the characteristic curve of the actuator (i.e. rotational angle vs. axial strain). (e-g) The effects of imperfection magnitude and spatial distribution of materials on the characteristic curves calculated for three different relative densities.

To demonstrate some of the potential applications of the proposed concepts in robotics, we performed three experiments in which our soft actuators were used as a force switch, as kinematic (position/velocity) controllers, and as a pick and place grasping mechanism (Figure 5). As previously mentioned, the buckling mechanism could function as a force switch, allowing us to keep the force below a certain threshold over a large range of displacements. In the case of our experiment, the buckling mechanism prevented the load applied to the egg to go beyond 40 N over a range of >15 mm (supplementary video V2 [32], Figure 5a). Such a large range of displacement will translate into a very comfortable tolerance for controlling the movements of robotic arms. In a second experiment, we used the rotational actuation modes (Figure 4) of the specimens with different levels of imperfections to control the movement patterns of two table tennis balls (supplementary video V3 [32], Figure 5b). The different levels of imperfection introduced to both cellular structures caused very distinct movement patterns (Figure 5b). Moreover, higher imperfection amplitudes linearized the behavior of the rotational actuators, while instability patterns dominated the kinematics of the actuators with smaller imperfection amplitudes. Finally, the same rotational mode of instability was used to design a pick and place ratchet and pawl assisted grasping mechanism, where the rotating mechanism locked into the object with the initial push enabling it to be moved to a new position at which point a second push released the object (supplementary video V4 [32], Figure 5c).

The work presented here clearly shows the importance of form-freedom as well as freedom in the spatial distribution of multiple materials when trying to design buckling-driven soft actuators. Predictive computational models are an important part of the rational design process as well. When taken full advantage of, these three components enable designing actuators that are highly tunable not only in terms of the actuation force and actuation amplitude but, more importantly, in terms of the actuation mode. Of vital importance to the generality of the approach is the possibility to activate the higher modes of instability. The higher instability modes are usually so rich in geometry that should be able to provide the basis for any practically relevant actuation modes either individually or in combination with each other. Purposeful introduction of imperfections into the metamaterial design could be also used for improving the reliability of actuation. Even when the intention is to activate the metamaterials through their first instability mode, another mode (e.g. second or third modes) may be actuated particularly when the critical strains of those modes are too to that of the first one. Relatively small irregularities caused by the manufacturing process could then lead the metamaterial to actuate another (undesired) mode. Purposeful imperfections ensure that only the desired mode is activated.

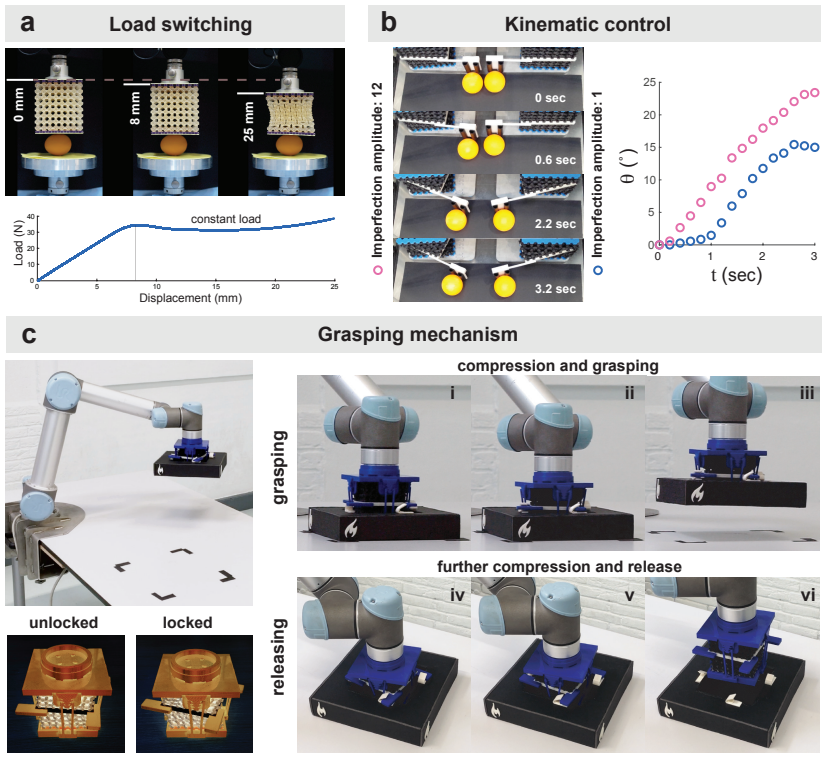

Figure 5
Some potential applications of the proposed soft actuators in robotics. (a) A force switch. The buckling of a sample cellular structure (four-fold type II $(\phi, r, d, n) = (0.45, 0.8, -1, 4)$, projection ratio: 10-70) allows for keeping the force applied to a raw egg almost constant and below 40 N for a large range (>15 mm) of displacements. (b) Kinematic (i.e. position/velocity) controllers. Two cellular structures (four-fold type I $(\phi, r, d, n) = (0.45, 0.7, +1, 4)$, projection ratio: 10-70) were pre-disposed to actuate their third instability mode (Figure 4) using two imperfection amplitudes of 12 and 1. The different imperfection amplitudes caused distinct movement patterns and different absolute values of the position angle for two table tennis balls moved by both actuators. (c) A pick and place ratchet and pawl assisted grasping mechanism as the end effector of a robotic arm. The rotational actuation mode of a cellular specimen (four-fold type I $(\phi, r, d, n) = (0.45, 0.7, +1, 4)$, projection ratio: 10-70, imperfection amplitude: 12) constrained between two clamps was used to lock the end effector into the object with the first push (i-iii). The clamps were linked to each other through four ratchet and pawl mechanisms. The object could then be moved to the desired locating at which point a second push releases it (iv-vi).

The rational design process advocated here means that the actuation pattern and actuation characteristics could be programmed into the fabric of the metamaterials, thereby eliminating the need for an interconnected network of distributed actuators, sensors, and controllers that are usually needed for achieving complex actuations [33].

Buckling-driven metamaterials could have important medical applications in wearable soft robotics such as exoskeletons and exosuits as well as robot-assisted surgery on soft tissues. Potential industrial applications are also numerous. Moreover, highly tunable buckling behavior could be used for designing switches that enforce a cut-off force, thereby ensuring (patient) safety.

References

[1] J. N. Grima and R. Caruana-Gauci, *Mechanical metamaterials: Materials that push back*, Nat Mater **11**, 565 (2012).

[2] T. Buckmann, N. Stenger, M. Kadic, J. Kaschke, A. Frolich, T. Kennerknecht, C. Eberl, M. Thiel, and M. Wegener, *Tailored 3D mechanical metamaterials made by dip-in direct-laser-writing optical lithography*, Adv Mater **24**, 2710 (2012).

[3] A. A. Zadpoor, *Mechanical meta-materials*, Mater. Horiz. **3**, 371 (2016).

[4] J. H. Lee, J. P. Singer, and E. L. Thomas, *Micro-/nanostructured mechanical metamaterials*, Adv Mater **24**, 4782 (2012).

[5] R. Lakes, *Foam Structures with a Negative Poisson's Ratio*, Science **235**, 1038 (1987).

[6] K. Bertoldi, P. M. Reis, S. Willshaw, and T. Mullin, *Negative Poisson's ratio behavior induced by an elastic instability*, Adv Mater **22**, 361 (2010).

[7] J. N. Grima, S. Winczewski, L. Mizzi, M. C. Grech, R. Cauchi, R. Gatt, D. Attard, K. W. Wojciechowski, and J. Rybicki, *Tailoring graphene to achieve negative Poisson's ratio properties*, Adv Mater **27**, 1455 (2015).

[8] Q. Wang, J. A. Jackson, Q. Ge, J. B. Hopkins, C. M. Spadaccini, and N. X. Fang, *Lightweight Mechanical Metamaterials with Tunable Negative Thermal Expansion*, Phys Rev Lett **117**, 175901 (2016).

[9] J. Qu, M. Kadic, A. Naber, and M. Wegener, *Micro-Structured Two-Component 3D Metamaterials with Negative Thermal-Expansion Coefficient from Positive Constituents*, Sci Rep **7**, 40643 (2017).

[10] R. Lakes, *Cellular solids with tunable positive or negative thermal expansion of unbounded magnitude*, Appl Phys Lett **90**, 221905 (2007).

[11] Z. G. Nicolaou and A. E. Motter, *Mechanical metamaterials with negative compressibility transitions*, Nat. Mater. **11**, 608 (2012).

[12] E. B. Duoss *et al.*, *Three-Dimensional Printing of Elastomeric, Cellular Architectures with Negative Stiffness*, Adv Funct Mater **24**, 4905 (2014).

[13] T. A. Hewage, K. L. Alderson, A. Alderson, and F. Scarpa, *Double-Negative Mechanical Metamaterials Displaying Simultaneous Negative Stiffness and Negative Poisson's Ratio Properties*, Adv Mater **28**, 10323 (2016).

[14] X. Zheng *et al.*, *Ultralight, ultrastiff mechanical metamaterials*, Science **344**, 1373 (2014).

[15] L. R. Meza, S. Das, and J. R. Greer, *Strong, lightweight, and recoverable three-dimensional ceramic nanolattices*, Science **345**, 1322 (2014).

[16] L. R. Meza, A. J. Zelhofer, N. Clarke, A. J. Mateos, D. M. Kochmann, and J. R. Greer, *Resilient 3D hierarchical architected metamaterials*, Proc Natl Acad Sci U S A **112**, 11502 (2015).

[17] M. Kadic, T. Bückmann, N. Stenger, M. Thiel, and M. Wegener, *On the practicability of pentamode mechanical metamaterials*, Appl Phys Lett **100**, 191901 (2012).

[18] G. W. Milton and A. V. Cherkaev, *Which Elasticity Tensors are Realizable?*, J. Eng. Mater. Technol. **117**, 483 (1995).

[19] S. Babaee, J. Shim, J. C. Weaver, E. R. Chen, N. Patel, and K. Bertoldi, *3D soft metamaterials with negative Poisson's ratio*, Adv Mater **25**, 5044 (2013).

[20] S. H. Kang, S. Shan, A. Kosmrlj, W. L. Noorduin, S. Shian, J. C. Weaver, D. R. Clarke, and K. Bertoldi, *Complex ordered patterns in mechanical instability induced geometrically frustrated triangular cellular structures*, Phys Rev Lett **112**, 098701 (2014).
[21] J. Shim, S. C. Shan, A. Kosmrlj, S. H. Kang, E. R. Chen, J. C. Weaver, and K. Bertoldi, *Harnessing instabilities for design of soft reconfigurable auxetic/chiral materials*, Soft Matter **9**, 8198 (2013).
[22] C. Coulais, D. Sounas, and A. Alu, *Static non-reciprocity in mechanical metamaterials*, Nature **542**, 461 (2017).
[23] J. T. B. Overvelde, S. Shan, and K. Bertoldi, *Compaction Through Buckling in 2D Periodic, Soft and Porous Structures: Effect of Pore Shape*, Adv Mater **24**, 2337 (2012).
[24] S. Janbaz, H. Weinans, and A. A. Zadpoor, *Geometry-based control of instability patterns in cellular soft matter*, RSC Adv. **6**, 20431 (2016).
[25] D. S. Engstrom, B. Porter, M. Pacios, and H. Bhaskaran, *Additive nanomanufacturing - A review*, J Mater Res **29**, 1792 (2014).
[26] A. R. Studart, *Additive manufacturing of biologically-inspired materials*, Chem Soc Rev **45**, 359 (2016).
[27] A. A. Zadpoor and J. Malda, *Additive Manufacturing of Biomaterials, Tissues, and Organs*, Ann Biomed Eng **45**, 1 (2017).
[28] T. Frenzel, M. Kadic, and M. Wegener, *Three-dimensional mechanical metamaterials with a twist*, Science **358**, 1072 (2017).
[29] X. Ren, J. H. Shen, P. Tranc, T. D. Ngo, and Y. M. Xie, *Design and characterisation of a tuneable 3D buckling-induced auxetic metamaterial*, Mater Des **139**, 336 (2018).
[30] D. Schaeffer and M. Golubitsky, *Boundary-Conditions and Mode Jumping in the Buckling of a Rectangular Plate*, Commun Math Phys **69**, 209 (1979).
[31] B. Florijn, C. Coulais, and M. van Hecke, *Programmable mechanical metamaterials*, Phys. Rev. Lett. **113**, 175503 (2014).
[32] See Supplemental Material at [URL].
[33] R. Hedayati, M. J. Mirzaali, L. Vergani, and A. A. Zadpoor, *Action-at-a-distance metamaterials: Distributed local actuation through far-field global forces*, Apl Mater **6**, 036101 (2018).
[34] G. Campoli, M. S. Borleffs, S. A. Yavari, R. Wauthle, H. Weinans, and A. A. Zadpoor, *Mechanical properties of open-cell metallic biomaterials manufactured using additive manufacturing*, Mater Design **49**, 957 (2013).

Supplementary information

Materials and methods summary

For each type of unit cell, four parameters, i.e. ϕ, r, d, n, determined the shape of the voids and, thus, ligaments (details below). To create the 3D unit cells, 2D void shapes were projected onto the six external tangential planes from the three major mid-planes of a hollow sphere with outside and inside diameters of 20 and 12.5 mm (Figure 1a). The symmetric voids were then formed by loft cutting through the internal and external void shapes. To ensure that the dimensions of the generated ligaments were in the same range and that the integrity of the unit cells were preserved, the projected 2D voids on the surfaces of the corresponding cube were respectively scaled by 7.0, 7.5 or 8.0 for the circular, four-fold type I, and four-fold type II void geometries.

An advanced multi-material 3D printer (Stratasys Object 350 Connex3, US) working on the basis of jetting multiple UV-curable polymers was used to 3D print nine cellular structures with the three different void shapes and three different ratios of the mechanical properties of the corner parts to central parts (i.e. 0.5, 1, and 2). The more compliant material used for 3D printing of the corner or central parts was Agilus (Stratasys, US) while the stiffer material was a digital combination of Agilus and Vero Cyan (Stratasys, US). Vero (a hard polymer) (Stratasys, US) was used to print the end clamps. A soluble support material (SUP706, Stratasys, US) was used to preserve the details of the structures during the printing process. The cellular structures were first cleaned manually and were then soaked in a solution of 2% sodium hydroxide (NaOH) and 1% sodium metasilicate (Na2SiO3) in water for 2 hours to completely dissolve the support material. Cellular structures were compressed with a strain rate of 1 mm/min using a Lloyd universal test bench (LR5K) equipped with a 100 N load cell. A digital camera (Sony A7R with a Sony FE 90 mm f/2.8 macro OSS lens) was used to capture the deformations of the specimens during the tests.

Computational models were built to study the instability behavior of the designed mechanical metamaterials under compression. A Neo-Hookean hyperplastic material model was used to describe the constitutive behavior of all materials. The material parameter (C_{10}) was determined according to the results of uniaxial tensile tests on base materials (details below). The instability modes were determined using an eigenvalue analysis and were then introduced for nonlinear analysis of the buckling and post-bucking behavior of the specimens. A nonlinear finite element solver (Abaqus Standard, ver. 6.14) was used for all simulations. Half-whole models were created for all the nine experimentally studied specimens and were discretized using ten-node hybrid tetrahedral elements (C3D10H). The nodes at the top and bottom

surfaces of the specimens were constrained to satisfy the clamping conditions. A reference point was allowed to translate in the vertical direction. The onset of instability was determined by finding the maximum curvature at the start of the nonlinear phase in the stress-strain curves. The stiffness of the cellular structures was calculated using the data from the middle part of linear region in the corresponding stress-strain curve of each specimen.

Geometric design

The 2D patterns used to design the geometry of the voids were generated using a rotational vector previously described in [24]. Three selected combinations of parameters resulted in the circular ($(\phi, r, d, n) = (0.45, 1.0, -, -)$), four-fold type I ($(\phi, r, d, n) = (0.45, 0.7, +1, 4)$), and four-fold type II ($(\phi, r, d, n) = (0.45, 0.8, -1, 4)$) voids symmetrically confined in a square with a length size of 2.5 mm. 2D void shapes were projected onto the six external tangential planes from the three major mid-planes of a hollow sphere with outside and inside diameters of 20 and 12.5 mm. The symmetric voids were then formed by cutting-loft through the internal and external void shapes forming a porous ball with 6 holes (Figure 1a). The projected 2D voids on the surfaces of the corresponding cube were respectively scaled up by 7.0, 7.5 and 8.0 times to create the *representative* unit cells with four-fold type II, circular, and four-fold type I void shapes. The selected projection ratios assured that the dimensions of the generated ligaments were similar and that the integrity of the buckliballs were preserved. The *translational* unit cell that could be repeated in different directions to create the cellular structure is somewhat different from the *representative* unit cells and is equal to the shared volume of the BCC assembly of nine unit-cells with a cube when the vertices of the cube are placed on the center of eight *representative* unit cells (Figure S1). To study the effects of the material properties on the buckling behavior of cellular structures, the representative unit cells were segmented into corner and central parts using six two-by-two parallel cutting planes resulting in ligaments with lengths of 25% of the external diameter of the unit cells. All four combinations of flexible and stiff material properties were used for the corner and central parts of the representative unit cells. The lattice structures based on the BCC arrangement of the unit cells, with a lattice parameter of $a = 22.5\ mm$ and comprising $4 \times 4 \times 4$ unit cells were selected to numerically study the instability behavior of mechanical metamaterials. Finally, two rigid clamps were included on both parallel ends of the structures to facilitate the clamping of the specimens during uniaxial compression tests (Figure S1b).

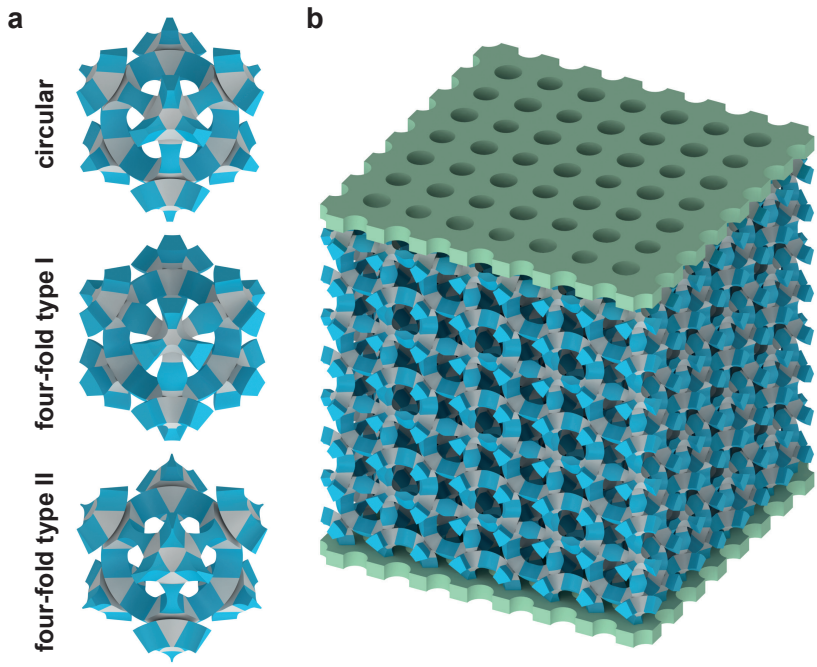

Figure S1
(a) Circular, four-fold type I, and four-fold type II *translational* unit cells. The gray and blue elements represent the corner and central parts of the unit cells. (b) A four-fold type II specimen comprising 4 × 4 × 4 unit cells and two rigid clamps at the top and bottom sides.

Mechanical properties of the base materials

We characterized the base (flexible and stiff) materials used for fabrication of the cellular structures. Strips ($80 \times 10 \times 3$ mm) of both types of materials were 3D printed with rigid end parts using a similar procedure as the one used for fabrication of multi-material cellular structures. Tensile tests under quasi-static condition were performed to measure the hyperelastic properties of the soft and stiff rubbers (Figure S2). The mean stress-strain curve of each group was used to evaluate the Neo-Hookean parameters (C_{10}) using the parameter estimation algorithm available in Abaqus, resulting in two values of $C_{10} = 115kPa$ and $C_{10} = 230kPa$ for the flexible and stiff polymers, respectively. SEM inspection of the flexible and stiff rubbers revealed no clear formation of void in the polymers. The materials were considered to be incompressible.

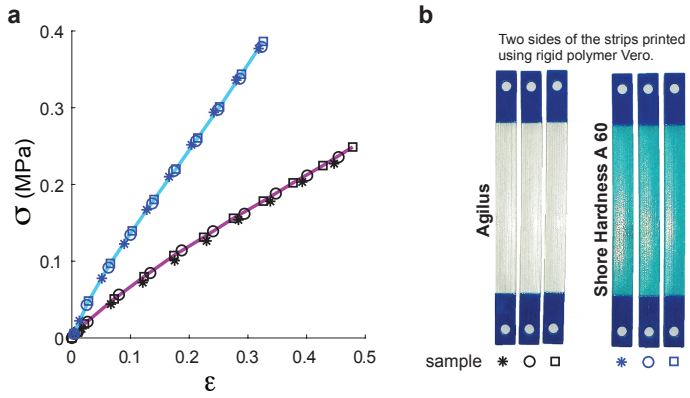

Figure S2
(a) The stress-strain curves obtained from tensile tests. (b) The tensile test strips (80 × 10 × 3 mm) with rigid end parts.

Computational models

As described in the summary of materials and methods, computational models were built to study the effects of geometrical design and material properties on the critical behavior of soft cellular structures. Some relatively small differences between the experimental observations and computational analyses were observed (Figures 1 and S3). We performed a microscopic analysis to study the reason for those deviations and found out that these differences are most likely due to the geometrical imperfections created by the fabrication process (Figure S4). The differences in material properties caused by different UV exposures (time, orientation) may also influence the experimental results. Some of the micro- and macro-scale geometrical imperfections observed in the specimens are visualized in Figure S4. Studies on 3D printed hard materials have also shown deviations of experimental observations from computational results caused by manufacturing imperfections even for small strains [34].

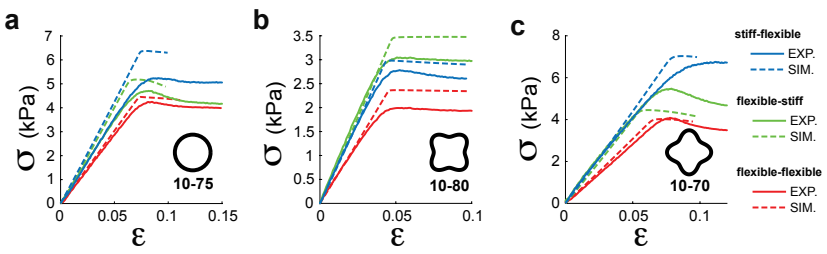

Figure S3
The experimental and computational stress-strain curves of (a) circular, (b) fourfold type I, and (c) fourfold type II specimens.

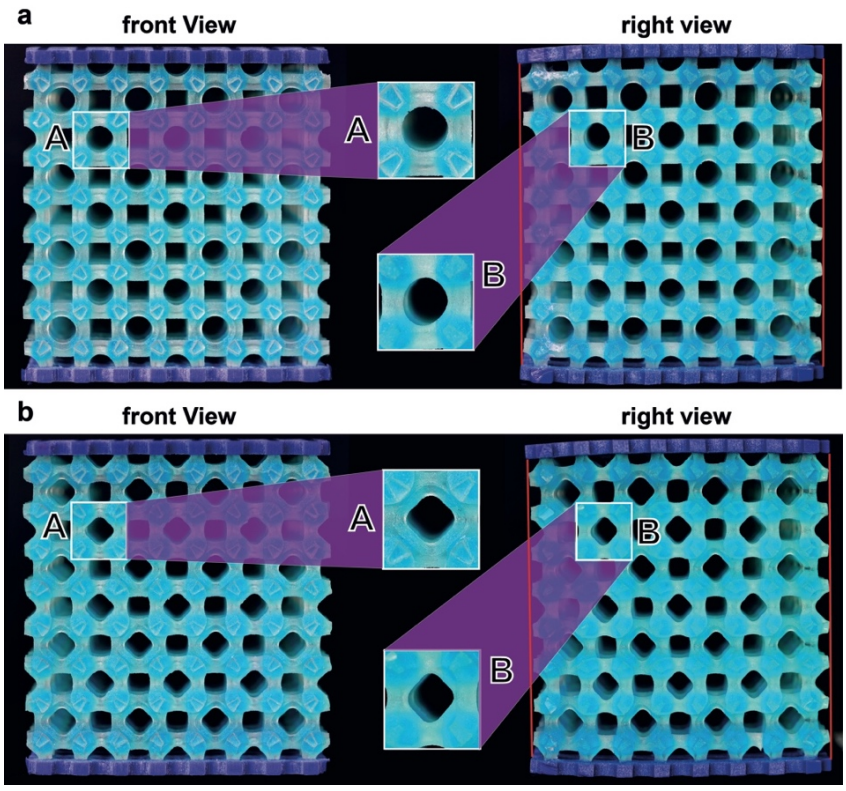

Figure S4. Microscopic and macroscopic geometrical imperfections were observed in the specimens produced using multi-material 3D printing. (a) The microscopic imperfections were manifested as deviations from the prescribed void shape. Macroscopically, a small deviation from straight line (to concavity) was observed in one of the faces of the specimen. (b) Similar macroscopic deviations are observed in four-fold type II specimens.

Activation of higher instability modes

Computational analysis revealed that the third instability mode for the cellular structures based on the four-fold type I voids is a rotational (twisting) mode regardless of the spatial distribution of the mechanical properties. The eigenvalue associated with this instability mode (according to linear buckling analysis) was < 2% higher than that of the first eigenvalue. To switch the order of instability modes, the post-buckling shape of the third mode was introduced as an imperfection modifying the geometry of the cellular structures. Two imperfection amplitudes (4 and 8) from the linear buckling analysis performed for a specific cellular structure (10-80, flexible-flexible, four-fold type I) were used to create the half-whole models that were then exported as geometry files, mirrored, and assembled using Blender (version 2.77) to create the geometry of full models. Similar to the previous specimens, two rigid clamps were included at the top and bottom of these specimens. To visualize the rotation of the specimens during compression, two lightweight rings (placed at the mid-section of

the specimens) were 3D printed using polylactic acid (PLA). The cellular structures were cleaned and compressed using an Instron testing machine (5500R equipped with a 1 kN load cell). The tests were performed both with and without the lightweight rings to ensure the addition of the rings does not significantly influence the results. Computational analysis using four different imperfection amplitudes (0.5, 1, 4, and 8) was used to evaluate the effects of the spatial distribution of the material properties, projection ratio, and the imperfection size on the characteristic curve of the cellular structures. Four reference points at the corners of the bottom side of the half-whole models were used to calculate the rotation of the mid-section of the full models when compressed.

Demonstration of the potential applications in robotics

To demonstrate some of the potential applications of the proposed concepts in robotics, we performed three experiments in which our soft actuators were used as a force switch, as kinematic (position/velocity) controllers, and as a pick and place grasping mechanism.

A raw egg was placed between the fixed compression plate and the free end of a cellular structure (four-fold type II, $(\phi, r, d, n) = (0.45, 0.8, -1, 4)$) (supplementary video 2, Figure 5a). The top side of the soft mechanical material was clamped to the moving compression plate. To avoid hard contact between the egg and the contact plates, two 1 mm thick semi-soft PVC plates were placed between the contact surfaces of the egg and the compression setup. To minimize possible bending moments, the egg was placed at the middle area of the soft actuator. The soft actuator was compressed after touching the egg for up to 25 mm (compression rate = 20 mm/min).

Using imperfections with different amplitudes (1 and 12), cellular solids (four-fold type I ($(\phi, r, d, n) = (0.45, 0.7, +1, 4)$, projection ratio: 10-70) were pre-disposed to actuate their third modes of instability (Figure 4) and were used as kinematic (position/velocity) controllers. Two rigid arms were fixed to two rings placed at the middle part of the soft actuators in order to push two table tennis balls when the soft actuators were compressed (supplementary video 3, Figure 5b). Both structures were compressed at the same time using a high compression rate of 500 mm/min. A MATLAB code was used to estimate the rotation angle of the rigid arms using a number of recorded images.

A soft cellular structure (four-fold type I $(\phi, r, d, n) = (0.45, 0.7, +1, 4)$, projection ratio 10-70, imperfection amplitude: 12) was pre-disposed to actuate its third mode of instability and was used as the actuator of a pick and place grasping mechanism. The cellular structure was constrained between two clamps that were linked together using four linear ratchet and pawl mechanisms (Figure S5). A gear ring at the middle part of the cellular structure was used for locking the end-effector into the picked objects with the first push. Further compression unlocked the ratchet and pawl mechanisms,

thereby releasing the grasped object. A universal robotic arm (Universal Robots, UR5, Denmark) was programmed to perform a pick and place task (supplementary video 4, Figure 5c) that visualized the function of the mechanism.

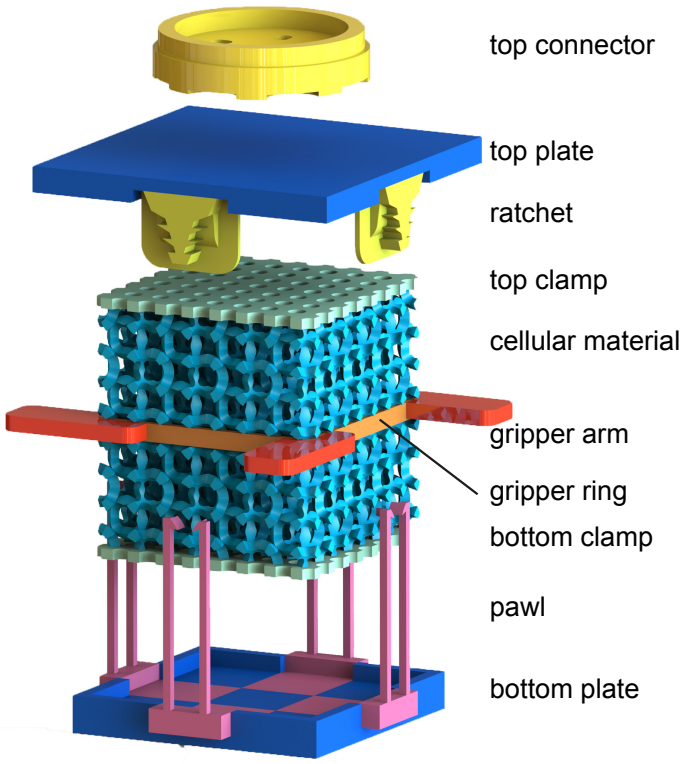

Figure S5
The components of the pick and place grasping mechanism. Four ratchet and pawl mechanisms enable the locking and unlocking of this rotational grasper.

Chapter 5

Shape-matching soft mechanical metamaterials

Scientific Reports (2018, 8, 965)

Architectured materials with rationally designed topologies could be used to create mechanical metamaterials with unprecedented or rare properties and functionalities. Here, we introduce "shape-matching" metamaterials where the topology of cellular structures comprising auxetic and conventional unit cells is designed so as to achieve a pre-defined shape upon deformation. We used computational models to forward-map the space of planar shapes to the space of topological designs. The validity of the underlying computational models was first demonstrated by comparing their predictions with experimental observations on specimens fabricated with indirect additive manufacturing. The forward-maps were then used to devise the topology of cellular structures that approximate the arbitrary shapes described by random Fourier's series. Finally, we show that the presented metamaterials could match the contours of three real objects including a scapula model, a pumpkin, and a Delft Blue pottery piece. Shape-matching materials have potential applications in soft robotics and wearable (medical) devices.

Mechanical metamaterials are materials whose macro-scale properties such as unusual deformation characteristics directly originate from their (small-scale) topological design [1–4]. Rational topological design of metamaterials could lead to properties and functionalities not usually offered by natural materials such as negative Poisson's ratio (auxetics) [5–7], negative compressibility [4], elastic hysteresis [8], independent tailoring of elastic properties [9], and snapping deformations [10], and shape-changing with vibration-mitigation capability [11] and out-of-plane deformation through 3D design of architectured metamaterials [12].

Metamaterials have also potential applications in shape-changing materials that are kinematically inspired by kirigami/origami-based designs [13], fractal cuts [14], deployable morphing [15], pattern switching [16], or strain amplification elements working through auxetic unit cells [17]. A novel objective in the design of shape-changing metamaterials is achieving a pre-defined shape upon loading through what we here call "shape-matching" materials.

Shape-matching metamaterials have a myriad of potential applications most notably in soft robotics [18], [19] and wearable (medical) devices. For example, shape-matching metamaterials could be used to design soft grippers that grip delicate objects with the maximum surface contact and, thus, minimum contact force. Wearable (medical) devices such as exosuits [20], prosthetics and orthotics [21], and tunable mechanical memory [22] are the other potential areas of application. Finally, the fashion design industry [23] may also be able to benefit from shape-matching or form-fitting materials.

Here, we demonstrate soft shape-matching metamaterials that are designed by rationally combining auxetic, conventional, and transitional unit cells into a cellular solid, and are indirectly additively manufactured from elastomers (Figure 1). We used an equal aspect ratio for the longitudinal and transversal dimensions of all unit cells for easier integration of the unit cells with different reference angles in a planar cellular structure. This enables us to combine auxetic and conventional unit cells in the longitudinal direction, which could be also replicated in the transverse direction. The arrangement of unit cells with different values of the Poisson's ratio could then be used to program the lateral deformation of the cellular material upon deformation. The inverse problem of rationally designing a shape-matching metamaterial then reduces to the problem of finding the combinations of the Poisson's ratios that give rise to the desired lateral deformation and mapping those values of the Poisson's ratios back to unit cell designs.

METHODS

To design the first prototypes, we divided the length of the specimen into three regions, i.e., auxetic, transitional, and conventional (Figure 1a). When designing the cellular structures, we assumed that the parameters c and w (Figure 1a) are constant

for both auxetic and conventional unit cells $^{c}/_{w} = 3$. The interior angle of each unit cell could therefore change the geometry of the unit cell from auxetic $48° < \theta < 90°$ to conventional $90° < \theta < 120°$. In the transitional region, the angle of each unit cell linearly changed from the auxetic angle to conventional one. We fabricated four prototypes with different unit cells in each of those three regions. The total numbers of unit cells in the longitudinal direction, $m = 18$, was similar for all specimens. The total length of each specimen was therefore $L = c \times m$. The number of unit cells in the transverse direction, n, was also fixed ($n = 7$). The width of each specimen was therefore $W = 2 \times n \times w$. The design parameters for all specimens are presented in Table 1.

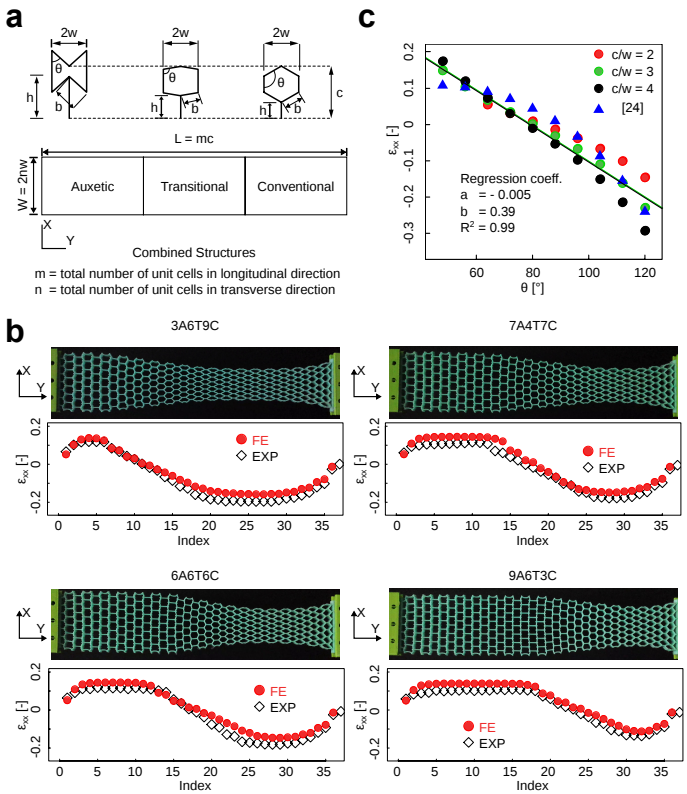

Figure 1

a) A schematic drawing of the auxetic and conventional unit cells. The angle, θ, varies between 48° and 120°. b) Four specimens with three zones (auxetic, transition and conventional) were fabricated. Computational models were developed for each specimen and the simulation results were compared against experimental observations. The specimen naming convention follows the NoANoTNoC format where "No" shows the number of unit cells in each region, while A, T, and, C stand for the number of unit cells in the auxetic, transitional, and conventional regions. In the transitional region, unit cells were linearly changed from auxetic to conventional unit cells. In all experimental specimens, c/w = 3. c) The strains of cellular structures calculated for different c/w ratios and reference angles (longitudinal strain = 20%). Numerical results were also compared with the analytical relation (Equation 2) in the literature [24] for the calculation of lateral strains.

Table 1
The parameters of the prototypes fabricated with indirect additive manufacturing.

parameters	$c\,[mm]$	$w[mm]$	$n[-]$	$m[-]$	$L[mm]$	$W[mm]$	$t_{lattice}$ $[mm]$	$t_{ligament}$ $[mm]$
	15	*5*	*7*	*18*	*270*	*70*	*7*	*0.7*

We used indirect additive manufacturing to fabricate the specimens. A mold was designed and additively manufactured using a fused deposition modeling (FDM) 3D printer (Ultimaker 2+, Geldermalsen, The Netherlands) from polylactic acid (PLA) filaments (MakerPoint PLA 750 gr Natural). Subsequently, an elastomeric polymer (Elite Double 8, Zhermack, Badia Polesine, Italy) with a one-to-one ratio of the base to catalyst was poured into the mold. Once the specimens had cured, i.e., after ≈1 hour, the mold was removed. The final shapes of all specimens are presented in Figure 1b.
The specimens were deformed under displacement-controlled tensile loading applied by a mechanical test bench (LLOYD instruments, LR5K, load cell = 100 N, displacement rate = 50 mm/min). Time, force, and displacement were recorded at a sampling rate of 20 Hz. Simultaneously, the deformation was captured by a digital camera. After the test, the first and last frames of each video was selected and converted into binary images. The middle junctions in each unit cell at the left and right sides of the structure were highlighted by points in the images. Then, the highlighted regions were dilated to one pixel. The initial width of specimens, W_j, was calculated from the first image as: $W_j = X_{j,right} - X_{j,left}$, where $j = 1{:}36$ shows the number of points in the total length of the structure and X_j stands for the position of each point measured in terms of pixels. Similarly, after deformation, the final width of each cross section, W_j', was calculated as $W_j' = X_{j,right}' - X_{j,left}'$. Finally, the lateral strain was defined as $\varepsilon_{j,xx} = \frac{W_j'}{W_j}$.
Computational models of the metamaterials were created with ABAQUS, 6.14. A hyperplastic Neo-Hookean material model $C_{10} = 0.106\ MPa$ and $D_1 = 0.03\ MPa^{-1}$ and plane-stress elements (CPS8) were used in the models. The material coefficients were determined using the standard experimental protocols for testing elastomeric materials in tension (ASTM D412 Type C) and compression (ASTM D 575-91). The out-of-plane thickness, $t_{lattice}$, of the structure and the thickness of each ligament, $t_{ligament}$ were respectively set to 10 mm and 1 mm. Two reference points were defined at the top and bottom of the model and were tied to two nodes from the corresponding locations. The bottom reference point was fixed while the top reference point was displaced far enough to create 20% longitudinal strain. An implicit

nonlinear solver (Abaqus Standard) was used for the simulations. The lateral strain calculated for the computational models were evaluated in a way similar to those of the experiments. Several node sets were defined at the internal hinges of the unit cells located at the left and right sides of the structure. The mean lateral displacements $U_{j,left}$, $U_{j,right}$ were calculated for each node set. The lateral strain was then obtained as: $\varepsilon_{j,xx} = \frac{U_{j,right} - U_{j,left}}{W}$.

The lateral strains obtained computationally were found to be in good agreement with experimental observations (Figure 1b). Having evaluated the accuracy of the computational models, we expanded them to include other $^{c}/_{W}$ ratios, i.e. 2, and 4, for fully auxetic and conventional lattice structures (Figure 1c). In those simulations, the total number of unit cells in the structure was kept the same to enable comparison with previous results and the lateral strain was calculated at the middle of the cellular structure. Our calculations showed changing this ratio does not drastically change the lateral strains especially for the auxetic unit cells (Figure 1c). Therefore, we continued to use $^{c}/_{W} = 3$ as a reference ratio in the following designs. Furthermore, the computational results showed an almost linear relationship between the lateral strains and the angle of the unit cells (Figure 1c). This linear relation was used as the basis of our designs in the next steps:

$$\varepsilon_{xx} = -0.005\theta + 0.39 \quad (1)$$

We compared our numerical simulations with the analytical relation found in the literature [24]. Lateral strain in the conventional and the re-entrant honeycombs can be calculated as:

$$\varepsilon_{xx} = -\frac{\delta sin\theta}{bcos\theta} \quad (2)$$

where, b and θ are the geometrical parameters of each unit cell (Figure 1a) and $\delta = \frac{0.2}{cos\theta}(c - h)$ as we fixed the applied longitudinal strain at 20%. The geometrical parameters, i.e. b, θ, c and h, were considered separately for individual unit cells and the fnal lateral strains were compared with the numerical simulations. Tis comparison shows a good agreement between the numerical and analytical results (Figure 1c).

We also performed experiments to evaluate the effects of the number of unit cells in the transverse direction of the structure on the lateral deformation (see the Supplementary information). We found that the number of the unit cells in the transverse direction only influences the amplitude of the deformations but not the lateral strains of the structure.

RESULTS AND DISCUSSION

Having verified our computational models against experiments for a number of designs, we developed a rational design platform based on the results of the

computational models to achieve lateral deformations that match the contour of an arbitrarily-shaped object. If the contour of the lateral deformation is discretized into a finite number of sub-regions, auxetic and conventional unit cells could be used to create the desired lateral deformation using Equation (1). The superposition of the deformations of all unit cells was hypothesized to create the target shape. To assess the validity of that hypothesis, we created a number of arbitrarily-defined strain functions Y1-Y9 using a three-terms Fourier's-like series:

$$Y = a_1 \sin\big(\alpha\omega(x-1)\big) + a_2 \sin\big(2\alpha\omega(x-1)\big) + a_3 \sin\big(3\alpha\omega(x-1)\big) \qquad (3)$$

where the parameters $\omega = 0.37$ and a_1, a_2, a_3, α (Table 2) were randomly selected. The x is the index of each unit cells in the longitudinal direction and changes between 1 and 18 (the total number of unit cells in the longitudinal direction of the cellular structure). Using Equation (1), we selected the angles of the auxetic and conventional unit cells such that their predicted deformation would follow the strain functions generated by Equation (3) using the above-mentioned coefficients (Figure 2). We then created computational models to determine the actual deformation of the cellular structures that were designed using the predictions of Equation (1). Comparison between the actual deformations and the target strain functions showed that the cellular structures designed using Equation (1) could closely follow the target shape in all considered cases (Figure 2).

Table 2
The random parameters used in the definition of the functions (Y1-Y9).

Functions	a_1	a_2	a_3	α
Y1	0.15	0	0	0.5
Y2	0	0.15	0	0.5
Y3	0	0	0.15	0.5
Y4	0.068	0.068	0.068	0.5
Y5	0.15	0	0.075	0.5
Y6	0.075	-0.09	0.045	0.5
Y7	0.068	0.068	0.068	1
Y8	0.105	-0.053	-0.053	1
Y9	0.15	0	0.075	1

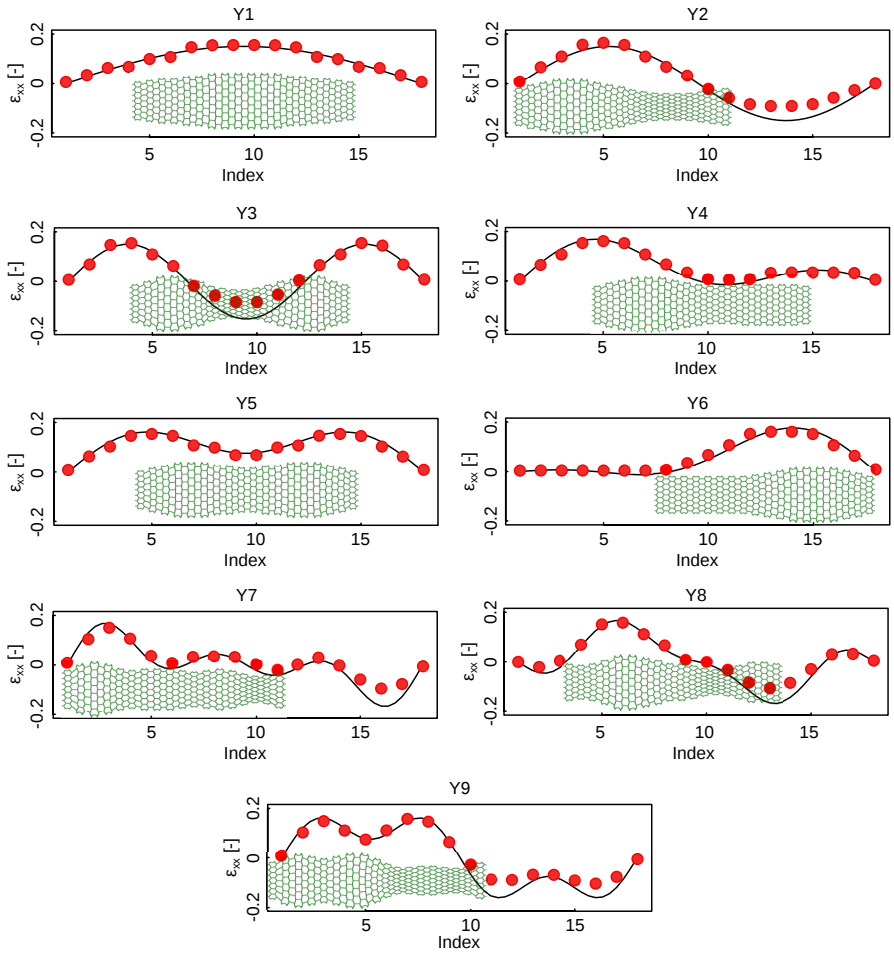

Figure 2
The structures were designed in a way to fit the arbitrary functions (Y1-Y9). The parameters of the functions are listed in Table 2. The longitudinal strain for each case is equal to 20% of the total length. The actual deformations determined using direct numerical simulations are also shown (scaling factor = 3).

In the last step, we aimed to design cellular structures that would match the shapes of three real objects including an anatomical model of the scapula (Sawbones, Vashon Island, USA), a pumpkin, and a piece of Delft Blue pottery (a vase) (Figure 3). All objects were photographed from the top view, which was then used to describe the contours of the objects. The resulting contours then served as the target shapes for the design of the cellular structures. We selected the reference angles of the auxetic and conventional unit cells such that, according to Equation (1), their lateral deformations match the captured contours as closely as possible. The total number of unit cells in

the transverse and longitudinal directions are therefore the only parameters that could be freely chosen with more unit cells along the length of the structure resulting in smoother approximations of the target curve. To use Equation (1), the design of the cellular structure needs to satisfy $^{c}/_{w} = 3$, which could be achieved by isotropic scaling of the entire structure. Assuming that we require a 20% deformation of the metamaterial to match the shape of the objects, the length of the cellular structures could be determined using a deformation ratio of 1.2. Given the total length of the specimen and the parameter c, the maximum number of unit cells along the length of the structure, m, was calculated. Having assumed the number of unit cells in the transverse direction, $n + 1$, the lateral strain could be calculated, which must be in the range of the minimum and maximum strains that fully auxetic and conventional structures could achieve. Finally, the reference angles of the unit cells were selected using Equation (1). A flowchart in Figure 3d shows the different design steps.

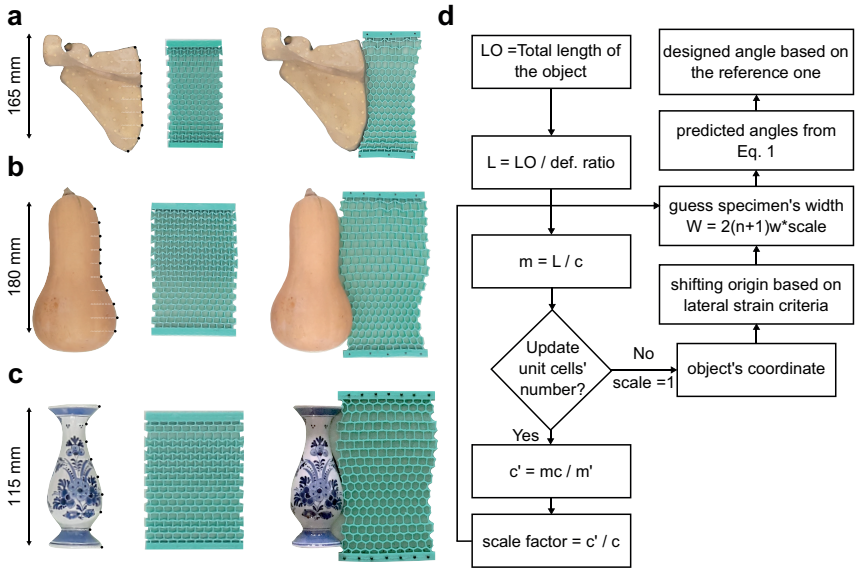

Figure 3
Matching the shapes of three real objects including an anatomical model of the scapula (a), a pumpkin (b), and a Delft Blue pottery piece (a vase) (c). d) The flowchart of the design procedure.

The cellular structures designed to match the shapes of the selected objects achieved reasonable approximations of their target contours (Figure 3a-c). The shapes of the objects used here were selected based on the potential applications of shape-matching metamaterials. Moreover, each object represented different types of shape variations. For instance, the contour of the pumpkin requires the highest deformation amplitude.

To achieve such high amplitudes, it is necessary to define more unit cells in the lateral direction of the structure (Figure 3b). The vase, on the other hand, has the smallest length among three objects. Therefore, application of a scaling factor is required when designing the shape-matching metamaterial (Figure 3c).

The fact that a simple equation such as Equation (1) and the superposition principle are very effective in designing soft metamaterials (whose deformation is nonlinear in nature) is quite remarkable and enables the fast design of shape-matching metamaterials without the need for (nonlinear) optimization algorithms. The presented technique could be expanded for the prediction of the deformations at lower (i.e., micro-) scales. While we used here mechanical loading to deform the specimens, shape-matching could also be activated using magnetic, thermal, or electrical stimuli. Shape memory polymers are the other candidates for such designs [25–28].

There are some limitations in the presented approach that are dictated by the maximum strains that could be achieved by conventional and auxetic unit cell. In general, auxetic unit cells tend to deform faster than the conventional ones and reach a level of saturation and robustness at higher longitudinal strains. This affects the connection between conventional and auxetic unit cells and prevents the conventional unit cells from complete deformation (see the Supplementary Information). The next steps would entail extending the presented technique to the case of three-dimensional shapes such as the shapes described by the surface of the human body.

In summary, we presented a design platform for the rational design of shape-matching soft mechanical metamaterials that combine functionally graded auxetic and conventional unit cells. The platform is shown to be able to match the arbitrary shapes created by three-term Fourier's series as well as the shape of real objects. Shape-matching materials have potential applications in soft robotics, wearable (medical) devices, and fashion industry.

References

[1] J. N. Grima and R. Caruana-Gauci, *Mechanical metamaterials: materials that push back*, Nat mater, **11**, 565 (2012).

[2] Z. G. Nicolaou and A. E. Motter, *Mechanical metamaterials with negative compressibility transitions*, Nat mater, **11**, 608 (2012).

[3] K. K. Saxena, R. Das, and E. P. Calius, *Three decades of auxetics research-materials with negative Poisson's ratio: a review*, Adv Eng Mater, **18**, 1847 (2016).

[4] A. A. Zadpoor, *Mechanical meta-materials*, Mater Horiz, **3**, 371 (2016).

[5] K. Bertoldi, P. M. Reis, S. Willshaw, and T. Mullin, *Negative Poisson's ratio behavior induced by an elastic instability*, Adv Mater, **22**, 361 (2010).

[6] R. Lakes, *Negative Poisson's Ratio Materials: Response*, Science, **238**, 551 (1987).

[7] Y. Prawoto, *Seeing auxetic materials from the mechanics point of view: a structural review on the negative Poisson's ratio*, Comp Mater Sci, **58**, 140 (2012).

[8] B. Florijn, C. Coulais, and M. van Hecke, *Programmable mechanical metamaterials*, Phys rev let, **113**, 175503 (2014).

[9] M. J. Mirzaali, R. Hedayati, P. Vena, L. Vergani, M. Strano, and A. A. Zadpoor, *Rational design of soft mechanical metamaterials: independent tailoring of elastic properties with randomness*, Appl Phys Let, **111**, 051903 (2017).

[10] A. Rafsanjani, A. Akbarzadeh, and D. Pasini, *Snapping mechanical metamaterials under tension*, Adv Mater, **27**, 5931 (2015).

[11] Y. Chen, T. Li, F. Scarpa, L. Wang, *Lattice Metamaterials with Mechanically Tunable Poisson's Ratio for Vibration Control*, Phys Rev Appl, **7**, 024012 (2017).

[12] T. Li, X. Hu, Y. Chen and L. Wang, *Harnessing out-of-plane deformation to design 3D architected lattice metamaterials with tunable Poisson's ratio*, Sci Rep **7**, 8949 (2017).

[13] R. M. Neville, F. Scarpa, and A. Pirrera, *Shape morphing Kirigami mechanical metamaterials*, Sci rep, **6**, 31067 (2016).

[14] Y. Cho, J.-H. Shin, A. Costa, T. A. Kim, V. Kunin, J. Li, S. Y. Lee, S. Yang, H. N. Han, I.-S. Choi, and others, *Engineering the shape and structure of materials by fractal cut*, Proc Natl Acad Sci U S A, **111**, 17390. (2014).

[15] R. M. Neville, J. Chen, X. Guo, F. Zhang, W. Wang, Y. Dobah, F. Scarpa, J. Leng, and H.-X. Peng, *A Kirigami shape memory polymer honeycomb concept for deployment*, Smart Mater Struct, **26**, 05LT03 (2017).

[16] J. Hu, Y. Zhou, Z. Liu, and T. Y. Ng, *Pattern Switching in Soft Cellular Structures and Hydrogel-Elastomer Composite Materials under Compression*, Polymers, **9**, 229 (2017).

[17] R. H. Baughman, *Auxetic materials: Avoiding the shrink*, Nature, **425**, 667 (2003).

[18] C. Laschi and M. Cianchetti, *Soft Robotics: New Perspectives for Robot Bodyware and Control*, Front Bioeng Biotechnol, **2**, 3 (2014).

[19] A. G. Mark, S. Palagi, T. Qiu, and P. Fischer, *Auxetic metamaterial simplifies soft robot design*, in Robotics and Automation (ICRA), 2016 IEEE International Conference on, 2016, p. 4951.

[20] L. N. Awad et al., *A soft robotic exosuit improves walking in patients after stroke*, Sci Transl Med, **9**, eaai9084 (2017).

[21] C. Coulais, E. Teomy, K. de Reus, Y. Shokef, and M. van Hecke, *Combinatorial design of textured mechanical metamaterials*, Nature, **535**, 529 (2016).

[22] B. Charlot, W. Sun, K. Yamashita, H. Fujita, and H. Toshiyoshi, *In-plane bistable nanowire for memory devices*, in Design, Test, Integration and Packaging of MEMS/MOEMS, 2008. MEMS/MOEMS 2008. Symposium on, 2008, p. 254.

[23] M. Konakovi, K. Crane, B. Deng, S. Bouaziz, D. Piker, and M. Pauly, *Beyond developable: computational design and fabrication with auxetic materials*, ACM Trans Graph, **35**, 89 (2016).

[24] L. J. Gibson, M. F. Ashby, *Cellular solids: structure and properties*. Cambridge university press (1999).

[25] M. Bianchi, F. Scarpa, and C. Smith, *Shape memory behaviour in auxetic foams: mechanical properties*, Acta Mater, **58**, 858 (2010).

[26] S. Janbaz, R. Hedayati, and A. A. Zadpoor, *Programming the shape-shifting of flat soft matter: from self-rolling/self-twisting materials to self-folding origami*, Mater Horiz, **6**, 536 (2016).

[27] T. van Manen, S. Janbaz, and A. A. Zadpoor, *Programming 2D/3D shape-shifting with hobbyist 3D printers*, Mater Horiz, **6**, 935 (2017).

[28] J. Rossiter, K. Takashima, F. Scarpa, P. Walters, and T. Mukai, *Shape memory polymer hexachiral auxetic structures with tunable stiffness*, Smart Mater Struct, **23**, 045007 (2014).

Supplementary information

Pure auxetic and conventional lattice structure were experimentally tested (Figure S1). Auxetic unit cells reached the saturation levels of strains earlier than conventional unit cells. The maximum level of lateral strain that could be reached with fully conventional structures is higher than the combined structures.

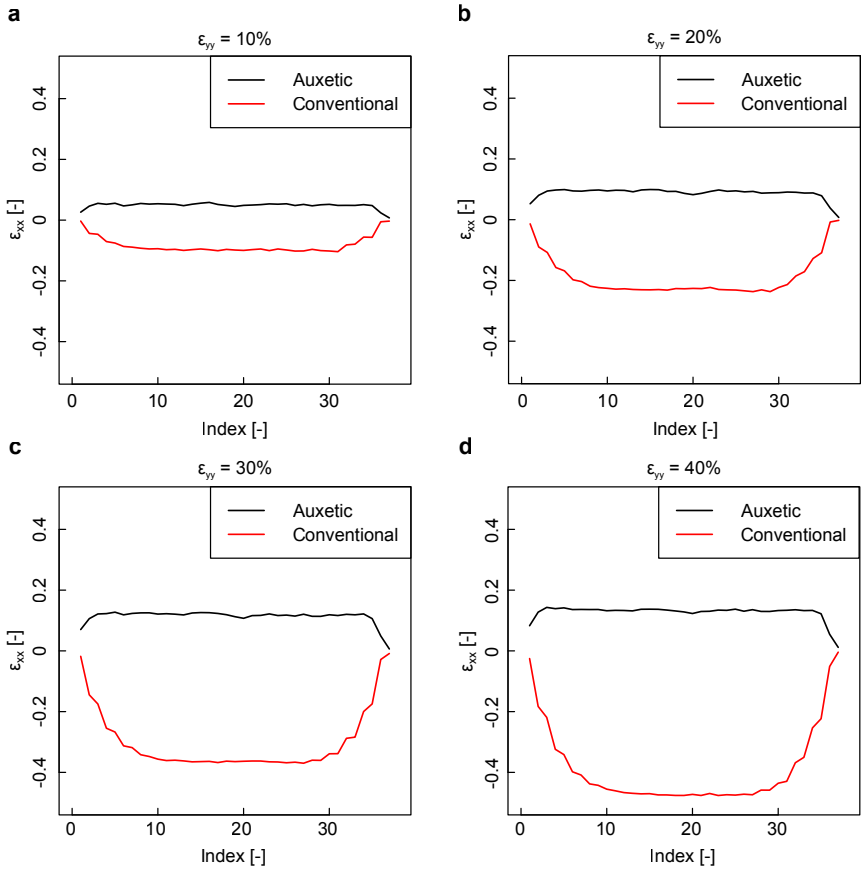

Figure S1
Lateral strain at four different longitudinal strains for pure auxetic and pure conventional lattice structures. The angle of auxetic and conventional structures were 48 and 120, respectively.

The total number of unit cells in the transverse direction does not influence the lateral strains. This is shown from the experiments Figure S2.

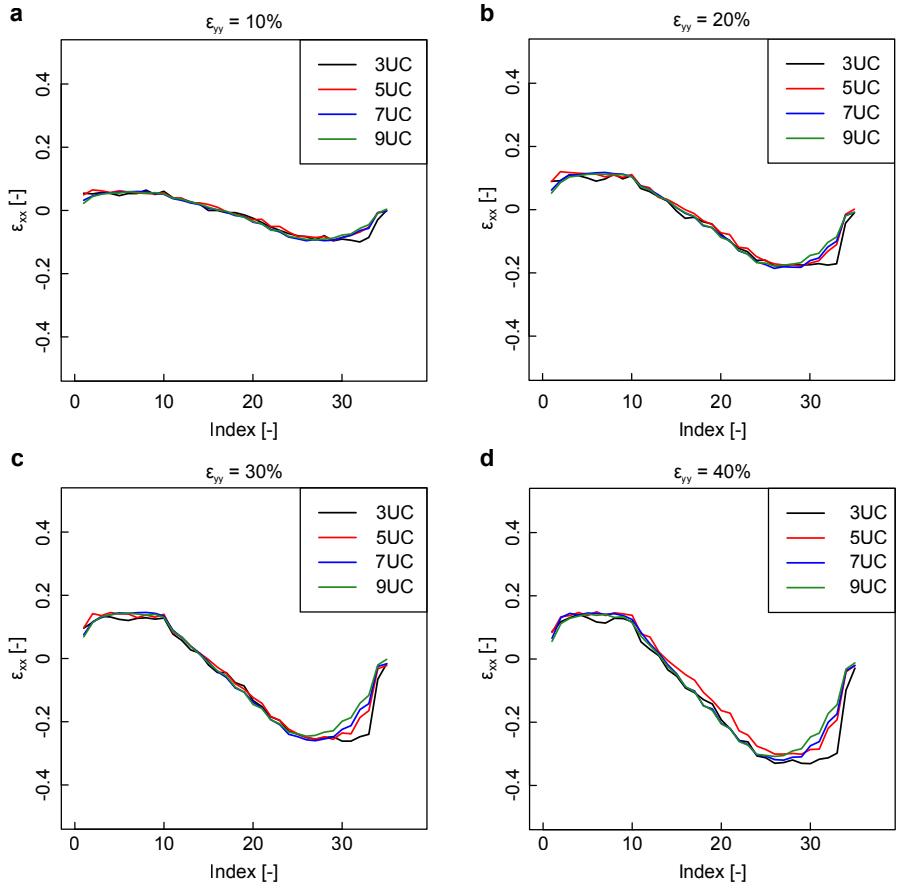

Figure S2
The effects of the number of unit cells in the transverse direction of combined structure on the lateral strains. Results are plotted at four extension levels (a-d). Equal number of conventional, auxetic and transitional unit cells were considered for the construction of these specimens.

Considering the experimental results for the combined structures, it was observed that changing the regions (auxetic, transition, conventional) in the structure does not influence the maximum lateral strains in the auxetic unit cells. However, due to the geometrical features of the conventional unit cells, they were more sensitive to the boundary conditions and deformation of the adjacent unit cells. In the transitional

region, we found that lateral strain linearly changes along the length (Figures S3 and S4).

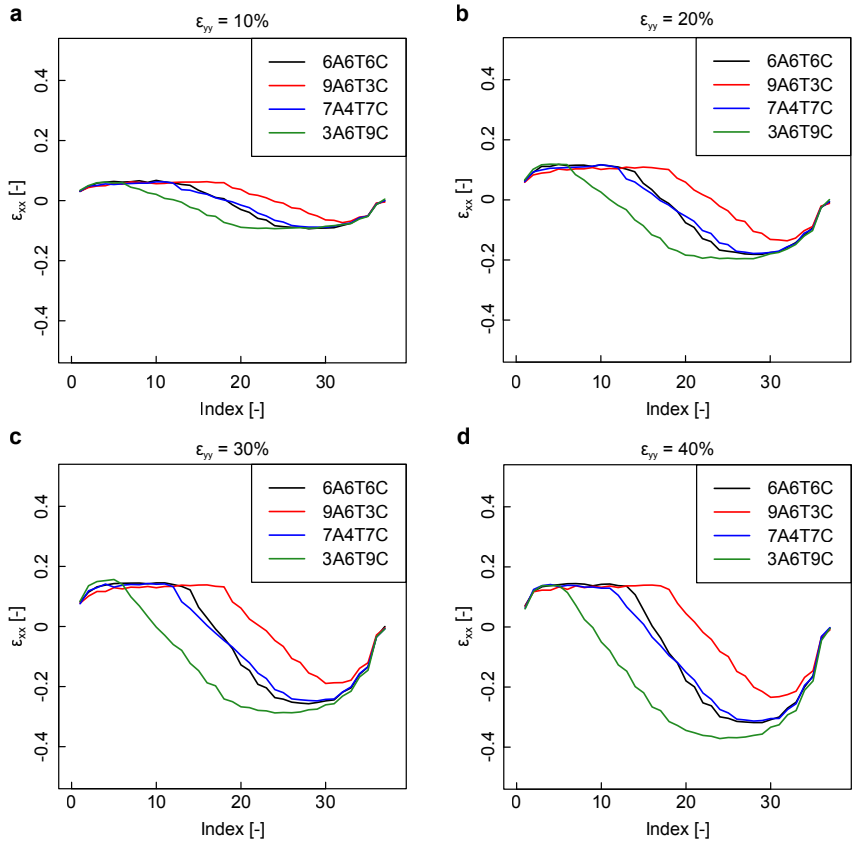

Figure S3
Comparison of lateral strains at different levels of longitudinal expansion for four combined specimens. The specimen naming convention follows the NoANoTNoC format where "No" shows the number of unit cells in each region, while A, T, and, C stand for the number of unit cells in the auxetic, transitional, and conventional regions. In the transitional region, unit cells were linearly changed from auxetic to conventional unit cells. In all experimental specimens, c/w=3.

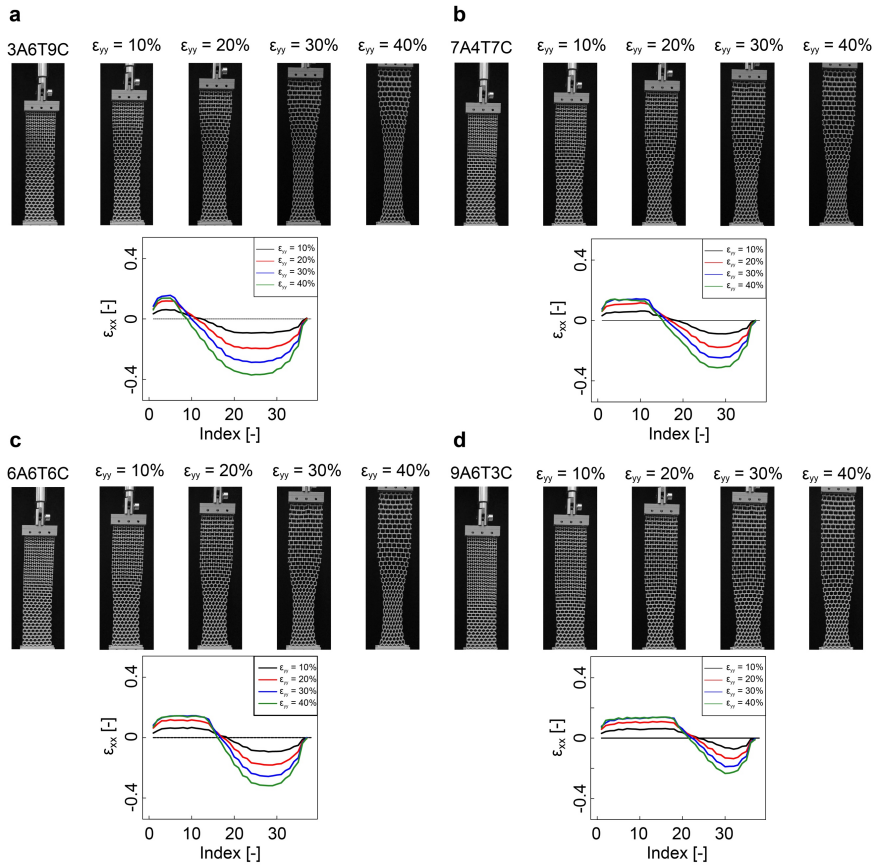

Figure S4
Individual lateral strains at different levels of longitudinal expansions for four combined specimens. a) 3A6T9C, b) 7A4T7C, c) 6A6T6C, d) 9A6T3C. The specimen naming convention follows the NoANoTNoC format where "No" shows the number of unit cells in each region, while A, T, and, C stand for the number of unit cells in the auxetic, transitional, and conventional regions. In the transitional region, unit cells were linearly changed from auxetic to conventional unit cells. In all experimental specimens, c/w=3.

Part B

From Flat Shapes to 3D Geometries

Chapter 6

Origami lattices with free-form surface ornaments

Science Advances (2017, 3, eaao1595)

Lattice structures are used in the design of metamaterials to achieve unusual physical, mechanical, or biological properties. The properties of such metamaterials result from the topology of the lattice structures, which are usually 3D printed. To incorporate advanced functionalities into metamaterials, the surface of the lattice structures may need to be ornamented with functionality-inducing features such as nano-patterns or electronic devices. Given our limited access to the internal surfaces of lattice structures, free-form ornamentation is currently impossible. Here we present lattice structures that are folded from initially flat states and show that they could bear arbitrarily complex surface ornaments at different scales. We identify three categories of space-filling polyhedra as the basic unit cells of the cellular structures and, for each of those, propose a folding pattern. We also demonstrate 'sequential self-folding' of flat constructs to 3D lattices. Furthermore, we folded auxetic mechanical metamaterials from flat sheets and measured the deformation-driven change in their negative Poisson's ratio. Finally, we show how free-form 3D ornaments could be applied on the surface of flat sheets with nanometer resolution. Taken together, these folding patterns and experimental techniques present a unique platform for fabrication of metamaterials with unprecedented combination of physical properties and surface-driven functionalities.

Rational design of the small-scale topology is the primary way of achieving unusual physical properties in many types of optical [1-3], electromagnetic[4], acoustic [5], and mechanical [6] metamaterials. Lattice structures have been often used in such topological designs to develop, among others, ultra-light yet ultra-stiff materials [7], fluid-like solids (meta-fluids) [8], materials with ultra-high energy absorption properties [9], auxetic materials [10], and materials that exhibit negative and adjustable thermal expansion [11]. The fact that the porosity and, thus, mass-transport properties (i.e. permeability and diffusivity) of lattice structures could be easily adjusted is instrumental to certain application areas such as regenerative medicine [12,13], where the nutrition and oxygenation of cells particularly at the early phases of tissue regenerations are dependent on diffusion. Modern 3D printing techniques have enabled production of lattice structures with arbitrarily complex topologies and with increasing accuracies at the micro- [14] and nano-scales [15-17]. Multi-functional metamaterials often require incorporation of functionality-inducing surface features onto the surface of lattice structures. For example, very specific types of nanotopographical features [18-21] applied on the surface of tissue engineering scaffolds [22] regulate focal adhesion [23] and activate certain mechanotransductory pathways [24] that determine the stem cell fate. Nanotopographical features on the surface of metamaterials could also induce other types of functionalities such as super-hydrophilicity and super-hydrophobicity [25-27], anti-reflective properties [28], and anti-bacterial behavior [29,30]. Devices such as (printed) sensors and actuators could be also integrated onto the surface of metamaterials to create metamaterials with more advanced functionalities. Advanced micro- and nano-patterning techniques such as electron-beam nanolithography [31], nano-imprinting [32,33], dip pen nanolithography [33,34], focused ion beam milling [35], and electron beam induced deposition [36], allow for free-form patterning of surfaces. However, they generally work only on flat surfaces. Moreover, our access to the internal surface areas of 3D printed lattice structures is very limited. Combining free-form surface ornaments with lattice topology is therefore currently impossible. Inspired by the Japanese art of paper folding (origami), here we present an approach that allows for that combination. The lattice structures are folded from initially flat states that allow for free-form ornamentation and device incorporation using currently available techniques. Self-folding mechanisms have been also incorporated into the flat material to allow for self-folding into the final lattice shape.

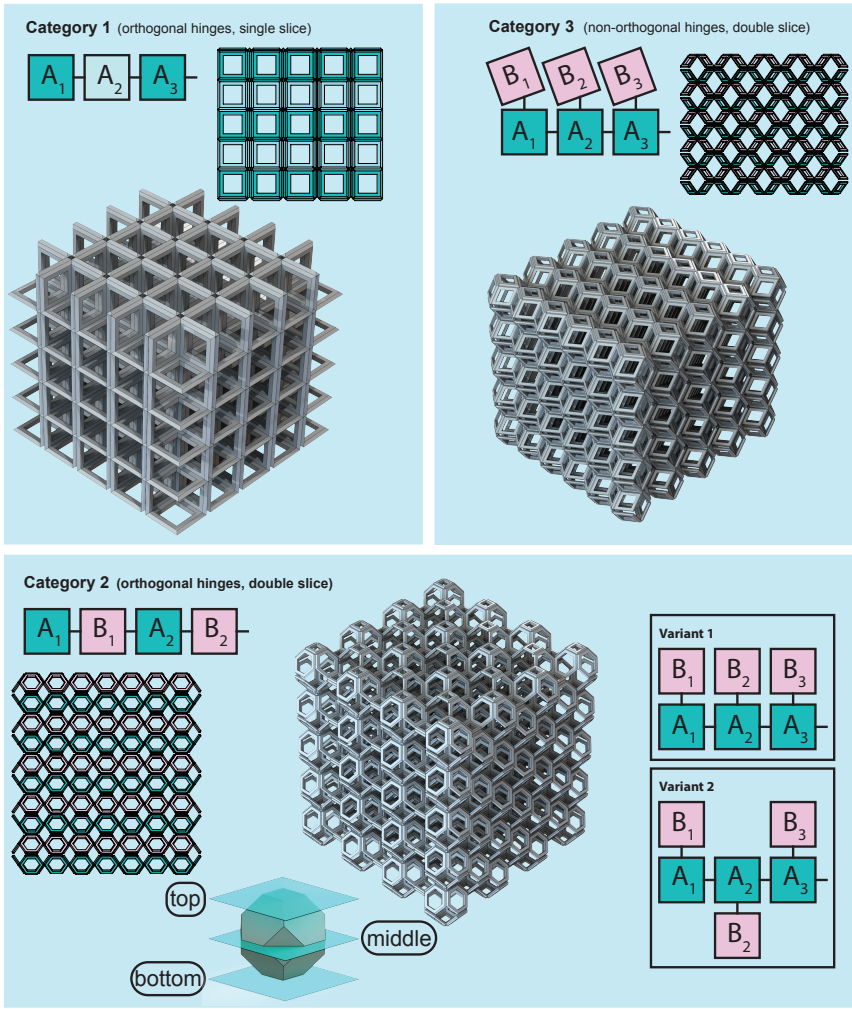

Figure 1
(Category 1) To unfold category 1 lattices, every floor needs to be sliced at its boundary with the adjacent floor. Within this context, a floor is a row of the lattice structure. The unfolded floors (A_1, A_2, …) are connected in series. A cubic lattice is illustrated here as an example of category 1 lattices. Dark and light green denote the same type of folding pattern. (Category 2) The lattices belonging to this category, need to be sliced at the middle of their floors as well as the boundary of the floors. The unfolded state of such lattices is made of a backbone that comprise every other half-floor (A_1, A_2, …) and the remaining half-floors (B_1, B_2, …) that branch out of the backbone. Green and pink colors therefore denote folding patterns that face each other after folding. Alternative arrangements of the half-floors are possible as shown in the two alternative variants. A truncated octahedron lattice is depicted here as an example of this category of foldable lattices. (Category 3) The unfolding of category 3 lattices is similar to that of category 2 lattices (a similar notation and color code is used), except that the positioning of the half-floors is not orthogonal anymore. A rhombic dodecahedron lattice is shown as an example of the foldable lattices from this category.

From computational geometry, the foldability of a large number of simple polyhedral structures from flat pieces of paper is guaranteed [37]. However, no such theorems exist for more complex polyhedral structures such as polyhedral lattices. Moreover, the algorithms used for establishing the generality results are not practical, as they are based on thin-paper assumptions and, thus, neglect the kinematic constraints that arise when folding real structures from sheets with finite thicknesses. In this work, we devised three folding patterns to fold various types of lattice structures from initially flat states (Figure 1). Those folding patterns account for and accommodate the thickness of the flat structure and are hence relevant for practical applications.

Folding Patterns

We considered lattices made by repeating a basic unit cell (with fixed shape and size) in different directions. Depending on the type of the repeating unit cell, a different folding pattern is needed. Unfolding the lattice to a fully flat state is the first step in devising the folding pattern. The lattice needs to be 'sliced' along certain cutting planes to allow for separation and unfolding. Each of the three folding patterns devised here have different folding kinematics (Figure 1 and S1-3). The proposed categories are aimed to serve as intuitive frameworks which guide the process of designing practical folding patterns for lattice structures of interest.

Category 1 includes the simplest types of unit cells with orthogonal fold lines (hinges), which generally require a single slice per lattice row (floor) (Category 1, Figure 1). The slicing planes are, thus, at the boundaries of the unit cells. Examples of space-filling polyhedra that belong in Category 1 are cubic, truncated cube, and oblique rectangular prism. A representative layer (floor) has open faces at the top and closed faces at the bottom (top, middle, and bottom are visualized in an inset of Figure 1). The thickness of the panels is incorporated by extruding the middle planes in both directions. The resulting panels are then chamfered at their edges to facilitate the folding process. In a thin-sheet design, the middle planes of the vertical faces would have overlapped with each other in the folded state. To accommodate the thickness in thick-sheet designs, the middle planes of the vertical faces were shifted by the thickness of one panel. Either a small connecting panel should then be positioned between two vertical panels or their thickness should be halved to allow for their folding (i.e. 180° relative rotation). The vertical panels at the end of each floor (i.e. mono-layer) connect the panels of different floors with each other. In their unfolded states, the unfolded floors (A_1, A_2, … in Figure 1) are connected to each other in series.

Category 2 covers more complex types of unit cells with orthogonal fold lines that require slicing along both top and bottom boundaries of the floors as well as through the middle of each floor (Figure 1). Since half-floors overlap at their boundaries, the middle planes need to be shifted by the thickness of one panel. In their unfolded (i.e. flat) state, the unfolded half-floors (A_1, A_2, … (green) and B_1, B_2, … (pink) in Figure

1) are connected to each other in series. Alternatively, the unfolded half-floors could be connected to each other in several other ways (see variants 1 and 2 of Category 2 in Figure 2). Some of those variants are helpful when trying to circumvent the additional kinematic constraints faced with more complex designs of unit cells and to accommodate locking mechanisms. Examples of space-filling polyhedra that could be unfolded using this type of folding pattern are truncated octahedron and re-entrant geometries.

Finally, Category 3 covers space-filling polyhedra with non-orthogonal folding lines (Figure 1). Those types of unit cells not only require double slicing similar to what described before for Category 2, but also need to be unfolded along non-orthogonal lines (Figure 1). Due to the complex spatial rotations that are required during the folding process, every other half-floor (B_1, B_2, … (pink) in Figure 1) should branch out of a main backbone (A_1, A_2, … (green) in Figure 1) that connects the remaining half-floors to each other in series (Figure 1, S3). Lattices based on a number of space-filling polyhedra such as rhombic dodecahedron could be folded using this type of folding pattern (Figure 2a). Supplementary videos 1-3 show the initially flat state, the folding sequences, and the resulting lattice structures for some sample unit cells from each category. Even though the three folding patterns presented here cover a large number of space-filling polyhedra, it is not clear how many of the hundreds of space-filling polyhedra [38] could be folded using the proposed patterns or slight modifications of those. On the other hand, a number of other (derivative) unit cell geometries could be folded using these patterns.

In the cases where the unfolded (half-)floors (i.e. A_1, A_2, …, B_1, B_2, …) are connected in series (i.e. Category 1 and the main variant of Category 2), one could first fold the (half-)floors individually and then fold the entire lattice. In the cases where there is a back-bone and half-floors that are branching out from that (i.e. Category 3 and two variants of Category 2), the facing half-floors, which make individual floors, should fold and meet each other first before all floors are folded to create the entire lattice. Sequential folding is therefore needed in those cases. Even when sequential folding is not essential to fold the lattice (e.g. Category 1), it could improve the reliability of the folding process by minimizing the chance of interlocking incidents. This is particularly important when locking mechanism are incorporated in the design of the lattice to increase its structural integrity.

Self- and sequential-folding

We also demonstrated the self-folding of lattice structures from initially flat states using 3D printed thick panels that hinged at the folding lines (Figure 2). We used simple elastic bands to program sequential folding into the flat assembly of panels. The number of elastic bands determined the amount of stored potential energy, which then converted to kinetic energy and determined the speed of the different segments

of the assembly during the folding process. That programmed sequential folding allowed for complete folding of the lattice structure from an initially flat state (see supplementary video 4). The designed cubic lattice also incorporated locking mechanisms that, subsequent to self-folding, locked the different segments of the panels into each other and guaranteed the mechanical performance of the folded lattice structure.

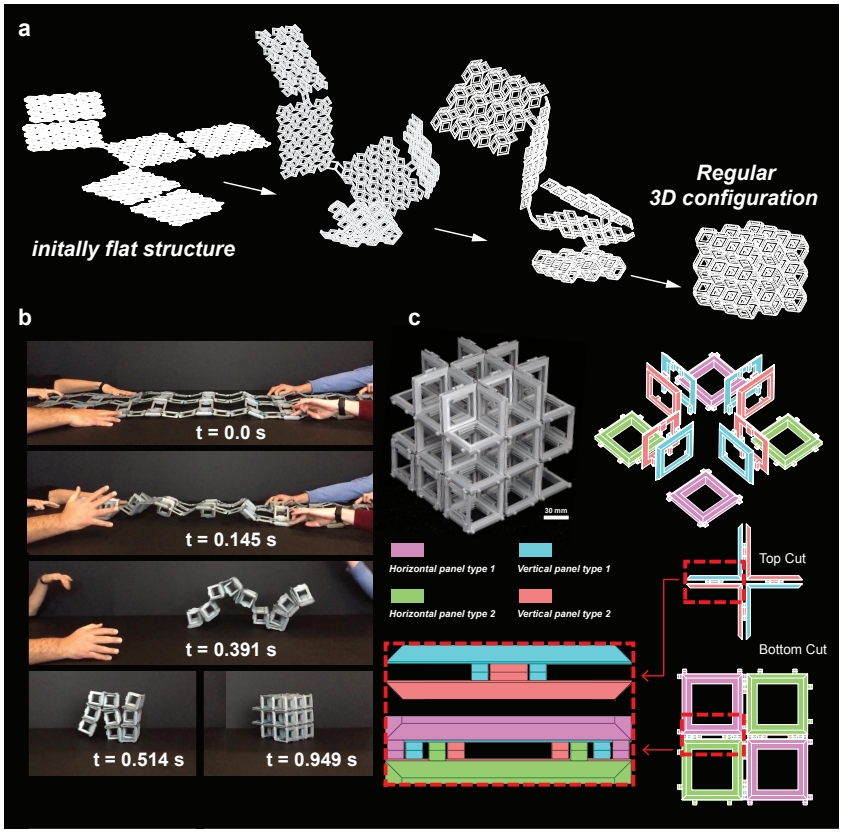

Figure 2
(a) The folding sequences for a category 3 lattice (rhombic dodecahedron). Folding sequences of all other sample lattices of Figure 1 can be seen in the supplementary videos 1-3. (b) The time sequence of sequential self-folding in a three-story thick panel lattice. 3D printed panels were hinged together using metal pins and a number of elastic rubber bands and, thus, the stored potential energy was used as a parameter for programming sequential self-folding. (c) The design of the self-folding lattice including the initial flat configuration and the final folded state. The hinges are designed so as to provide a confined space that locks the different floors after self-folding, thereby ensuring the integrity of the lattice and providing load-bearing capacity.

Mechanical metamaterials

The topology of the unit cells significantly influences the mechanical properties of lattice structures independent of their relative density (or porosity) [39]. Mechanical metamaterials with unusual properties could therefore be designed by changing the topology of the unit cells. Since adjusting the Poisson's ratio is one of the aims of such designs, here we present two types of fully-folded mechanical metamaterials with negative (reentrant unit cell) and zero (cubic unit cell) values of the Poisson's ratio (Figure 3). Locking mechanisms similar to what was shown before were incorporated in the design of the cubic lattice structure (Figure 3a) to ensure its ability to tolerate mechanical loading. The lattices were manually folded from aluminum sheets and subsequently tested under compression (Figure 3c-e). Both lattices showed significant mechanical properties (Figure 3c-d). The Poisson's ratio of the auxetic lattice structure (based on the ensemble average of selected reentrant unit cells on the front side of the reentrant lattice) was determined using image processing techniques and was found to significantly change with the applied axial deformation (Figure 3e). The cubic lattice failed in a layer-by-layer fashion largely preserving its near-zero Poisson's ratio, while the final shape of the reentrant-based lattice structure clearly showed the auxetic behavior of this mechanical metamaterial.

Free-form surface ornamentation

To demonstrate the extent of freedom offered by the proposed approach in terms of surface ornamentation, we used two distinct techniques to decorate the surfaces of origami lattices at both micro- and nano-scales (Figure 4). The first technique, i.e. electron beam induced deposition (EBID), could be considered a 3D printing technique with a theoretical resolution in the 'sub-nanometer' range [40]. We used EBID (see supplementary document for the methodological details) not only to create nano-patterns and write on the surface of flat origami sheets but also to create free-form 3D shapes and lattice structures with features sizes in the range of a few tens of nanometers (Figure 4a). Combining the surface ornaments demonstrated here with the lattice folding patterns, it is possible to create hierarchical lattice structures that also cover the internal surfaces of porous lattices. The second patterning technique, namely ultrashort pulse laser micromachining, was used to apply patterns at the micrometer scale (Figure 4b). For both techniques, the type, geometry, and size of the ornaments could be very different from one place within the flat sheet to another. Functionally graded ornaments, i.e. ornaments with spatially varying topology and dimensions, could then be realized. For example, we packed multiple types of surface patterns into the same origami lattice (Figure 4b).

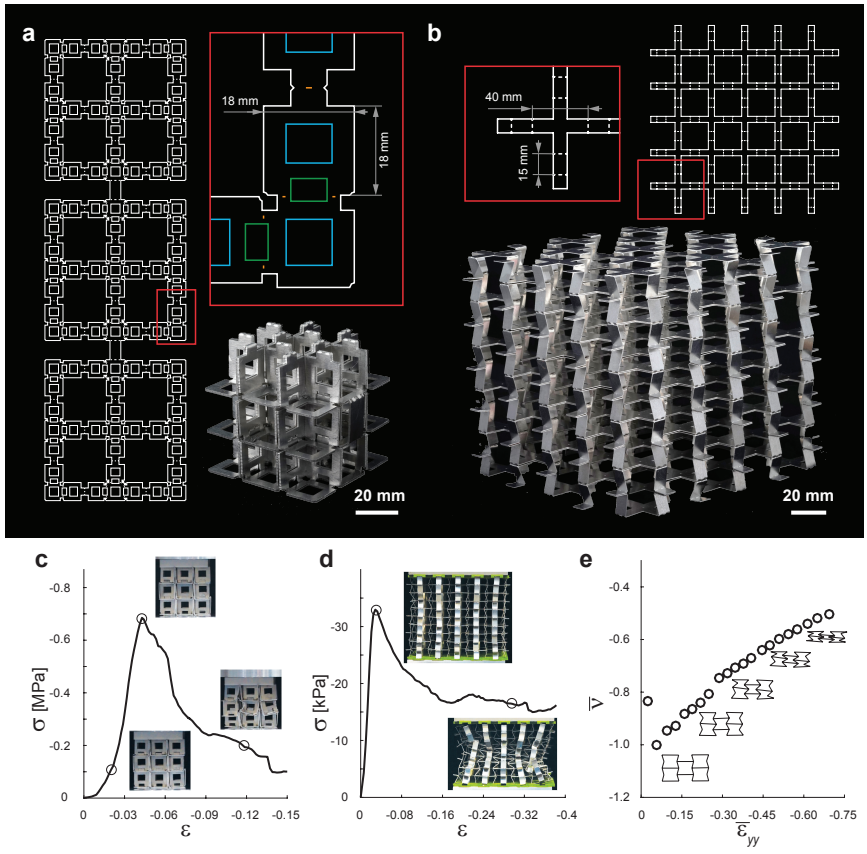

Figure 3
Conventional and auxetic metallic origami lattices. (a) An aluminum cubic lattice structure comprising 3 unit cells in each direction. (b) Multi-layer assembly of a re-entrant lattice structure (a variant of truncated octahedron). (c, d) Compression stress-strain results for cubic and reentrant structures. (e) The evolution of the average Poisson's ratio with compressive strain in the auxetic lattice. The evolution in the shape of the unit cells belonging to the ensemble that was used for calculating the Poisson's ratio is depicted as well.

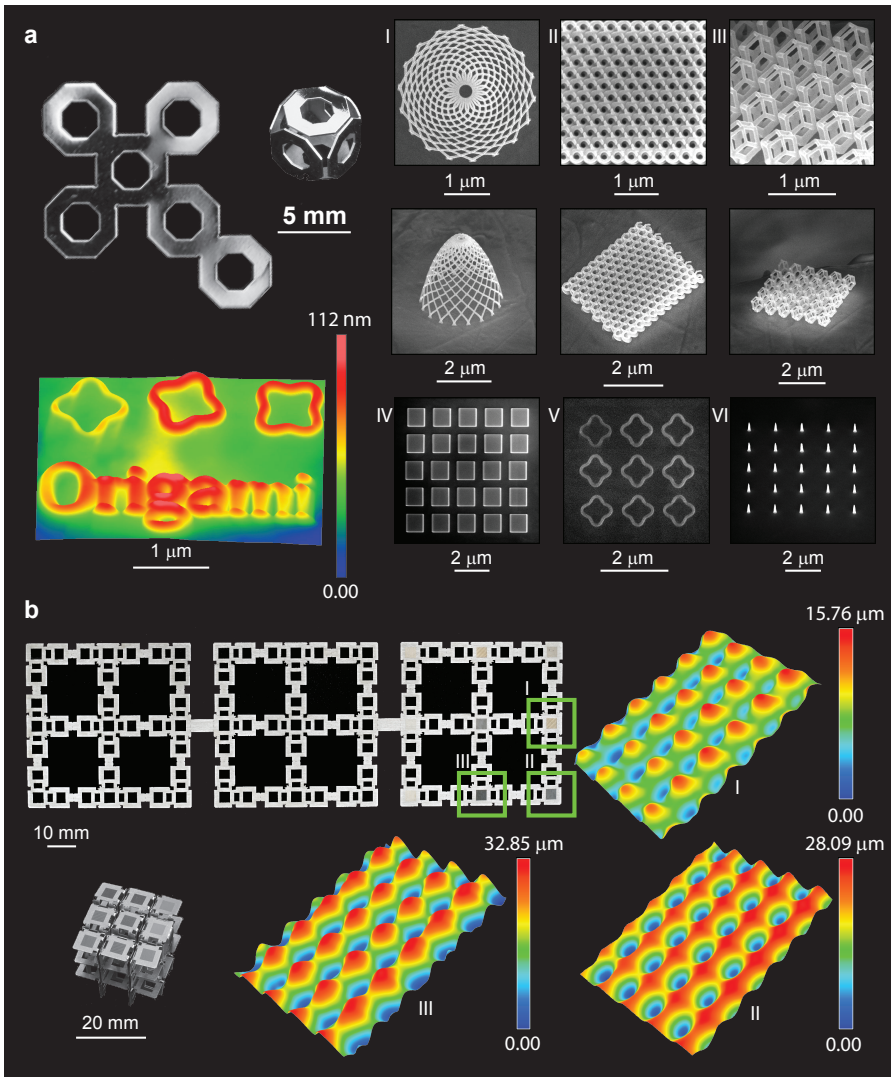

Figure 4
Free-form ornamentation of origami lattices. (a) Electron beam-induced deposition was used to deposit gasified platinum based precursor on top of a polished flat origami truncated octahedron cut from a 200 µm pure titanium foil. Multiple 2D and hierarchical 3D patterns have been produced with features sizes in the range of a few tens of nanometers. The surface ornaments were imaged using SEM. The dimensions of the ornaments were measured with AFM (details in the supplementary document). (b) A flat pure titanium foil was patterned using an ultrashort pulse laser. Three spots in the unfolded sheet were patterned using three different types of pattern design. The final configuration of folded lattice shows the arrangement of the three patterned spots. The profiles of the patterns were measured using 3D optical microscopy (details in the supplementary document).

Potential and applications

There are several areas where the proposed approach could be used for creating metamaterials with advanced functionalities. One specific area is the development of (meta-)biomaterials that stimulate tissue regeneration. Recent studies have shown that very specific nano-topographies could determine stem cell fate and induce cell differentiation towards the preferred lineage [18,24,41]. Advanced surface ornamentation techniques such as those presented here are capable of producing the required nano-topographies but only on flat surfaces. At the same time, highly ordered porous lattice structures with fully interconnected porosities are needed to simultaneously provide mechanical support for tissue regeneration and facilitate the transport of oxygen and nutrients to cells [42,43]. The approach proposed here allows for combining the bio-functionalities offered by surface ornaments with those provided by highly ordered lattice structures and will be pursued in our future research. Another example of the potential areas of application would be integration of flexible electronics (e.g. sensors and actuators) in the design of (mechanical) metamaterials.

Conclusions

The approach presented here for fabrication of lattice structures with internal surfaces that are covered with arbitrarily complex ornaments is unprecedented, general, and scalable. Different variants of this approach with alternative folding patterns, self-folding techniques, and surface ornamentation methods could be used to suit the needs of various application areas. Using other surface ornamentation techniques such as optical and electron-beam lithography as well as combining the current techniques with techniques such as nano-imprinting could maximize the scalability of the ornamentation techniques.

Materials and methods

The polymeric models of (self-folding) lattice structures (Figure 2 and S4) were fabricated with a 3D printer (Ultimaker 2+, Ultimaker, The Netherlands) working on the basis of fused deposition modelling (FDM) and using polylactic acid filaments (diameter = 2.85 mm, Ultimaker). Pre-stretched elastic bands were used as active elements. Sequential folding was achieved by adjusting the number of the pre-stretched elastic bands.

The metallic lattices (Figure 3) were folded from an aluminum sheet (1050A with a nominal elastic modulus of 71 GPa) and a thickness of 0.8 mm, which was laser cut to create the unfolded state of a cubic structure comprising 3 unit cells in each direction (see Figure 3 and S5 for details). In order to fixate the top and bottom floors during mechanical testing, a poly-methyl methacrylate (PMMA) plate (thickness = 8 mm) was laser cut to create matching grooves that accommodated the free ends of the

lattice structure. The same type of sheet (thickness = 0.5 mm) was laser cut and folded to form the different floors of the re-entrant lattice (Figure 3), which were later mounted on top of each other to create the full lattice structure. Clamps with matching grooves were 3D printed using an Ultimaker 2+ printer (Ultimaker, The Netherlands) and polylactic acid filaments (diameter = 2.85 mm, Ultimaker). The folded floors (together with their clamps, Figure S5) were placed under 2 kg of compressive load for 15 mins to minimize the springback of the folds. The floors were then assembled using double-sided tapes (Tesa, sided polyester tape type FT 4967) and were put under compressive pre-load similar to what was explained for the folded floors. The folded lattices were then compressed uniaxially using a Lloyd LR5K mechanical testing machine equipped with a 5 kN load cell. A high resolution digital camera (Sony A7R with a Sony FE 90 mm f/2.8 macro OSS lens) was used to record the trend of the deformations. A group of unit cells (5 full unit cells and 2 halves) in the middle of the front side of the re-entrant lattice were selected to estimate the evolution in the Poisson's ratio as the compressive strain increased.

To create the nanopattern using the electron beam induced deposition technique (Figure 4a), a truncated cube origami unit cell was laser cut first and manually polished using 3 μm and 1 μm water-based diamond suspensions for 30 mins. The final polish was performed with the OP-S solution and an automatic polisher (Struers, RotoPol-31 & RotoForce-4) for 20 minutes giving a roughness of 5 ± 3 nm based on four selected squares of 1.5 by 1.5 μm. Prior to patterning, the samples were cleaned ultrasonically in acetone for 5 minutes, soaked in isopropanol, and then dried with compressed nitrogen gas and in the oven at 90 °C. By using trimethyl(methylcyclopentadienyl)-platinum (IV) precursor ($MeCpPtMe_3$) in a Nova Nano Lab 650 Dual Beam system (FEI, Oregon), various shapes, from simple arrays of squares and pillars to complex 3D shapes were generated at different locations within the polished surface of the titanium unit cell.

For laser patterning (Figure 4b), a smaller version of the cubic lattice used for mechanical testing was laser cut from a pure titanium foil (thickness = 0.125 mm, purity: 99.6+%, annealed, GoodFellow). Nine different surface patterns were created in nine different spots of the top floor of the cubic lattice using laser micro-machining (machine: 3D Micromac, PicoBlade® laser, wavelength = 355 nm, scanner: 163 mm, Lumentum, performed by Reith Laser, the Netherlands). The samples were then carefully washed and dried. A digital optical microscope (Keyence, VHX-5000) was used to produce the 3D images of resulting patterns by merging multiple images taken at varying depths of focus (Figure 4b).

Following EBID, the generated surface ornaments were directly inspected with SEM and images were acquired at various magnifications both under horizontal and tilted positions. Selected structures were also imaged with atomic force microscopy (AFM) using a Fastscan-A probe (Bruker, Massachusetts) with a tip radius of 5 nm and

nominal spring constants of 18 N/m. Experiments were conducted under ambient conditions. ScanAsyst® mode was implemented with a scan rate of 3.91 Hz. ScanAsyst® (Bruker, Massachusetts) is a tapping-based mode with automatic image optimization. The results obtained from AFM were then analyzed using Gwyddion 2.47.

References

[1] J. Valentine, S. Zhang, T. Zentgraf, E. Ulin-Avila, D. A. Genov, G. Bartal, and X. Zhang, *Three-dimensional optical metamaterial with a negative refractive index*, Nature **455**, 376 (2008).

[2] V. M. Shalaev, *Optical negative-index metamaterials*, Nat Photon **1**, 41 (2007).

[3] I. M. Pryce, K. Aydin, Y. A. Kelaita, R. M. Briggs, and H. A. Atwater, *Highly strained compliant optical metamaterials with large frequency tunability*, Nano Lett **10**, 4222 (2010).

[4] D. Schurig, J. J. Mock, B. J. Justice, S. A. Cummer, J. B. Pendry, A. F. Starr, and D. R. Smith, *Metamaterial electromagnetic cloak at microwave frequencies*, Science **314**, 977 (2006).

[5] S. Zhang, C. Xia, and N. Fang, *Broadband acoustic cloak for ultrasound waves*, Phys Rev Lett **106**, 024301 (2011).

[6] A. A. Zadpoor, *Mechanical meta-materials*, Mater Horiz **3**, 371 (2016).

[7] X. Zheng *et al.*, *Ultralight, ultrastiff mechanical metamaterials*, Science **344**, 1373 (2014).

[8] M. Kadic, T. Bückmann, N. Stenger, M. Thiel, and M. Wegener, *On the practicability of pentamode mechanical metamaterials*, Appl Phys Lett **100**, 191901 (2012).

[9] J. H. Lee, L. Wang, M. C. Boyce, and E. L. Thomas, *Periodic bicontinuous composites for high specific energy absorption*, Nano Lett **12**, 4392 (2012).

[10] K. E. Evans and A. Alderson, *Auxetic materials: Functional materials and structures from lateral thinking!*, Adv Mater **12**, 617 (2000).

[11] Q. Wang, J. A. Jackson, Q. Ge, J. B. Hopkins, C. M. Spadaccini, and N. X. Fang, *Lightweight Mechanical Metamaterials with Tunable Negative Thermal Expansion*, Phys Rev Lett **117**, 175901 (2016).

[12] Y. Chen, S. Zhou, and Q. Li, *Microstructure design of biodegradable scaffold and its effect on tissue regeneration*, Biomaterials **32**, 5003 (2011).

[13] X. Sun, Y. Kang, J. Bao, Y. Zhang, Y. Yang, and X. Zhou, *Modeling vascularized bone regeneration within a porous biodegradable CaP scaffold loaded with growth factors*, Biomaterials **34**, 4971 (2013).

[14] M. Vaezi, H. Seitz, and S. F. Yang, *A review on 3D micro-additive manufacturing technologies*, Int J Adv Manuf Tech **67**, 1721 (2013).

[15] M. Lee and H. Y. Kim, *Toward nanoscale three-dimensional printing: nanowalls built of electrospun nanofibers*, Langmuir **30**, 1210 (2014).

[16] M. Rohrig, M. Thiel, M. Worgull, and H. Holscher, *3D direct laser writing of nano- and microstructured hierarchical gecko-mimicking surfaces*, Small **8**, 3009 (2012).

[17] J. Bauer, A. Schroer, R. Schwaiger, and O. Kraft, *Approaching theoretical strength in glassy carbon nanolattices*, Nat Mater **15**, 438 (2016).

[18] M. J. Dalby, N. Gadegaard, R. Tare, A. Andar, M. O. Riehle, P. Herzyk, C. D. Wilkinson, and R. O. Oreffo, *The control of human mesenchymal cell differentiation using nanoscale symmetry and disorder*, Nat Mater **6**, 997 (2007).

[19] J. Fu, Y. K. Wang, M. T. Yang, R. A. Desai, X. Yu, Z. Liu, and C. S. Chen, *Mechanical regulation of cell function with geometrically modulated elastomeric substrates*, Nat Methods **7**, 733 (2010).
[20] H. N. Kim, A. Jiao, N. S. Hwang, M. S. Kim, D. H. Kang, D. H. Kim, and K. Y. Suh, *Nanotopography-guided tissue engineering and regenerative medicine*, Adv Drug Deliv Rev **65**, 536 (2013).
[21] J. Shi, A. R. Votruba, O. C. Farokhzad, and R. Langer, *Nanotechnology in drug delivery and tissue engineering: from discovery to applications*, Nano Lett **10**, 3223 (2010).
[22] M. M. Stevens, *Biomaterials for bone tissue engineering*, Mater Today **11**, 18 (2008).
[23] E. K. Yim, E. M. Darling, K. Kulangara, F. Guilak, and K. W. Leong, *Nanotopography-induced changes in focal adhesions, cytoskeletal organization, and mechanical properties of human mesenchymal stem cells*, Biomaterials **31**, 1299 (2010).
[24] M. J. Dalby, N. Gadegaard, and R. O. Oreffo, *Harnessing nanotopography and integrin-matrix interactions to influence stem cell fate*, Nat Mater **13**, 558 (2014).
[25] T. Sun, L. Feng, X. Gao, and L. Jiang, *Bioinspired surfaces with special wettability*, Acc Chem Res **38**, 644 (2005).
[26] T. L. Liu and C. J. Kim, *Repellent surfaces. Turning a surface superrepellent even to completely wetting liquids*, Science **346**, 1096 (2014).
[27] E. Martines, K. Seunarine, H. Morgan, N. Gadegaard, C. D. Wilkinson, and M. O. Riehle, *Superhydrophobicity and superhydrophilicity of regular nanopatterns*, Nano Lett **5**, 2097 (2005).
[28] A. Rahman, A. Ashraf, H. Xin, X. Tong, P. Sutter, M. D. Eisaman, and C. T. Black, *Sub-50-nm self-assembled nanotextures for enhanced broadband antireflection in silicon solar cells*, Nat Commun **6**, 5963 (2015).
[29] L. Zhao, S. Mei, P. K. Chu, Y. Zhang, and Z. Wu, *The influence of hierarchical hybrid micro/nano-textured titanium surface with titania nanotubes on osteoblast functions*, Biomaterials **31**, 5072 (2010).
[30] S. Kim, U. T. Jung, S. K. Kim, J. H. Lee, H. S. Choi, C. S. Kim, and M. Y. Jeong, *Nanostructured multifunctional surface with antireflective and antimicrobial characteristics*, ACS Appl Mater Interfaces **7**, 326 (2015).
[31] S. Kim, B. Marelli, M. A. Brenckle, A. N. Mitropoulos, E. S. Gil, K. Tsioris, H. Tao, D. L. Kaplan, and F. G. Omenetto, *All-water-based electron-beam lithography using silk as a resist*, Nat Nanotechnol **9**, 306 (2014).
[32] H. Schift, *Nanoimprint lithography: An old story in modern times? A review*, J Vac Sci Technol, B **26**, 458 (2008).
[33] Z. Nie and E. Kumacheva, *Patterning surfaces with functional polymers*, Nat Mater **7**, 277 (2008).
[34] S. W. Lee, B. K. Oh, R. G. Sanedrin, K. Salaita, T. Fujigaya, and C. A. Mirkin, *Biologically active protein nanoarrays generated using parallel dip-pen nanolithography*, Adv Mater **18**, 1133 (2006).
[35] R. Steve and P. Robert, *A review of focused ion beam applications in microsystem technology*, J Micromech Microeng **11**, 287 (2001).

[36] W. F. van Dorp and C. W. Hagen, *A critical literature review of focused electron beam induced deposition*, J Appl Phys **104**, 081301 (2008).
[37] E. D. Demaine, M. L. Demaine, and J. S. B. Mitchell, *Folding flat silhouettes and wrapping polyhedral packages: New results in computational origami*, Comp Geom-Theor Appl **16**, 3 (2000).
[38] D. G. Wells, *The Penguin Dictionary of Curious and Interesting Geometry* (Penguin Books, 1991).
[39] A. A. Zadpoor and R. Hedayati, *Analytical relationships for prediction of the mechanical properties of additively manufactured porous biomaterials*, J Biomed Mater Res A **104**, 3164 (2016).
[40] W. F. van Dorp, B. van Someren, C. W. Hagen, P. Kruit, and P. A. Crozier, *Approaching the resolution limit of nanometer-scale electron beam-induced deposition*, Nano Lett **5**, 1303 (2005).
[41] S. Dobbenga, L. E. Fratila-Apachitei, and A. A. Zadpoor, *Nanopattern-induced osteogenic differentiation of stem cells - A systematic review*, Acta Biomater **46**, 3 (2016).
[42] S. J. Hollister, *Porous scaffold design for tissue engineering*, Nat Mater **4**, 518 (2005).
[43] F. S. L. Bobbert and A. A. Zadpoor, *Effects of bone substitute architecture and surface properties on cell response, angiogenesis, and structure of new bone*, J Mater Chem B **5**, 6175 (2017).
[44] I. Utke and H. W. P. Koops, *The historical development of electron beam induced deposition and etching: from carbon to functional materials*, In I. Utke, S. Moshkalev, & P. Russel (Eds.), Nanofabrication using focused ion and electron beams: principles and applications (pp. 3-35). New York: Oxford University Press. (2012).
[45] A. Fernandez-Pacheco, L. Serrano-Ramon, J. M. Michalik, M. R. Ibarra, J. M. De Teresa, L. O'Brien, D. Petit, J. Lee, and R. P. Cowburn, *Three dimensional magnetic nanowires grown by focused electron-beam induced deposition*, Sci Rep **3**, 1492 (2013).
[46] J. M. D. Teresa, A. Fernández-Pacheco, R. Córdoba, L. Serrano-Ramón, S. Sangiao, and M. R. Ibarra, *Review of magnetic nanostructures grown by focused electron beam induced deposition (FEBID)*, J Phys D: Appl Phys **49**, 243003 (2016).
[47] P. Peinado, S. Sangiao, and J. M. De Teresa, *Focused Electron and Ion Beam Induced Deposition on Flexible and Transparent Polycarbonate Substrates*, ACS Nano **9**, 6139 (2015).
[48] C. Shi *et al.*, *Recent advances in nanorobotic manipulation inside scanning electron microscopes*, Microsystems & Nanoengineering **2**, 16024 (2016).
[49] J. D. Beard and S. N. Gordeev, *Fabrication and buckling dynamics of nanoneedle AFM probes*, Nanotechnology **22**, 175303 (2011).
[50] A. P. Ivanov, E. Instuli, C. M. McGilvery, G. Baldwin, D. W. McComb, T. Albrecht, and J. B. Edel, *DNA tunneling detector embedded in a nanopore*, Nano Lett **11**, 279 (2011).

[51] P. C. Post, A. Mohammadi-Gheidari, C. W. Hagen, and P. Kruit, *Parallel electron-beam-induced deposition using a multi-beam scanning electron microscope*, Journal of Vacuum Science & Technology B **29**, 06F310 (2011).
[52] M. Scotuzzi, M. J. Kamerbeek, A. Goodyear, M. Cooke, and C. W. Hagen, *Pattern transfer into silicon using sub-10 nm masks made by electron beam-induced deposition*, J Micro Nanolithogr MEMS MOEMS **14**, 031206 (2015).
[53] A. V. Riazanova, B. N. Costanzi, A. I. Aristov, Y. G. Rikers, J. J. Mulders, A. V. Kabashin, E. D. Dahlberg, and L. M. Belova, *Gas-assisted electron-beam-induced nanopatterning of high-quality titanium oxide*, Nanotechnology **27**, 115304 (2016).
[54] C. W. Hagen, *The future of focused electron beam-induced processing*, Appl Phys a-Mater **117**, 1599 (2014).

Supplementary information

Design and folding sequence

The designs and folding strategies of some sample lattices from the three identified categories are illustrated in the three following figures.

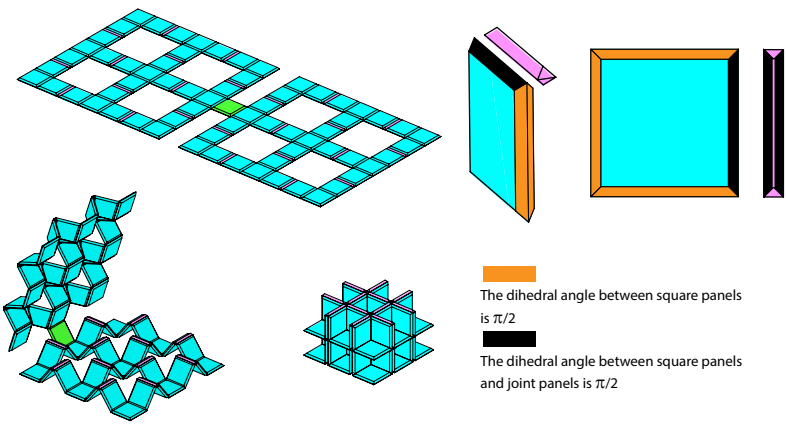

Figure S1
A Category 1 lattice made from the cubic unit cell. Each floor includes a repetitive pattern of square panels (cyan) and joint panels (pink) that connect vertical panels. Joint panels have a short edge length equal to the thickness of the panels so as to accommodate the thickness of the vertical panels. Some additional (bridge) panels (green) are needed to connect different floors in series. The folding direction of each floor is opposite to those of the neighbouring floors. Two overlapping vertical panels provide a larger thickness, which enhances the stability of the adjacent floor. The dihedral angle between all panels is $\pi/2$.

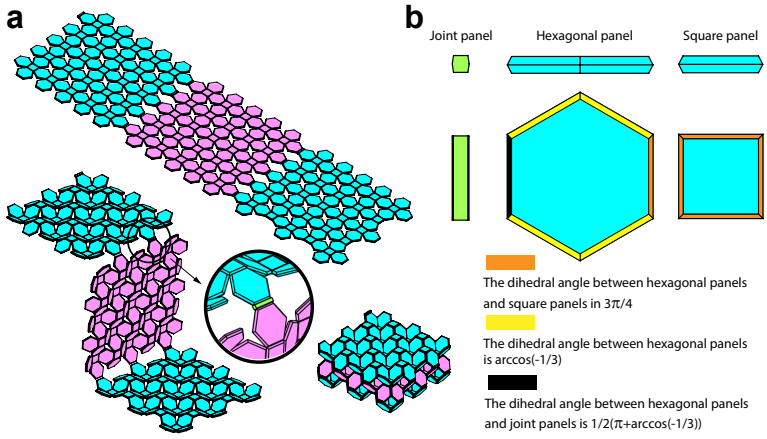

Figure S2
The serial connection of three half-floors in a truncated octahedron lattice (Category 2). Two neighbouring half-floors (highlighted in cyan and pink) form a floor. Joint panels (green) connect adjacent half-floors. The folding directions are similar in neighbouring half-floors. The dihedral angle between hexagonal panels and square panels is $3\pi/4$.

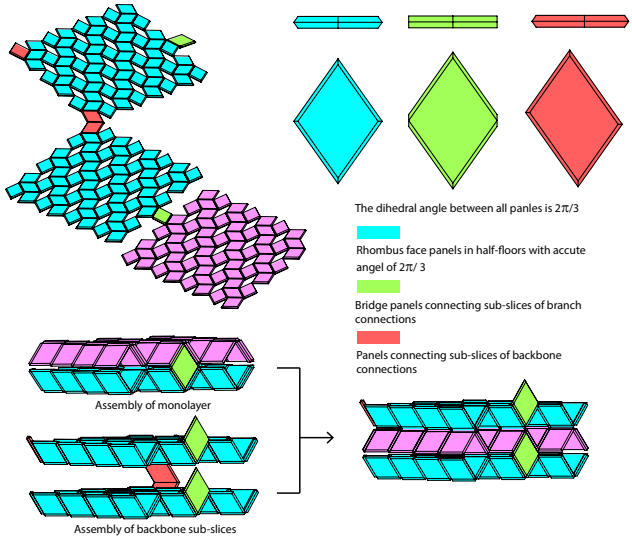

Figure S3
A Category 3 lattice made from the rhombic dodecahedron unit cell. Every other half-floor is a part of the backbone (cyan), while the remaining half-floors (magenta) branch out of the backbone. All the panels in a half-floor have similar rhombus faces with acute angles of $arccos(1/3)$, thereby forming non-orthogonal chains. A number of bridge panels (green) connect different half-floors. The diagonal extension of the joint panels equals the thickness of the main lattice panels. The dihedral angle between all panels is $2\pi/3$.

Self-folding lattices

A number of square-shaped panels were connected to each other using revolute joints and according to a variant of the design previously described for Category 1 lattices (Figure S4). Two different arrangement of hinges were introduced for connection of vertical and horizontal panels. To provide a locking mechanism, the hinges were designed in such a way that the hinges of the top floor be positioned in a confined space between the panels of the bottom floor (Figure S4). All panels were fabricated with a 3D printer (Ultimaker 2+, Ultimaker, The Netherlands) working on the basis of fused deposition modelling (FDM) and using polylactic acid filaments (diameter = 2.85 mm, Ultimaker). Pre-stretched elastic bands were used as active elements. Sequential folding was achieved by adjusting the number of the pre-stretched elastic bands. The resulting sequential self-folding happened in about 1 s (see supplementary video 4).

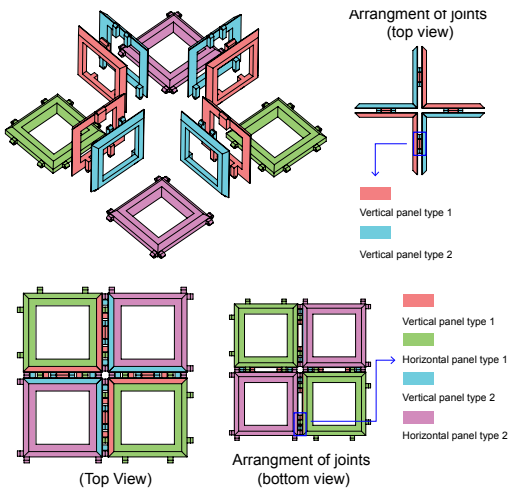

Figure S4
Arrangement of joints in hinged panels. The gaps introduced between any two parallel panels provide a confined space for locking the lattice structure in its folded state.

Folded mechanical metamaterials

The dihedral angles could be chosen so as to adjust the mechanical properties of the folded lattice structures. We folded two types of lattice-based mechanical metamaterials and adjusted their Poisson's ratios through modification of the dihedral angles. The first case is a lattice structure of cubic unit cells with a Poisson's ratio of zero. An aluminum sheet (1050A with a nominal elastic modulus of 71 GPa) and a thickness of 0.8 mm was laser cut to create the unfolded state of a cubic structure comprising 3 unit cells in each direction (see Figure 3 and S5 for details). In order to

fixate the top and bottom floors during mechanical testing, a poly-methyl methacrylate (PMMA) plate (thickness = 8 mm) was laser cut to create matching grooves that accommodated the free ends of the lattice structure.

A second lattice structure based on the re-entrant unit cell was designed by increasing the angle between the inclined panels. It is worth noting that the re-entrant unit cell is a variant of the truncated octahedron lattice where the expanded square has been replaced by a cross-like shape while the hexagonal design in the truncated octahedron structure has been transformed into a rectangular piece (Figure S5b). The dihedral angle between inclined panels was increased until the convex shape of polyhedrons turned into concave (re-entrant shape). The nominal dihedral angle, neglecting the effect of sheet thickness, was 83.34°. Aluminium sheets (1050A, thickness = 0.5 mm, nominal elastic modulus = 71 GPa) were laser cut and folded to form the different floors of the re-entrant lattice, which were later mounted on top of each other to create the full lattice structure. Clamps with matching grooves were 3D printed using an Ultimaker 2+ printer (Ultimaker, The Netherlands) and polylactic acid filaments (diameter = 2.85 mm, Ultimaker). The folded floors were placed under 2 kg of compressive load for 15 mins to minimize the springback of the folds. The floors were then assembled using double-sided tapes (Tesa, sided polyester tape type FT 4967) and were put under compressive pre-load similar to what was explained for the folded floors.

The folded lattices were then compressed uniaxially using a Lloyd LR5K mechanical testing machine equipped with a 5 kN load cell. A high resolution digital camera (Sony A7R with a Sony FE 90 mm f/2.8 macro OSS lens) was used to record the trend of the deformations. Figure 3a,b shows the engineering stress-strain curves of the cubic and re-entrant lattice structures where the engineering stress is the force divided by the initial cross-section area of the lattice structures. A group of unit cells (5 full unit cells and 2 halves) at the centre of the front side of the re-entrant lattice were selected to estimate the evolution in the Poisson's ratio as the compressive strain increased (Figure S6). A Matlab (Mathworks, US) code was developed to process the recorded images, calculate the lateral and horizontal displacements of the equivalent vertices, and determine the ensemble average of the horizontal and vertical strains ($\overline{\varepsilon}_{xx}$, $\overline{\varepsilon}_{yy}$) as:

$$\overline{\varepsilon}_{xx} = \frac{\sum_{j=1}^{5} x^{(3,j)} - x^{(1,j)} + x^{(4,j)} - x^{(2,j)} - A_0}{A_0} \qquad (1)$$

$$A_0 = \sum_{j=1}^{5} x_0^{(3,j)} - x_0^{(1,j)} + x_0^{(4,j)} - x_0^{(2,j)},$$

$$\bar{\varepsilon}_{yy} = \frac{\sum_{i=1}^{4} y^{(i,5)} - y^{(i,1)} + y^{(i,4)} - y^{(i,2)} - B_0}{B_0} \qquad (2)$$

$$B_0 = \sum_{i=1}^{4} y_0^{(i,5)} - y_0^{(i,1)} + y_0^{(i,4)} - y_0^{(i,2)}$$

The mean average $\pm$ standard deviation for the dihedral angle between the horizontal and inclined faces was estimated to be $74.59 \pm 1.26°$ in the uncompressed state of the assembled lattice. The deviation from the nominal value is due to the effect of the sheet thickness. Figure 3d shows the change in the Poisson's ratio, $\bar{\upsilon}$, as the compressive strain, $\bar{\varepsilon}_{yy}$, increases.

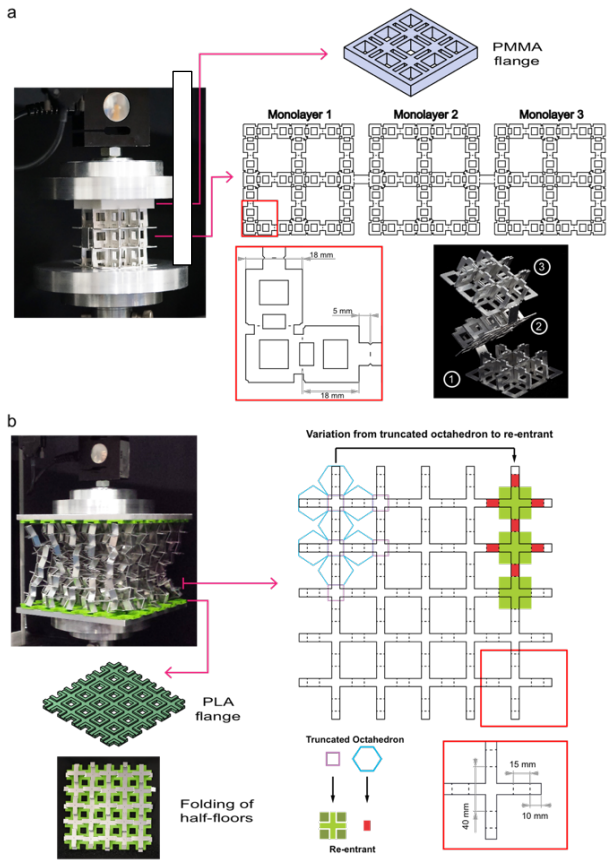

Figure S5
Fully-folded cubic and re-entrant lattices. (a) A three-floor cubic lattice and the PMMA clamp used for fixing the cubic lattice during mechanical testing. (b) The re-entrant lattice and the 3D printed flanges made for its fixation during mechanical testing.

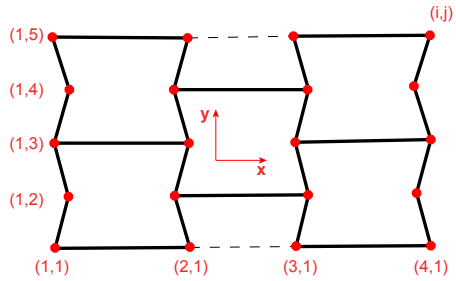

Figure S6
The initial configuration of the ensemble determined from the recorded images using the developed Matlab code.

Free-form surface ornamentation

The initial flat state of origami lattices provides full access to the surface of the material. It is therefore possible to apply free-form surface ornaments that induce advanced functionalities using highly refined ornamentation technologies that work only on flat surfaces. Here, we created surface ornaments at the scale of a few micrometres (with laser micro-machining) as well as a few nanometres (with electron beam induced deposition, EBID). Laser micro-machining is basically a subtractive manufacturing process, while EBID is one of the finest 3D printing technique currently available with a theoretical resolution in the single-nanometer range. A cubic origami lattice and one truncated cube origami unit cell were laser cut from a pure titanium foil as the host substrate for surface ornaments.

Laser

A smaller version of the cubic lattice used for mechanical testing was laser cut from a pure titanium foil (thickness = 0.125 mm, purity: 99.6+%, annealed, GoodFellow). Nine different surface patterns were created in nine different spots of the top floor of the cubic lattice using laser micro-machining (machine: 3D Micromac, PicoBlade® laser, wavelength = 355 nm, scanner: 163 mm, Lumentum, performed by Reith Laser, the Netherlands). The samples were then carefully washed and dried. A digital optical microscope (Keyence, VHX-5000) was used to produce the 3D images of resulting patterns by merging multiple images taken at varying depths of focus (Figure 4b).

Electron beam induced deposition

From an undesired side-effect during scanning electron microscopy, EBID has evolved into an advanced lithography method to generate controlled structures at nanoscale [44]. The need for such structures spans many fields of applications including magnetic nanostructures for 3D memory devices and catalytic growth

[45,46], flexible electronics, nano-optics and nanoplasmonics [47], nanotools/nanodevices [48], and biosensors for medicine [49,50]. The method is based on direct writing (i.e. no resist layers and templates are needed) on the surface of interest by local growth of deposits as a result of interactions between the precursor gas molecules adsorbed on the surface and a focused beam of electrons (Figure S7). The process enables generation of patterns with high spatial resolution (i.e. features size down to 1 nm) as well as *in situ* imaging of the resulting structures in a single-step process[36,40]. Nanopatterning and 3D nanofabrication of free-forms are possible on planar as well as non-planar conductive substrates. Using different precursor gases, variations in deposit chemistries and functionalities (e.g. magnetic, insulators, semiconductors) could be achieved. The growth rates of the deposits depend on the total electron flux available for dissociation, the supply of precursor gas, and the residence time of gas molecules on the substrate.

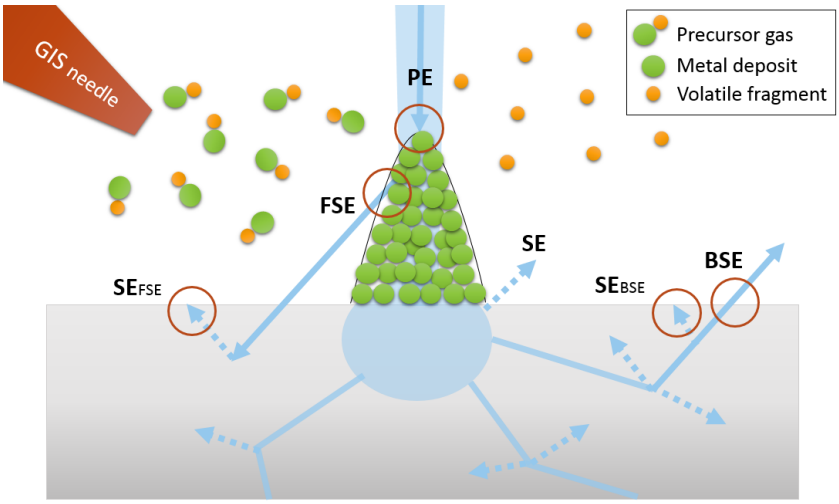

Figure S7
A schematic drawing of the EBID process: the precursor gas molecules injected by the gas injection system (GIS) are adsorbed on the surface and are converted under the electron beam irradiation (primary electrons) into non-volatile fragments that form the solid deposits and volatile components that leave the system. (SE=secondary electrons; BSE=backscattered electrons; FSE=forward scattered electrons).

The potential of the EBID process to generate hierarchical 3D structures is clearly shown by direct patterning the initially planar unit cells that undergo subsequent assembly by controlled mechanisms. A truncated cube origami unit cell was laser cut first and then manually polished using 3 μm and 1 μm water-based diamond

suspension for 30 mins. The final polish was performed with the OP-S solution and an automatic polisher (Struers, RotoPol-31 & RotoForce-4) for 20 minutes giving a roughness of 5 ± 3 nm based on four selected squares of 1.5 by 1.5 μm. Prior to EBID processing, the samples were cleaned ultrasonically in acetone for 5 minutes, soaked in isopropanol, and then dried with compressed nitrogen gas and in the oven at 90 °C. By using trimethyl(methylcyclopentadienyl)-platinum (IV) precursor ($MeCpPtMe_3$) in a Nova Nano Lab 650 Dual Beam system (FEI, Oregon) (Figure S8), various shapes, from simple arrays of squares and pillars to complex 3D shapes were generated at different locations within the polished surface of the titanium unit cell.

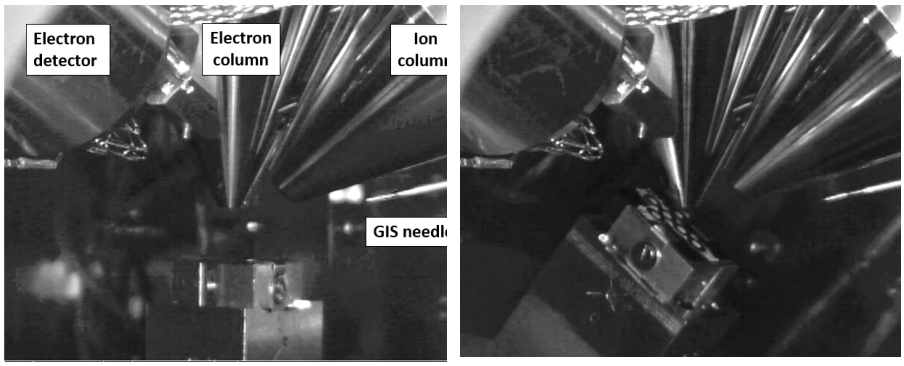

Figure S8
Titanium sample (unit cell) mounted on the holder inside the EBID microscope chamber: (a) horizontal position; (b) tilted position used to image the resulting ornaments.

The growth parameters used for each pattern/shape are presented in Table S1. The structures have been generated either by using the graphical user interface (GUI) or by creating stream files. For the latter, the unit cells were drawn in Portable Network Graphics format (.png). Using Matlab routines, the coordinates of all pixels were acquired and generated into a stream file. In order to produce 1 nm dots for each pixel, a magnification of 31,250x was used.

The 3D arrays were built from the ground up, in a parallel writing mode; each substructure (spiral or rhombic dodecahedra) was built up out of a set of irradiated pixels and the corresponding pixels of each substructure in the array was irradiated successively, building up the entire array in the z-direction. The spacing between the irradiated pixels in each substructure was approximately 1 nm. The pillar/spiral diameter ranged between 100 nm near the surface to about 30 nm at the top of the arrays. All structures were written with a 5,0 kV acceleration voltage and a current of 98 pA at a chamber-pressure between $1{,}0{\cdot}10^{-5}/2{,}0{\cdot}10^{-5}$ milli-bar. Following EBID, the generated surface ornaments were directly inspected with SEM and images were

acquired at various magnifications both under horizontal and tilted positions. Selected structures were also imaged with atomic force microscopy (AFM) using a Fastscan-A probe (Bruker, Massachusetts) with a tip radius of 5 nm and nominal spring constants of 18 N/m. Experiments were conducted under ambient conditions. ScanAsyst® mode was implemented with a scan rate of 3.91 Hz. ScanAsyst® (Bruker, Massachusetts) is a tapping-based mode with automatic image optimization. The results obtained from AFM were then analyzed using Gwyddion 2.47. Representative SEM and AFM images of the structures are presented in Figures S9 and S10.

Table S1
EBID process conditions

Pattern/Shape	Acc. voltage	Dwell time	Current	GIS position/gas pressure	Remarks
Patterns					
Square arrays	20 kV	1.0 µs	2.4 nA	Inserted (50 µm above the sample)/ $7x10^{-6}$ mbar	GUI
Triangle arrays	20 kV	1.0 µs	2.4 nA	Inserted/ $7x10^{-6}$ mbar	GUI
Circle arrays	20 kV	1.0 µs	2.4 nA	Inserted/ $7x10^{-6}$ mbar	GUI
Pillar arrays	20 kV	1.0 µs	2.4 nA	Inserted/ $7x10^{-6}$ mbar	GUI
4-Fold ring	20 kV	100 µs	2.4 nA	Retracted	.str file
Filled 4-fold shapes	20 kV	100 µs	2.4 nA	Retracted	.str file
Origami	20 kV	100 µs	2.4 nA	Retracted	.str file
3D shapes					
Double helices array	5 kV	6.0-8.0 ms/pixel	98 pA	$1.0x10^{-5}$-$2.0x10^{-5}$ mbar	.str file
Spiral mesh cylinders	5 kV	8.0-20.0 ms/pixel	98 pA	$1.0x10^{-5}$-$2.0x10^{-5}$ mbar	.str file
Stacked pyramids	5 kV	4 ms/pixel plus 0.8 ms/successive layer	98 pA	$1.0x10^{-5}$-$2.0x10^{-5}$ mbar	.str file
Rhombic dodecahedron array	5 kV	8 ms/pixel	98 pA	$1.0x10^{-5}$-$2.0x10^{-5}$ mbar	.str file
Spiral cone shape	5 kV	4.6-11 ms/pixel	98 pA	$1.0x10^{-5}$-$2.0x10^{-5}$ mbar	.str file

GIS = gas injection system; GUI = graphical user interface; .str file = stream files

Table S2
Characteristic dimensions of the EBID structures, as determined from AFM, SEM and stream files.

Pattern/Shape	Characteristic size (nm)	Height (nm)	Interspace
Patterns			
Square	1024 ± 16 x 1070 ± 19	120 ± 9	1487 ± 14
Circle	1054 ± 17	114 ± 6	1495± 9
Triangle (isosceles)	A: 519 ± 11 h: 529 ± 16 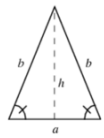	89 ± 3	1481 ± 9
Pillar	255 ± 16	507 ± 12	1493 ± 9
4-Fold ring	Line width: 163 ± 3		
Filled 4-fold shapes	634 ± 6 x 63 ± 5	59 ± 3	694 ± 13
3D shapes (pillar/spiral diameter changes from about 100 nm at the base to 30 nm at the top of the arrays)			
Double helices array	Helix radius: 120 nm	900 nm	50 nm
Spiral mesh cylinders	Helix radius: 200 nm 4 clockwise and 4 counterclockwise	-	-
Stacked pyramids	Area covered by a pyramid: 400 x 400 nm	1000 nm	-
Rhombic dodecahedron array	Area covered by rhombic dodecahedron area coverage: 600 x 600 nm	-	30 nm
Spiral Cone shape	2 sets of oppositely oriented spirals Outer radius: 1500 nm Inner radius 150 nm	-	-

Structures with sizes between 30 nm and 1100 nm, with a high aspect ratio or complex self-supporting 3D shapes were generated by designing specific stream files and optimizing the growth conditions (Figure S9). Furthermore, it was remarkable to observe that such structures could be also deposited on non-planar local areas of the samples.

The combination of the proposed origami lattices and EBID-made surface ornaments opens up exciting opportunities for biomedical applications (and beyond) by enabling unprecedented combinations of biofunctionalities, ranging from biomechanical to biomolecular stimuli in a single hierarchical construct. As an example, recent studies indicate the potential of specific nanoscale patterns as a sole stimulus for controlling the fate of stem cells[18,24,41]. By combining such nanopatterns with rationally-

designed 3D architectures, instructive constructs for regenerative medicine could be developed with unparalleled biocompatibility for various applications.

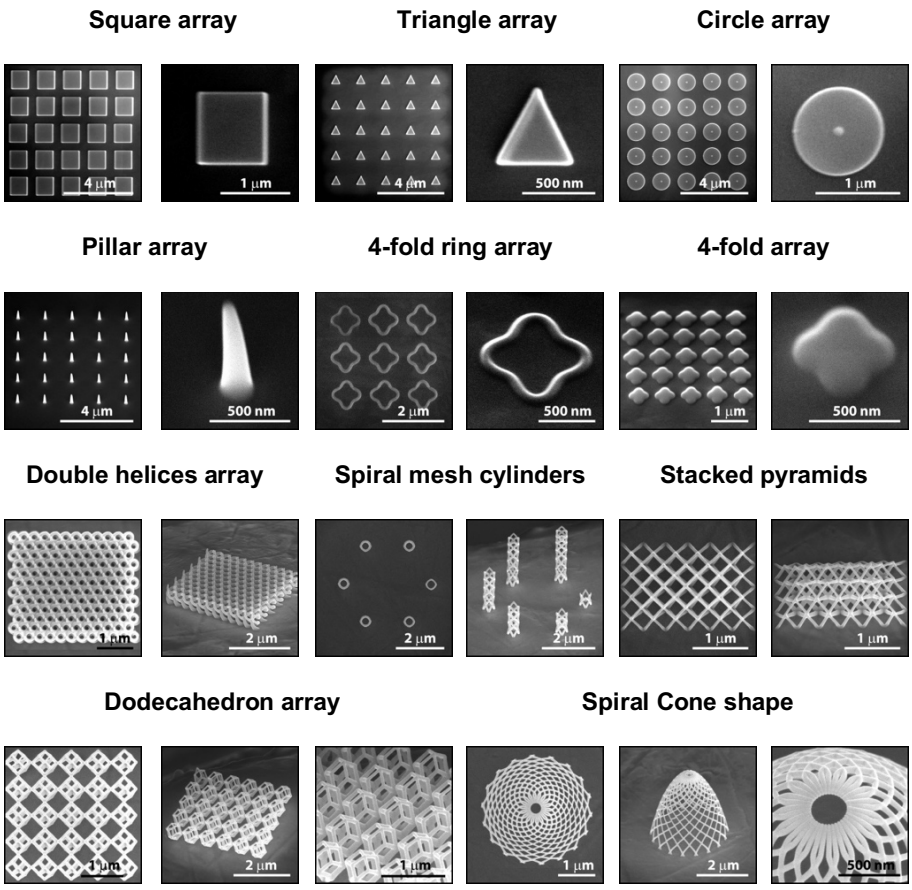

Figure S9
SEM images of the EBID structures produced on the titanium unit cell. Patterns and complex 3D shapes were fabricated to show the potential of the EBID process to generate free-form ornaments on a polished titanium unit cell. Furthermore, the SEM images from the last row demonstrate the growth of such shapes by EBID on local non-planar areas of the samples.

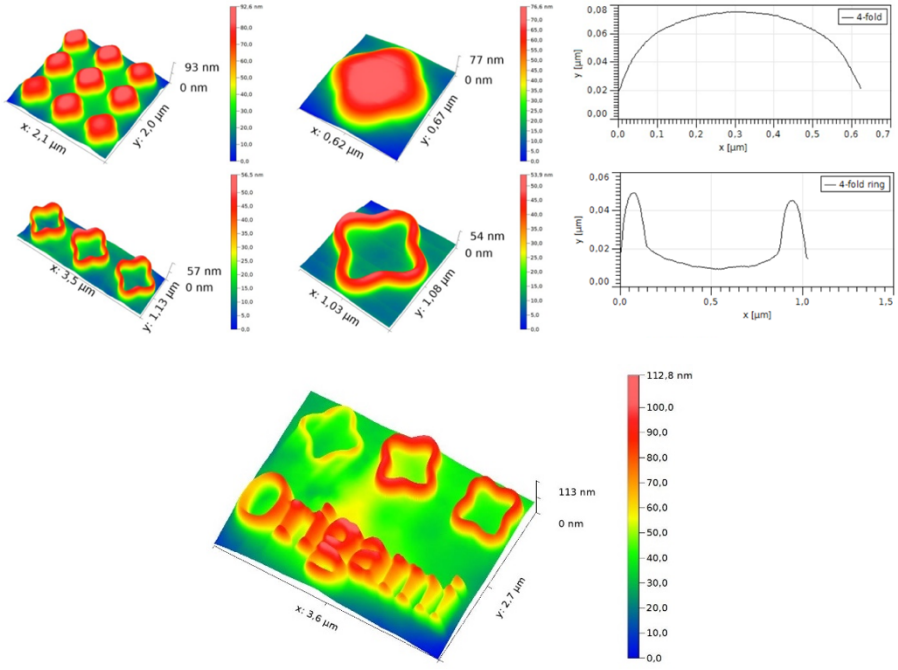

Figure S10
Selected AFM images of EBID structures with representative line profiles used to quantify the characteristic dimensions of the EBID structures.

Towards achieving that target, next research steps should focus on efficient EBID nano-patterning of large surface areas possibly by using multi-beam scanning electron microscopes[51], pattern transfer using EBID mask[52] or nanoimprinting of EBID stamps, assessment of stability and functionality of the EBID deposits after folding of the structures, optimization of patterns chemistry for specific applications by developing novel precursors[53,54]. Furthermore, combining EBID with complementary patterning methods such as the laser micro-machining technique could be used to achieve multiscale (micro/nano) structures integrated in a single 3D architecture. Such architectures may be of further interest for mimicking specific biological niches. The main dimensions of the structures, as determined from AFM, SEM and stream files are presented in Table S2.

Chapter 7

Programming the shape-shifting of flat soft matter: from self-rolling/self-twisting materials to self-folding origami

Materials Horizons (2016, 3, 536)

Nature uses various activation mechanisms to program complex transformations in the shape and functionality of living organisms. Inspired by such natural events, we aimed to develop initially flat (i.e. two-dimensional) programmable materials that, when triggered by a stimulus such as temperature, could self-transform their shape into a complex three-dimensional geometry. A two-dimensional starting point enables full access to the surface, e.g. for (nano-) patterning purposes, which is not available in most other manufacturing techniques including additive manufacturing techniques and molding. We used different arrangements of bi- and multi-layers of a shape memory polymer (SMP) and hyperelastic polymers to program four basic modes of shape-shifting including self-rolling, self-twisting (self-helixing), combined self-rolling and self-wrinkling, and wave-like strips. The effects of various programming variables such as the thermomechanical properties of the hyperelastic layer, dimensions of the bi- and multi-layer strips, and activation temperature on the morphology of the resulting three-dimensional objects were studied experimentally and were found to cause as much as 10 folds change in the relevant dimensions. Some of the above-mentioned modes of shape-shifting were then integrated into other two-dimensional constructs to obtain self-twisting DNA-inspired structures, programmed pattern development in cellular solids, self-folding origami, and self-organizing fibers. Furthermore, the possibility of incorporating multiple surface patterns into one single piece of shape-transforming material is demonstrated using ultraviolet-cured photopolymers.

Nature uses various mechanical and physical mechanisms to program such events as shriveling at the surface of fruits, fast motions in plants, solar tracking in sunflowers, growth of the skin and organs of various creatures during their metamorphosis cycle, and the folding mechanism observed in pine cone. The mechanisms include development of cellular and extracellular layers [1,2], swelling[3], inhomogeneous contraction or expansion of underlying elements [4], different effects of dehydration on different layers [4,5], and activation of snap-through instabilities [6-8]. For example, the folding mechanism observed in pine cone aimed to release the embodied seeds and the coiling (twisting) of certain seed pods are both caused by differences in the layers in terms of dehydration and orientation of reinforcing cellulose fibrils [4,5]. Another example is the swelling of tissues in ice-plants that unfolds the origami-like structures that protect the seeds during the drying period [3]. Finally, very fast motions of Venus flytrap leaves are the result of activation of snap-through instabilities via contraction (expansion) of their interior (exterior) layers [6-8].

The above-mentioned mechanisms that are exploited by nature to program the growth, movement, and morphogenesis of living creatures could be imitated to create materials with advanced functionalities and attractive properties. In particular, materials made from multiple layers and combined with activation mechanisms such as shape memory materials [9-12] or swelling gels could be used for development of programmable materials. A number of such programmable materials have been proposed recently. Bi-layer materials are the simplest form of such constructions and could be programmed to exhibit (homogeneous) bending [13,14] and wrinkled surface [1,15,16]. A number of bi- and multi-layer materials proposed by different researchers have been discussed below.

Structures equipped with bendable features are shown to exhibit shape shifting or transition in their internal structure as a response to various stimuli such as temperature, light, moisture, electric and magnetic fields, high frequency, etc. [16-18]. Moreover, seedpod-like hygroscopic bilayer composites reinforced in different directions using thin aluminum oxide ribbons which are aligned in a hydrogel by means of magnetic fields have been designed to demonstrate self-rolling and self-helixing in presence of moisture [19,20]. In another study, Ionov *et al.* fabricated a polymeric star-like self-folding bilayer which could reversibly encapsulate and release cell particles [21]. Dissimilar swelling properties can also provide the bending moment needed for rolling a polymer/polymer or metal/polymer bilayer composite [22]. Techniques such as ion dip-dyeing and transfer printing have been also used to program complex shape transformations in tough hydrogels from 1D to 2D, from 2D to 3D, and from 3D to more complex 3D shapes [23]. Alternative approaches such as 3D printing of composite materials as well as lithography techniques have been used to produce multi-materials with various types of functionalities [24,25].

In a different approach, heating up over the glass transition temperature has been used to shrink pre-strained polystyrene in-plan. Dark ink printed on either sides of such transparent sheet absorbs light selectively and locally heats up the polymer leading to inhomogeneous strain relaxation in the film and, thus, folding [26,27]. Surface traction can be also used to assemble the components of a 3D structure [28,29]. Graphene ink printed on the surface of pre-strained polystyrene sheets can absorb microwaves and warm up the underlying sections. Exceeding the glass transition temperature of polymer activates strain relaxation leading to selective folding [30]. Graphene oxide papers can be similarly programmed using through-the-thickness gradients to reversibly deform and fold in response to slight heating or light irradiation [31].

Embedding conductive elements in the structure of self-folding systems can help producing 3D electronics or active hinges applicable in automatic fabrication and robotics [32-36]. Equipped with shape memory polymers, origami structures can be transformed spontaneously in response to change in temperature [37]. Intelligent elements such as Joule-heated shape memory alloys could be used to program self-folding of origami structures to various configurations [38]. Edge activation in highly thin bilayers could prescribe hinge-like folding in bilayer structures [39], while step-controlled folding of origami-like structures has been shown to enable assembly of complex 3D structures [39,40]. Sequential folding of origami structures could facilitate the actuation of locking features once folding is completed [40,41].

The aim of the current study is to demonstrate the possibility of designing and programming initially flat (i.e. two-dimensional) structures that upon application of a stimulus undergo shape transformations and exhibit a complex three-dimensional geometry. This is in line with similar approaches reported in the literature recently [26,28,36-38]. The fact that such complex shape-shifting could be programmed into an initially flat structure opens up many possibilities for development of materials with advanced functionalities, because there is full access to the flat surface of the material before shape-transformation which could be used, for example, to introduce arbitrarily complex surface patterns onto the flat structure.

We used rationally-designed arrangements of simple elements for programming the desired shape-transformations based on bi- and multi-layers of active (i.e. shape memory) and passive polymers. Geometrical features, different arrangements of the passive and active polymers, and temperature fields were then used to program various types of shape transformations. Four basic modes of shape-shifting were defined including self-rolling, self-twisting (self-helixing), combined self-rolling and self-wrinkling, and shape-shifting to wave-like geometries. The basic shape-shifting modes were then combined with other two-dimensional structures to program more complex shape transformations in DNA-inspired constructs, patterned cellular solids, self-folding origami, and self-organizing fibers. To demonstrate the potential of

incorporating additional functionalities, surface patterns with various designs were incorporated into some of the presented shape-shifting materials.

Materials and methods

The shape-shifting materials presented in the current study were, in their simplest form, made of bi-layers constituting a soft hyperelastic layer and a shape memory polymer (SMP) layer. Tri- and multi-layers were used in more complex constructions. The SMP acted as a temperature-triggered activation mechanism. The mechanical properties of the soft hyperelastic layer, size and dimensions of the soft hyperelastic layer and the SMP, arrangement of both layers, and activation temperature were all utilized for programming the shape-shifting behavior of the developed materials.

Materials and material characterization

Three types of hyperelastic polymers with different mechanical properties were used in the current study including natural rubber (NR) (RX® Luna Para, Eriks, color: beige, nominal thickness: 1-3 mm), soft polyvinyl chloride (soft PVC) (RX® Mipolam, Eriks, color: honey yellow or clear, nominal thickness: 1-3 mm), and natural rubber/styrene-butadiene rubber (NR/SBR) (RX® Noma, Eriks, color: black, nominal thickness: 1-3 mm). Hyperelastic polymers generally show rubber-like mechanical behaviors and nonlinear elastic stress-strain curves. The hyperelastic polymers were chosen to be flexible enough for bending and show different types of change in their mechanical behavior in response to the applied high temperature. The mechanical properties and stress-strain curves of the three hyperelastic materials at different temperatures are presented in the supplementary document accompanying this paper (Figure S1, Table S1). A heat-triggered SMP (polyolefin, G. Apex, Taiwan Yun Lin Electronic Co. Taiwan, nominal thickness: 0.6 mm) with a 2:1 nominal shrink ratio, a minimum shrink temperature of 70° C (nominal value), and a minimum full recovery temperature of 110° C was used. Our experiments, however, showed that there is detectable shrinkage for temperature as low as 55° C. The percentage of shrinkage vs. activation temperature is presented in the supplementary document accompanying the paper (Figure S2). Polyolefin SMPs were chosen because they are among the most commonly used SMPs that show good flexibility and fast shape recovery. Moreover, they are widely available, inexpensive, and are good representatives of temperature-triggered SMPs that can be programmed for high strain recovery applications. A layer of ethyl cyanoacrylate (LOCITE® 401, Loctite) or methyl cyanoacrylate (LOCITE® 496, Loctite) adhesives approximately $35\ \mu m$ in thickness was used to bond the hyperelastic polymers to the SMP. In all cases, the actual thickness of the polymers was measured and used for presenting the results of the study. The mechanical and thermomechanical properties of the hyperelastic polymers were measured (see the electronic annex for the details of the material characterization tests).

Programming basic shape-shifting modes

Four basic arrangements of the hyperelastic and SMP layers were considered (Figure 1) each of which giving rise to one specific shape-shifting behavior. Some of these four basic types of shape-shifting behaviors were then used for programming more complex materials as described in the following sub-sections. In the first arrangement, strips made of hyperelastic polymer and SMP were adhesively bonded such that the axis of SMP activation coincided with the longitudinal axis of the bi-layer (Figure 1a). Temperature gradients could be used to trigger self-rolling in this type of arrangement (Figure 1a). In the second type of arrangement, the axis of SMP activation made 45° angle with the longitudinal axis of the bi-layer (Figure 1b). Activation of the SMP triggers self-twisting (self-helixing) in this type of arrangement (Figure 1b). In the third arrangement, alternating types of weak and strong adhesives were used to bond the SMP and hyperelastic polymer such that the axis of SMP activation was in parallel with the longitudinal axis of polymer (Figure 1c). Delamination of the weakly-bonded parts of the bi-layer caused by activation of the SMP triggers wrinkling as well as rolling in this type of arrangement (Figure 1c). Ultimately, discrete bands of hyperelastic polymer were alternatively attached to the either side of continuous SMP strip to create a tri-layer (Figure 1d). This flat tri-layer transforms to a curved wavy shape upon heat application (Figure 1d).

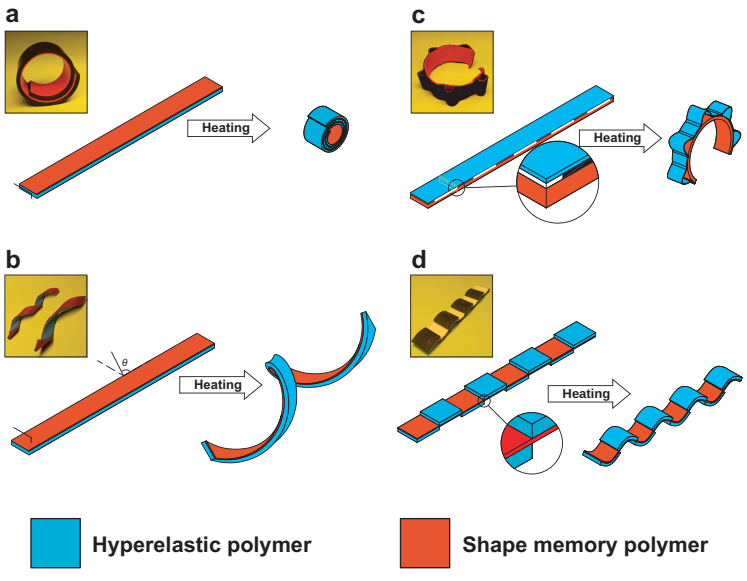

Figure 1
Basic modes of shape-shifting where a bi-layer of a SMP and a hyperelastic polymer transforms to a (a) rolled, (b) spiral, (c) wrinkled and rolled, or (d) wave-like structure.

The effects of the thermomechanical properties of the hyperelastic polymer and the dimensions of the bi-layer strips (thickness, width) in programming the final shape of the self-rolled and self-twisted structures were studied experimentally. The shape-transformation was triggered by submerging the bi-layers in a glass hot water bath (temperature = 80° C for self-rolling and 90° C for self-twisting) whose temperature was controlled by a magnetic stirrer (RET CV, IKA® Werke, Germany). The dimensions of the shape-transformed shapes were measured using digital images captured under optical microscope (Keyence VHX 5000) or using a calibrated digital camera. To measure the curvature of self-rolled structures, a circle was fitted to the points at the interface of the rolled bi-layer using a MATLAB (Mathworks, US) code. The curvature, exterior surface, and pitch size of the self-twisted (self-helixed) structures were measured using the image processing toolbox of MATLAB.

Self-twisting of DNA-inspired constructs

Two thin self-twisting bi-layer strips (width = 4 mm, thickness of the hyperelastic polymer = 2 mm) were attached to each other side-by-side using polylactic acid (PLA) rods to create some type of DNA-inspired structure. These are basically longer multi-segment versions of the basic shape-shifting mode illustrated in Figure 1b. The shape-shifting was triggered by gradual immersion of the construct in hot water container (temperature= 90° C) using a protocol similar to what described above.

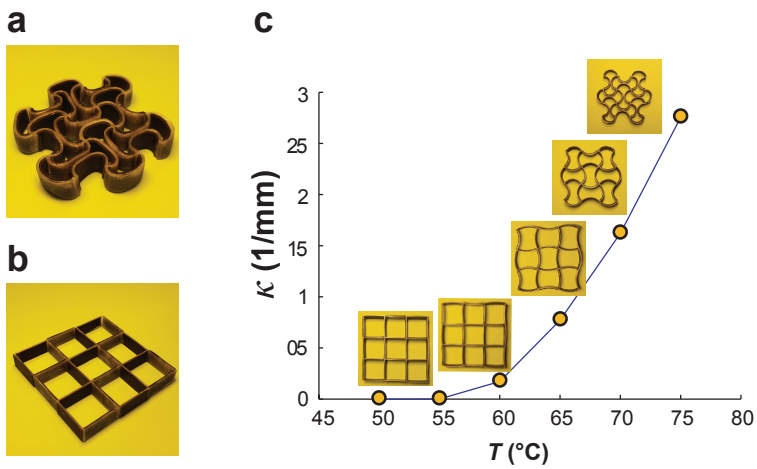

Figure 2
(a) The cell walls of a 3D-printed two-dimensional cellular solid were covered with the SMP. (b) The hourglass-shaped cells of the temperature-activated cellular solid after immersion in a hot water bath (temperature = 90°C). (c) The developed patterns and the curvature of the cell walls of the unit cells after immersion in hot water baths with varying temperatures. To insure the shape shifting process is complete, specimens were kept in the hot water bath for 30-40 sec.

Programmed pattern formation in cellular solids

A 3D printer (Ultimaker 2 Go, Ultimaker, The Netherlands) based on the fused deposition modeling (FDM) technology was used to manufacture a 3×3 square array (Figure 2a) from PLA. The dimensions of the unit cell of the resulting cellular structure was $25\ mm \times 25\ mm$ with a wall thickness of 1 mm. SMP layers were then adhesively bonded to the wall of the cellular solid based on a checker-board pattern. Upon SMP activation, the thin PLA walls bend (buckle) under compressive load and the square shape of unit cells initially transforms to some type of hour-glass shape which then progresses further to generate more complex patterns. Activation temperature was used to control the programmed shape-shifting in the cellular material and the effects of temperature on the generated pattern were studied experimentally by changing the temperature between <50° and 90° C. The curvature of the deformed walls was measured using a similar protocol as described above.

Self-folding origami

A different 3D printer based on the direct light projection technology (Prefactory® 4, EnvisionTEC, Germany) was used to fabricate six square-shaped elements from a liquid photo-reactive acrylate resin (R5-Gray EnvisionTEC, Germany) with a glass transition temperature of 120°-150° C. Together, these six elements create the unfolded shape of a cubic origami. The square elements (Figure 3a) were designed such that the SMP could be integrated into their structure (Figure 3b), attaching the elements together and providing the required activation mechanism for self-folding.

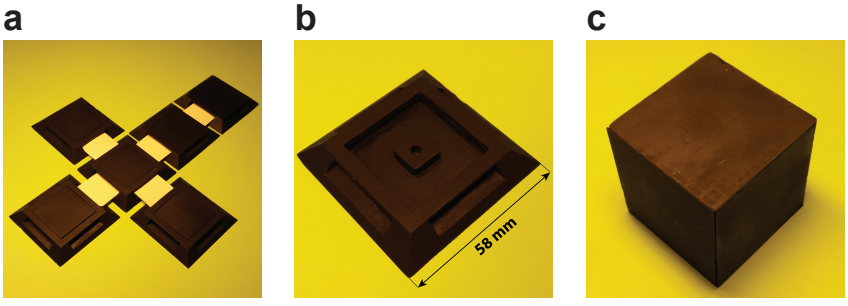

Figure 3
(a) The 3D-printed square elements used for creating the six sides of the unfolded cubic origami. (b) The assembly of the rigid square elements and the SMP into a self-folding origami structure. (c) The final configuration of the folded origami.

Self-organizing fibers

Narrow multi-layer constructs were made where the SMP strip served as the middle layer and hyperelastic polymers were attached on the either side of the SMP (Figure

4). The adhesive layer on both sides of the SMP incorporated thin layers of conventional paper tape (every 10 *mm*, a piece of conventional paper tape with the length of 5 *mm*) to facilitate delamination of the layers once the SMP was activated. The five-layer constructs had very small widths ($0.4 - 0.8\ mm$) as compared to their thickness (2 *mm*) which further helped delamination in weakly bonded regions (i.e. the locations where thin paper tape was applied). A number of multi-layer fibers prepared according to the above-mentioned protocol were integrated into comb-like structures.

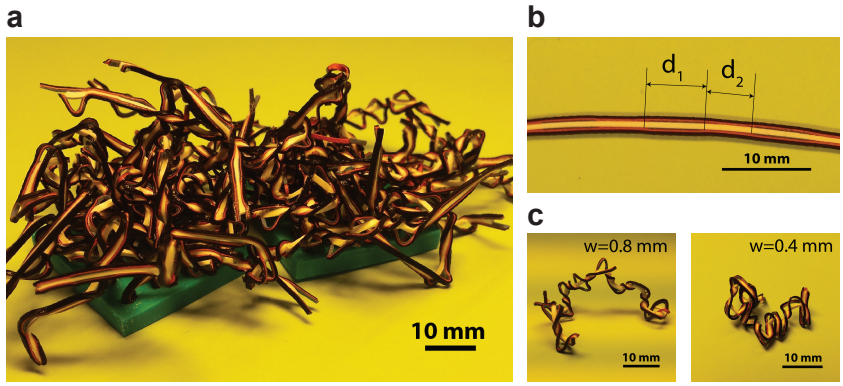

Figure 4
(a) Two comb-like arrangement of the self-organizing fibers entangled into each other after immersion in a hot water bath. (b) weakly-bonded (d_1) and strongly-bonded (d_2) hyperelastic polymers on both sides of the SMP (c) decrease in the width of the fibers increases their flexibility. The specimens were submerged in the hot water bath for 2−3 *min*.

Integration of surface patterns

To demonstrate the possibility of incorporating surface patterns into shape-shifting materials, self-twisting (self-helixing) materials with different types of surface patterns were developed. The hyperelastic polymer in the shape-shifting bi-layer was patterned by applying a thin layer of photosensitive polymer resin (a mixture of acrylated monomers and oligomers as well as photo initiators) (Flexible FLGR01, Formlabs, US). Different pattern shapes including circle, square, wavy, and stripped were used to demonstrate the possibility of incorporating a wide range of patterns in one single shape-shifting construct. Different pattern shapes were printed on transparent sheets using a Xerox printer to create different masks. The transparent masks were then placed on top of the hyperelastic polymer. A glass plate was compressed on top of the transparent mask to ensure uniform thickness of the liquid photosensitive polymer between the hyperelastic polymer and the mask. An ultraviolet (UV) chamber (Sun Ray 600, 150 mW/cm^2, used in the half-power mode, Integrated Dispensing Solutions

Inc.) was used to irradiate the masks with UV beams for ≈3 min, after which the masks were pealed from the cured photopolymer layer. The dark (printed) locations on the mask prevented transmission of the UV beam leaving pillars on the surface, while the transparent areas allowed UV transmission and, thus, direct curing of the photosensitive polymer below them, thereby creating pits. To invert the locations of pits and pillars on the surface, a mask with negatively printed patterns was used.

Results

Upon activations, the structures designed to exhibit the basic shape-shifting modes behaved as expected and respectively exhibited self-rolling (Figure 1a), self-twisting (Figure 1b), combined self-wrinkling and self-rolling (Figure 1c), and a wave-like geometry (Figure 1d). The programming variables investigated here were found to notably influence the resulting shape (Figure 5). For example, the radius of curvature in self-rolling could be changed with as much as ≈2 folds when the thermomechanical properties of the hyperelastic polymer were changed (e.g. compare soft PVC with NR/SBR in Figure 5a-b). Generally speaking, NR/SBR specimens showed the highest radii of curvature as compared to two other hyperelastic polymers (Figure 5a-b). Changing the width of the bi-layers from 2 mm to 12 mm changed the radius of curvature of the resulting structures by as much as ≈3 folds (Figure 5a). The thickness of the hyperelastic polymer also strongly affected the radius of curvature of the self-rolled constructs (Figure 5b): changing the thickens of the hyperelastic polymer from 1 mm to 3 mm resulted in as much as ≈10 folds increase in the radius of curvature (Figure 5b).

The helices formed in the self-twisting materials showed similar trends (Figure 5c-d). The radius of the helix curvature and its pitch changed by as much as ≈3 folds, depending on the hyperelastic polymer used (Figure 5c). Changing the width of the bi-layer strips between 2 mm and 10 mm strongly influenced both radius of curvature and the pitch of the helix (Figure 5c-d). The radius of curvature was the largest for NR/SBR (Figure 5c). For small widths of the bi-layer strip (i.e. <6 mm), the helix pitch was the highest for the PVC specimens (Figure 5d). The pitch size was the highest for soft NR/SBR when the width of the strip exceeded 6 mm (Figure 5d). The sensitivity of the pitch to width was very much dependent on the type of the hyperelastic polymer (Figure 5d). While for NR and NR/SBR specimens the changes in the pitch with width were modest, changing width resulted in large changes in the pitch size for soft PVC (Figure 5d).

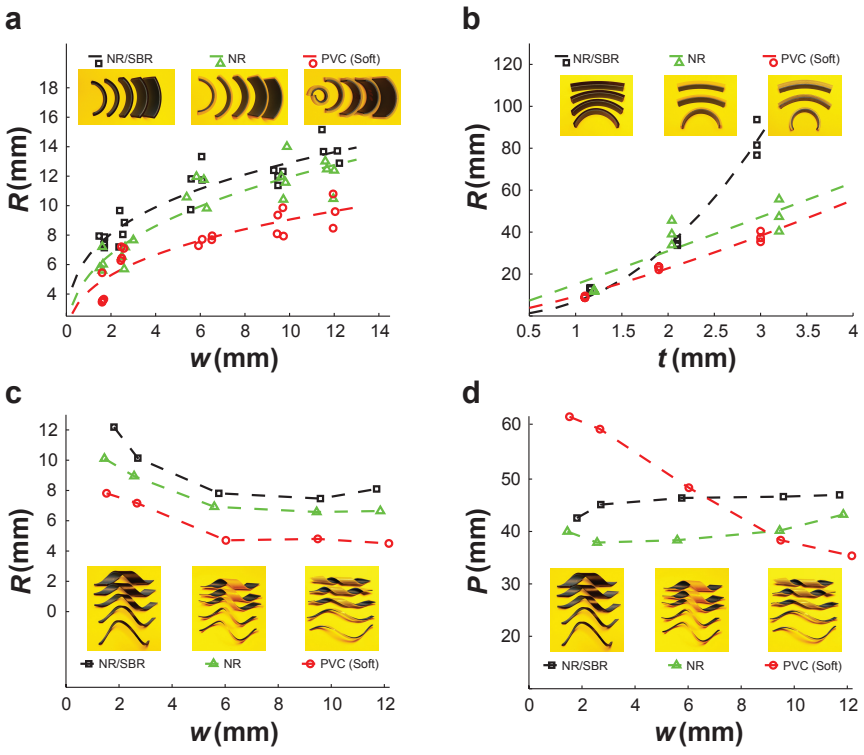

Figure 5
The effects of the width of the bi-layer strip (a) and the thickness of the hyperelastic polymers (b) on the radius of curvature of self-rolled materials. The effects of the width of the bi-layer strip on the radius and curvature (c) and pitch size (d) of the resulting helix. To insure the maximum shape shifting is achieved, samples were held for $35-45$ *sec* in the hot water bath.

The trailing edge of the SMP layer developed certain curvature after self-rolling or self-twisting (Figure 6). The curvature was clearly visible in several views of the structures with a size depending on the geometrical parameters defining the bi-layer such as the width of the bi-layer strip (Figure 6). While curvature was notably visible in the lateral view of self-rolling structures (Figure 6a), it was very small in their axial view (Figure 6b). As for the self-twisting constructs, the edge effect was similar regardless of the angle of view or location within the construct (Figure 6c-d). No such edge effects were observed in the hyperelastic polymers particularly the ones with larger thicknesses (Figure 6a-d).

Gradual immersion of the DNA-inspired structure in hot water bath resulted in gradual self-twisting and formation of a DNA-like structure (Figure 7a). Shape-shifting started from the bottom part of the structures and propagated upward as a larger part of the structure was submerged (Figure 7a). The time sequences of all

shape-shifting events are presented in Figure 7, while the captured movies can be found in the accompanying supplementary material.

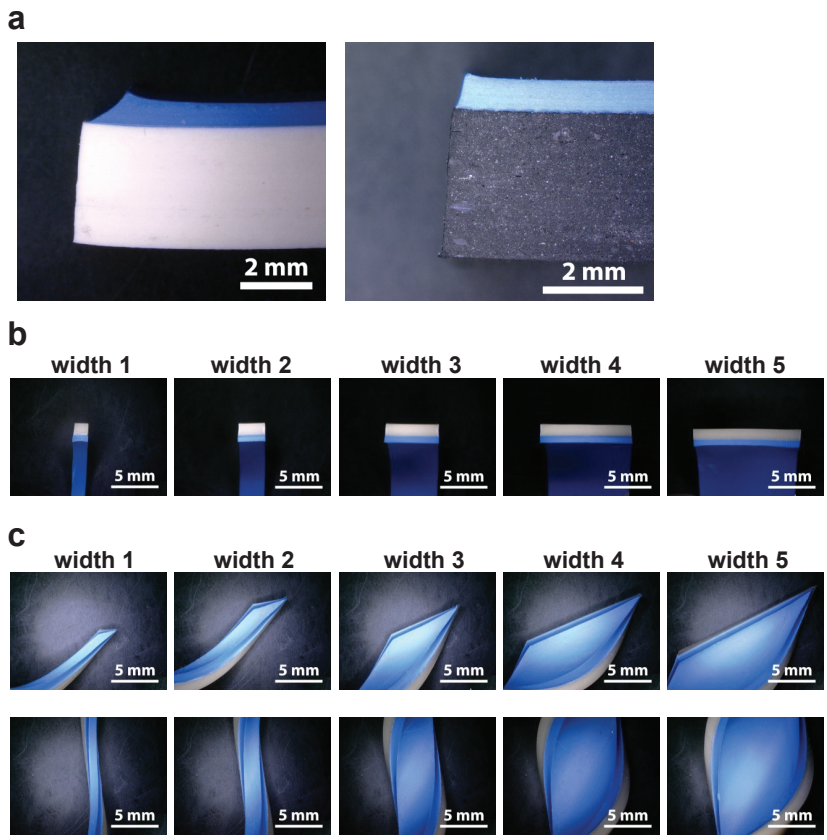

Figure 6
Microscopic images of self-rolled and self-twisted (self-helixed) structures: (a) the trailing edge of the SMP layer in the self-rolling structure is curved due to non-symmetric boundary conditions at its (free) top and (stiff) bottom surfaces. (b) The SMP layer in the self-rolling structures does not show lateral curvature regardless of the width of the bi-layer. (c) The angles and curves observed at the free end of the self-twisting structures with different widths. (d) The angles and curves observed in the middle part of self-twisting structures with different widths.

Gradual immersion of the origami also resulted in self-folding into the intended cubic shape (Figure 7c, where two sides of the cube were removed to facilitate observation of the self-folding process). At the beginning of the deformation, some hinges of the cubic structure were bent more than 90° (Figure 7c). However, further shrinkage of the SMP strip and subsequent sliding of the 45°-sloped edges of the adjacent square elements helped the structure to finally reach its planned shape (Figure 7c).

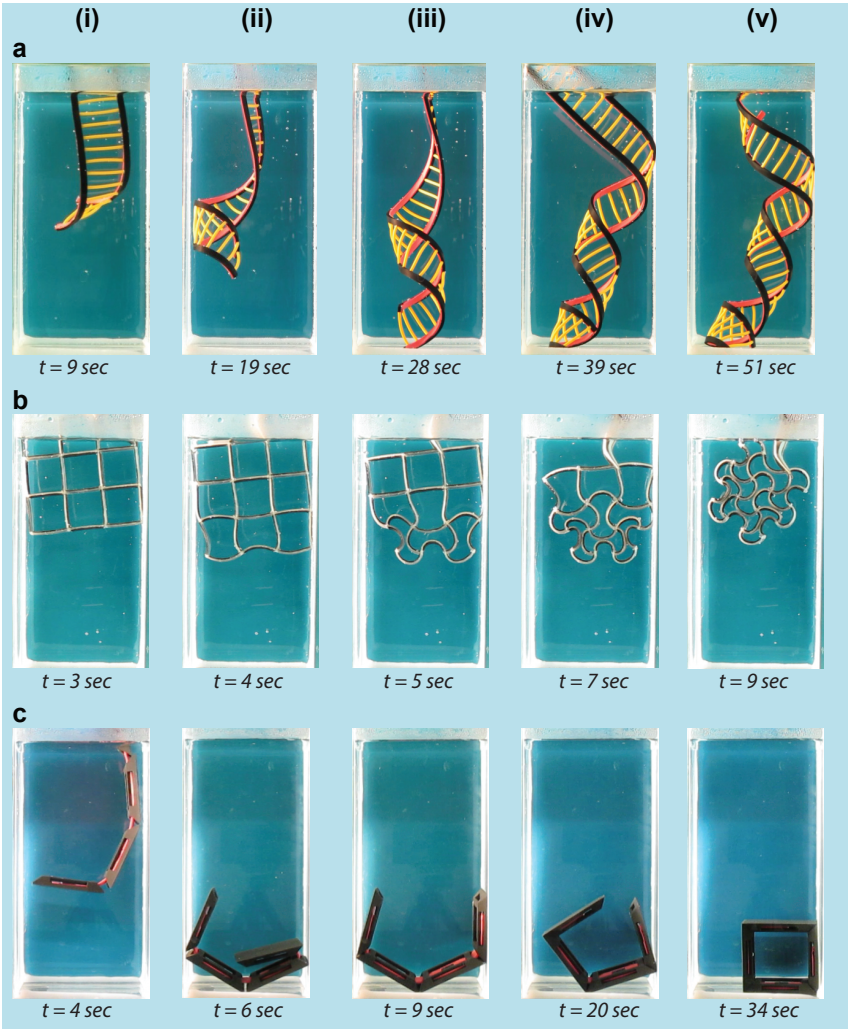

Figure 7
The time sequence of the shape transformations in (a) self-twisting DNA-inspired structure (b) two-dimensional cellular solids, and (c) self-folding origami.

The activation temperature significantly influenced the pattern formed in cellular solids (Figure 2b-c). In temperatures up to 50°C, the geometry of the cellular solid remained unchanged after immersion in hot water. For temperature above 50°C, the shape of the cellular solid gradually changed with exponentially growing curvature of the unit cell walls as the temperature increased from 55°C to 75°C. The walls of the unit cell were curved around the central point of the unit cell with alternating

horizontal/vertical collapsing of the unit cells (Figure 2c). At 75°C, the cell walls came into contact with each other (Figure 2c). The central part of the arced cell walls was flattened once the activation temperatures exceeded 80°C (Figure 2b). The patterns developed gradually as larger parts of the cellular solid was submerged in the hot water bath (Figure 7b).

In the self-organizing fibers, delamination of the hyperelastic polymers at the locations where the bonding between layers was weak (the delamination zones) led to the buckling of the hyperelastic polymers. This was due to the fact that the length of the SMP layer was decreased after activation, while the hyperelastic polymers did not change in length. At each delamination zone, the hyperelastic polymer buckled to a different direction depending on which side had the weakest bond. The random distribution of buckling direction resulted in the curly shape of the initially straight fibers (Figure 4c-d). We observed that the curvature of the curly fibers was dependent on their width and generally increased as the width decreased (e.g. compare Figure 4c with Figure 4d). Our preliminary tests also showed that the ratio of the length of the delamination zone to that of the bonded zone (i.e. d_1/d_2 in Figure 7b) must be larger than unity to ensure the thickness of the paper tape does not prevent the SMP layer from proper bonding to the hyperelastic polymers. Arranging the fibers in two comb-like structures and activating the SMPs resulted in entanglement of the combs into each other (Figure 4a).

The self-twisting (self-helixing) strips with surface patterns were observed under microscope and showed the imprinted patterns with one single strip showing multiple surface patterns on the various sides of a self-twisted helical shape (Figure 8).

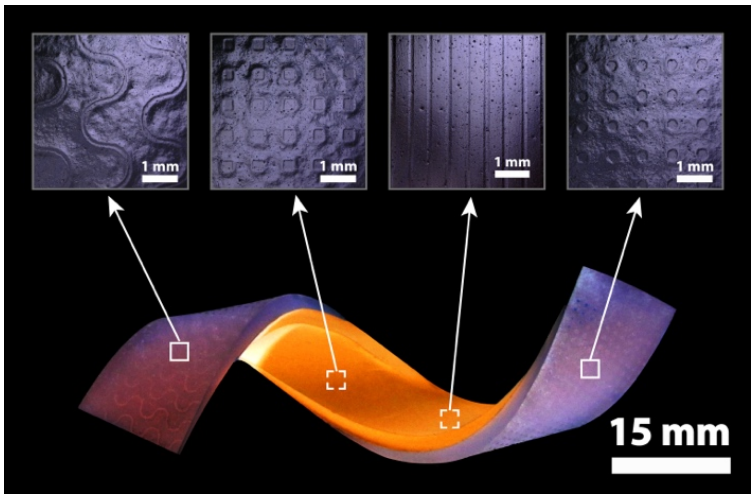

Figure 8
One single piece of self-twisted helix incorporating various types of surface patterns.

Discussion

The most important conclusion of the current study is that by combining soft (hyperelastic) polymers with simple SMP, it is possible to design and program shape transformations in initially flat (i.e. two-dimensional) structures so as to obtain complex three-dimensional geometries. The starting points of all cases presented here including the basic modes of shape-shifting, the DNA-inspired structures, programmed shape-shifting in cellular solids, self-folding origami, and self-organizing fibers were flat (i.e. two-dimensional) objects.

The results of this study also show the importance of various variables that could be used for programming the desired shape-shifting behavior. By changing the thermomechanical properties of the passive hyperelastic polymer, the dimensions of the bi- and multi-layer strips, and the activation temperature, the shape of the resulting three-dimensional objects could be controlled. In some conditions, the dimensions describing the shape of the resulting three-dimensional structure changed by as much as ≈10 folds when the above-mentioned parameters were modified. The arrangement of the passive and active layers together with the design parameters mentioned above provide a large space within which shape-shifting of two-dimensional structures to a wide range of three-dimensional objects could be programmed. Additional parameters such as the degree of anisotropy in the contraction of the SMP could be used to further enrich the space of programmable geometries. The measured radii of curvature and pitch exhibit some deviations from the fitted curves which are, in part, caused by spatial variations in the mechanical properties and shape shifting behavior of the hyperelastic and shape memory polymers. A few other secondary effects such as thickness variations also play a role.

Mechanistic aspects

In self-rolling structures, increasing both thickness and width of the bi-layer strips results in increased radius of curvatures after self-folding. All other parameters being constant, increasing the thickness of the hyperelastic polymer results in increased elastic force opposing the shrinkage of the SMP, thereby increasing the radius of curvature. Increasing the width of the bi-layer strips, on the other hand, increases both the flexural stiffness and the contraction force of the SMP per unit length, which is why the width of the bi-layer influences the radius of curvature only for small widths (i.e. $< \approx 10$ mm). For smaller widths, the radius of curvature increases with increased width of the bi-layer strips probably due to secondary effects such as edge effects and the instability and lateral forces that are more important for very thin strips. The absolute values of the radii of curvature are dependent on how large the contraction force of the SMPs is as compared to the elastic force of the hyperelastic layer at the elevated temperatures required for triggering the shape shifting behavior. In the case

of hyperelastic polymers that loose a significant portion of their mechanical properties at elevated temperatures, there might be some adjustments in the shape of the resulting self-rolling structures due to the increased elastic force of the hyperelastic polymer after cooldown. The shape adjustments are, however, expected to be relatively small, because after cooldown the increased elastic force of the hyperelastic polymer should overcome the elastic force (and not the contraction force) of the SMP to adjust the geometry of the self-rolled structure. The same mechanisms are at work when studying self-twisting constructs with the biggest difference being the angle of the hyperelastic polymer and SMP that further complicates understanding the exact distribution of the stresses and strains. Finally, the relationship between activation temperature and the shrinkage of the SMP is nonlinear (see supplementary document, Figure S2). The shrinking behavior of the SMP can therefore be adjusted within a large range by properly choosing the activation temperature. Increasing the activation temperatures could, thus, amplify the effects of the deformations caused by the SMP.

As for the edge effects observed both in self-rolling and in self-twisting structures, they are primarily due to the through-the-thickness difference between the surface of the SMP bonded to the hyperelastic polymer which is constrained in its deformation as compared to the free surface of the SMP that can freely deform. The width of the bi-layer strips also influences the edge effects, because the effects of such edge-related deformations are larger in strips with smaller widths, where the ratio of the perimeter of the bi-layer to the surface of the bi-layer is larger.

The shape transformations studied here are based on a number of underlying physical phenomena that need to be understood and preferably theoretically studied to enable more informed programming of the shape transformations and precise control of the dimensions of the resulting three-dimensional shapes. Increased temperature activates the SMP and results in anisotropic contraction of the SMP layer. The interaction of the SMP layer and the resisting hyperelastic polymer develops certain stress patterns that determine the course of shape transformation. Changing the activation temperature could be used to control the contraction force of the SMP layer. However, it has to be noted that the activation temperature might also change the mechanical properties of the hyperelastic material. The three hyperelastic polymers studied here were deliberately chosen to demonstrate three types of thermomechanical behavior: whereas the mechanical properties of the NR hardly change as the temperature increases from 20°C to 100°C, soft PVC exhibits tremendous loss of mechanical properties in the same temperature range (see accompanying electronic supplementary material for supporting experimental data). The thermomechanical behavior of NR/SBR is somewhere between the ones exhibited by NR and soft PVC. The thickness of the hyperelastic layer could be used as an additional parameter to control the resisting elastic force in bi- and multi-layers independent from the thermomechanical properties of the hyperelastic polymer. The

width of the strips influences the elastic force as well and modifies the stress distribution in bi- and multi-layer constructs. However, width simultaneously changes the other dimensions of the resulting three-dimensional object and is, thus, a less flexible way of programming shape transformations.

Another physical mechanism used here for programming shape transformations is mechanical instability. Harnessing mechanical instability has recently received increasing attention as a technique for development of active materials [42-45]. The programmed pattern transformation observed for cellular solids (Figure 5), is an example of how instability patterns triggered by activation of the SMP could be used to program shape-transformations. Combination of instability and buckling with rational positioning of the SMP segments in cellular materials provide additional physical pathways for programming shape transformations. Although the patterns developed in the current study remain in-plane after shape-transformations, out-of-plane buckling could be harnessed in similar ways to trigger additional modes of shape transformations and provide further freedom in design of the resulting three-dimensional object.

Surface features: wrinkling and patterns

Combining three-dimensional shapes with complex surface features such as surface wrinkles and surface (nano-) patterns is one of the most important advantages of starting from a flat structure, because full access to the surface of the material is possible. Similar access to the surface is not available in other manufacturing techniques that enable fabrication of complex three-dimensional geometries such as 3D printing. In this study, we presented two techniques for creating surface features including delamination-assisted self-wrinkling of the surfaces (Figure 1c) and surface patterning using UV-cured photopolymers (Figure 8). The approach used for combining various patterns (Figure 8) is particularly powerful, as it can be extended to any other surface-patterning technique that works on flat substrates including (nano-) lithography and all other nano-patterning techniques.

If the feature sizes of the wrinkling and wavy structural elements are properly chosen, they could be used for controlling cell proliferation, migration, and alignment [46-48]. These wrinkling and wavy strips can create homogeneous or hierarchical, or even more complicated patterns [46]. Different studies have shown that surface features in different scales from several nanometers [49] to hundreds of micrometers [50] can enhance cell response in different ways. Patterning the external surfaces of the proposed wrinkling and wavy elements could be used to combine patterns at different scales with each other, thereby obtaining hierarchical surface patterns and achieving the required biological responses. For example, it has been shown that random surface topographies affect the collective cell response, while ordered topographies influence the individual cell behavior [51]. The wettability of a substrate is another critical cue

in determining the cell attachment capability. The cell-to-substrate adhesion is maximized when the wettability of the surface is moderate [51-53]. Architecting the surface of a substrate by tailoring the design of the larger wrinkling or wavy strips (through changing their pitch size and radius) and smaller engraved patterns (through changing the engraved pattern shape, size, and depth) could be very helpful in achieving the intended cell behavior [51].

Applications

The possibility of creating complex three-dimensional shapes from flat structures could have many applications in various areas of research. An important area of potential application for the developed materials is soft robotics as well as design and manufacturing of soft actuators. Moreover, SMPs could be used in the form of biocompatible and/or biodegradable polymers for development of medical devices [54]. Stimulus-responsive elements can be used for unpacking and assembly of very big size structures, encapsulation of micro/nanoscale particles, development of medical implants, 3D electronics, sensors and smart bodies. In particular, complex three-dimensional geometries could be used for designing materials with unprecedented or rare mechanical properties within the context of mechanical meta-materials [55].

One of the main applications of shape-shifting bilayers can be fabrication of 3D cell culture substrates. Interaction between cells and matrix has been found to be of great significance in many biological processes such as embryogenesis [56], tumorigenesis [57], and angiogenesis[46,58]. Some of the structural elements introduced in this study have a great potential in stimulating cell growth in biological systems for example by adjusting the curvature [59] in the geometry of tissue engineering scaffolds. When concepts proposed in the current study are used for fabrication of biomaterials, shape transformations might need to occur before bringing the biomaterial in contact with living organisms. In such an approach, the advantage of shape transformation would the possibility to start from a flat structure whose entire surface is fully accessible for any type of surface bio-functionalization and/or bio-nanopatterning including the techniques that work only on flat surfaces. The complex 3D shape that is required for proper functioning of the biomaterial can then be obtained through programmed shape transformations.

The three-dimensional shapes of the biomaterials used for tissue regeneration are important, because such parameters as the porosity, pore size, pore shape, and surface curvature could all strongly influence the rate of tissue regeneration [59]. The effect of scaffold geometry on tissue regeneration occurs through multiple pathways including regulation of the mechanical stimulus for tissue regeneration [60,61] as well as adjustment of mass transport properties such as permeability [62].

Conclusions

Programming shape-transformations in initially flat soft materials was studied in the current study with the aim of obtaining complex three-dimensional structures. Bi- and multi-layers of SMP and hyperelastic polymers were used for programming four basic modes of shape transformation including self-rolling, self-twisting (self-helixing), combined self-rolling and self-wrinkling, and generation of wave-like geometries. Some of the basic modes of shape transformation were then used for designing self-twisting DNA-inspired structures, programmed pattern formation in cellular solids, self-folding origami, and self-organizing fibers. An experimental study was performed to investigate the effects of various programming variables such as the thermomechanical properties of the hyperelastic layer, the thickness of the hyperelastic polymer, the geometrical dimensions of the bi- and multi-layers, and the activation temperature on the morphology of the obtained geometries. It was observed that the various parameters describing the resulting three-dimensional shapes could be changed by as much as 10 folds, when the above-mentioned parameters were adjusted. The possibility of incorporating multiple types of surface patterns in one single piece of shape-shifting structure was also demonstrated.

References

[1] L. Ionov, *Biomimetic 3D self-assembling biomicroconstructs by spontaneous deformation of thin polymer films*, J Mater Chem **22**, 19366 (2012).

[2] J. P. Vandenbrink, E. A. Brown, S. L. Harmer, and B. K. Blackman, *Turning heads: the biology of solar tracking in sunflower*, Plant Sci **224**, 20 (2014).

[3] M. J. Harrington, K. Razghandi, F. Ditsch, L. Guiducci, M. Rueggeberg, J. W. Dunlop, P. Fratzl, C. Neinhuis, and I. Burgert, *Origami-like unfolding of hydro-actuated ice plant seed capsules*, Nat Commun **2**, 337 (2011).

[4] A. R. Studart, *Biologically inspired dynamic material systems*, Angew Chem Int Ed Engl **54**, 3400 (2015).

[5] J. Dawson, J. F. V. Vincent, and A. M. Rocca, *How pine cones open*, Nature **390**, 668 (1997).

[6] C. Darwin, *Insectivorous plants* (Murry, London, UK, 1975).

[7] W. H. Brown, *The mechanism of movement and the duration of the effect of stimulation in the leaves of Dionaea*, Am J Bot **3**, 68 (1916).

[8] Q. Guo, E. Dai, X. Han, S. Xie, E. Chao, and Z. Chen, *Fast nastic motion of plants and bioinspired structures*, J R Soc Interface **12**, 0598 (2015).

[9] Q. Zhao, W. Zou, Y. Luo, and T. Xie, *Shape memory polymer network with thermally distinct elasticity and plasticity*, Sci Adv **2**, e1501297 (2016).

[10] T. Xie, *Recent advances in polymer shape memory*, Polymer **52**, 4985 (2011).

[11] H. Meng and G. Li, *A review of stimuli-responsive shape memory polymer composites*, Polymer **54**, 2199 (2013).

[12] J. Mohd Jani, M. Leary, A. Subic, and M. A. Gibson, *A review of shape memory alloy research, applications and opportunities*, Mater Des **56**, 1078 (2014).

[13] Z. Chen, G. S. Huang, I. Trase, X. M. Han, and Y. F. Mei, *Mechanical Self-Assembly of a Strain-Engineered Flexible Layer: Wrinkling, Rolling, and Twisting*, Phys Rev Appl **5**, 017001 (2016).

[14] L. Ionov, *Soft microorigami: self-folding polymer films*, Soft Matter **7**, 6786 (2011).

[15] Q. Wang and X. Zhao, *A three-dimensional phase diagram of growth-induced surface instabilities*, Sci Rep **5**, 8887 (2015).

[16] Y. Liu, J. Genzer, and M. D. Dickey, *" 2D or not 2D": Shape-programming polymer sheets*, Prog Polym Sci **52**, 79 (2016).

[17] S. Ahmed *et al.*, *Multi-Field Responsive Origami Structures: Preliminary Modeling and Experiments* 2013), p. V06BT07A028.

[18] Z. He, N. Satarkar, T. Xie, Y. T. Cheng, and J. Z. Hilt, *Remote controlled multishape polymer nanocomposites with selective radiofrequency actuations*, Adv Mater **23**, 3192 (2011).

[19] R. M. Erb, J. S. Sander, R. Grisch, and A. R. Studart, *Self-shaping composites with programmable bioinspired microstructures*, Nat Commun **4**, 1712 (2013).

[20] R. M. Erb, R. Libanori, N. Rothfuchs, and A. R. Studart, *Composites reinforced in three dimensions by using low magnetic fields*, Science **335**, 199 (2012).

[21] G. Stoychev, N. Puretskiy, and L. Ionov, *Self-folding all-polymer thermoresponsive microcapsules*, Soft Matter **7**, 3277 (2011).

[22] V. Luchnikov, O. Sydorenko, and M. Stamm, *Self-Rolled Polymer and Composite Polymer/Metal Micro- and Nanotubes with Patterned Inner Walls*, Adv Mater **17**, 1177 (2005).
[23] X. Peng, Y. Li, Q. Zhang, C. Shang, Q.-W. Bai, and H. Wang, *Tough Hydrogels with Programmable and Complex Shape Deformations by Ion Dip-Dyeing and Transfer Printing*, Adv Funct Mater **26**, 4491 (2016).
[24] A. Sydney Gladman, E. A. Matsumoto, R. G. Nuzzo, L. Mahadevan, and J. A. Lewis, *Biomimetic 4D printing*, Nat Mater **15**, 413 (2016).
[25] V. Luchnikov, L. lonov, and M. Stamm, *Self-rolled polymer tubes: novel tools for microfluidics, microbiology, and drug-delivery systems*, Macromol Rapid Commun **32**, 1943 (2011).
[26] Y. Liu, J. K. Boyles, J. Genzer, and M. D. Dickey, *Self-folding of polymer sheets using local light absorption*, Soft Matter **8**, 1764 (2012).
[27] R. W. Mailen, Y. Liu, M. D. Dickey, M. Zikry, and J. Genzer, *Modelling of shape memory polymer sheets that self-fold in response to localized heating*, Soft Matter **11**, 7827 (2015).
[28] D. H. Gracias, V. Kavthekar, J. C. Love, K. E. Paul, and G. M. Whitesides, *Fabrication of Micrometer-Scale, Patterned Polyhedra by Self-Assembly*, Adv Mater **14**, 235 (2002).
[29] K. Kuribayashi-Shigetomi, H. Onoe, and S. Takeuchi, *Cell origami: self-folding of three-dimensional cell-laden microstructures driven by cell traction force*, PLoS One **7**, e51085, e51085 (2012).
[30] D. Davis, R. Mailen, J. Genzer, and M. D. Dickey, *Self-folding of polymer sheets using microwaves and graphene ink*, Rsc Advances **5**, 89254 (2015).
[31] J. Mu, C. Hou, H. Wang, Y. Li, Q. Zhang, and M. Zhu, *Origami-inspired active graphene-based paper for programmable instant self-folding walking devices*, Sci Adv **1**, e1500533 (2015).
[32] M. Shuhei, M. Laura, T. T. Michael, J. W. Robert, and R. Daniela, *Self-folding miniature elastic electric devices*, Smart Mater Struct **23**, 094005 (2014).
[33] S. Miyashita, C. D. Onal, and D. Rus, *Self-pop-up cylindrical structure by global heating* in *2013 IEEE/RSJ International Conference on Intelligent Robots and Systems*2013), pp. 4065.
[34] M. T. Tolley, S. M. Felton, S. Miyashita, L. Xu, B. Shin, M. Zhou, D. Rus, and R. J. Wood, *Self-folding shape memory laminates for automated fabrication* in *2013 IEEE/RSJ International Conference on Intelligent Robots and Systems*2013), pp. 4931.
[35] S. Miyashita, S. Guitron, M. Ludersdorfer, C. R. Sung, and D. Rus, *An untethered miniature origami robot that self-folds, walks, swims, and degrades* in *Robotics and Automation (ICRA), 2015 IEEE International Conference on* (IEEE, 2015), pp. 1490.
[36] S. Felton, M. Tolley, E. Demaine, D. Rus, and R. Wood, *A method for building self-folding machines*, Science **345**, 644 (2014).
[37] M. T. Tolley, S. M. Felton, S. Miyashita, D. Aukes, D. Rus, and R. J. Wood, *Self-folding origami: Shape memory composites activated by uniform heating*, Smart Mater Struct **23**, 094006 (2014).

[38] E. Hawkes, B. An, N. M. Benbernou, H. Tanaka, S. Kim, E. D. Demaine, D. Rus, and R. J. Wood, *Programmable matter by folding*, Proc Natl Acad Sci U S A **107**, 12441 (2010).
[39] G. Stoychev, S. Turcaud, J. W. C. Dunlop, and L. Ionov, *Hierarchical Multi-Step Folding of Polymer Bilayers*, Adv Funct Mater **23**, 2295 (2013).
[40] Y. Mao, K. Yu, M. S. Isakov, J. Wu, M. L. Dunn, and H. Jerry Qi, *Sequential Self-Folding Structures by 3D Printed Digital Shape Memory Polymers*, Sci Rep **5**, 13616 (2015).
[41] K. Yu, A. Ritchie, Y. Mao, M. L. Dunn, and H. J. Qi, *Controlled Sequential Shape Changing Components by 3D Printing of Shape Memory Polymer Multimaterials* in *IUTAM Symposium on Mechanics of Soft Active Materials, SAM 2014*, edited by K. Volokh, and M. Jabareen (Elsevier, 2015), pp. 193.
[42] S. Janbaz, H. Weinans, and A. A. Zadpoor, *Geometry-based control of instability patterns in cellular soft matter*, Rsc Advances **6**, 20431 (2016).
[43] J. T. Overvelde, S. Shan, and K. Bertoldi, *Compaction through buckling in 2D periodic, soft and porous structures: effect of pore shape*, Adv Mater **24**, 2337 (2012).
[44] S. C. Shan, S. H. Kang, P. Wang, C. Y. Qu, S. Shian, E. R. Chen, and K. Bertoldi, *Harnessing Multiple Folding Mechanisms in Soft Periodic Structures for Tunable Control of Elastic Waves*, Advanced Functional Materials **24**, 4935 (2014).
[45] S. C. Shan, S. H. Kang, P. Wang, C. Y. Qu, S. Shian, E. R. Chen, and K. Bertoldi, *Harnessing Multiple Folding Mechanisms in Soft Periodic Structures for Tunable Control of Elastic Waves*, Adv Funct Mater **24**, 4935 (2014).
[46] P. Yang, R. M. Baker, J. H. Henderson, and P. T. Mather, *In vitro wrinkle formation via shape memory dynamically aligns adherent cells*, Soft Matter **9**, 4705 (2013).
[47] C. C. Berry, G. Campbell, A. Spadiccino, M. Robertson, and A. S. Curtis, *The influence of microscale topography on fibroblast attachment and motility*, Biomaterials **25**, 5781 (2004).
[48] M. J. Dalby, N. Gadegaard, R. Tare, A. Andar, M. O. Riehle, P. Herzyk, C. D. Wilkinson, and R. O. Oreffo, *The control of human mesenchymal cell differentiation using nanoscale symmetry and disorder*, Nat Mater **6**, 997 (2007).
[49] W. A. Loesberg, J. te Riet, F. C. M. J. M. van Delft, P. Schon, C. G. Figdor, S. Speller, J. J. W. A. van Loon, X. F. Walboomers, and J. A. Jansen, *The threshold at which substrate nanogroove dimensions may influence fibroblast alignment and adhesion*, Biomaterials **28**, 3944 (2007).
[50] M. T. Eliason, E. O. Sunden, A. H. Cannon, S. Graham, A. J. Garcia, and W. P. King, *Polymer cell culture substrates with micropatterned carbon nanotubes*, J Biomed Mater Res A **86**, 996 (2008).
[51] N. M. Alves, I. Pashkuleva, R. L. Reis, and J. F. Mano, *Controlling cell behavior through the design of polymer surfaces*, Small **6**, 2208 (2010).
[52] Y. Arima and H. Iwata, *Effect of wettability and surface functional groups on protein adsorption and cell adhesion using well-defined mixed self-assembled monolayers*, Biomaterials **28**, 3074 (2007).

[53] J. Y. Lim, M. C. Shaughnessy, Z. Zhou, H. Noh, E. A. Vogler, and H. J. Donahue, *Surface energy effects on osteoblast spatial growth and mineralization*, Biomaterials **29**, 1776 (2008).
[54] A. Lendlein and S. Kelch, *Shape-Memory Polymers*, Angew Chem Int Ed **41**, 2034 (2002).
[55] A. A. Zadpoor, *Mechanical meta-materials*, Mater Horiz **3**, 371 (2016).
[56] M. A. Wozniak and C. S. Chen, *Mechanotransduction in development: a growing role for contractility*, Nat Rev Mol Cell Biol **10**, 34 (2009).
[57] S. Suresh, *Nanomedicine: elastic clues in cancer detection*, Nat Nanotechnol **2**, 748 (2007).
[58] D. E. Ingber, *Mechanical signaling and the cellular response to extracellular matrix in angiogenesis and cardiovascular physiology*, Circ Res **91**, 877 (2002).
[59] A. A. Zadpoor, *Bone tissue regeneration: the role of scaffold geometry*, Biomater Sci **3**, 231 (2015).
[60] D. P. Byrne, D. Lacroix, J. A. Planell, D. J. Kelly, and P. J. Prendergast, *Simulation of tissue differentiation in a scaffold as a function of porosity, Young's modulus and dissolution rate: application of mechanobiological models in tissue engineering*, Biomaterials **28**, 5544 (2007).
[61] J. A. Sanz-Herrera, J. M. Garcia-Aznar, and M. Doblare, *On scaffold designing for bone regeneration: A computational multiscale approach*, Acta Biomater **5**, 219 (2009).
[62] S. Van Bael, Y. C. Chai, S. Truscello, M. Moesen, G. Kerckhofs, H. Van Oosterwyck, J. P. Kruth, and J. Schrooten, *The effect of pore geometry on the in vitro biological behavior of human periosteum-derived cells seeded on selective laser-melted Ti6Al4V bone scaffolds*, Acta Biomater **8**, 2824 (2012).

Supplementary information

Thermomechanical characterization of the hyperelastic polymers

Three different types of rubber sheets were used as the passive layer of self-rolling and self-helixing bilayers. Rubber sheets were made of NR/SBR (natural rubber/styrene-butadiene rubber), NR (natural rubber) and soft PVC. Uniaxial tensile tests were performed to characterize the mechanical and thermomechanical properties of the rubbers. Specimens were tested at five different temperatures ($22, 40, 60, 80,$ and 100 ℃). An electromechanical testing machine (Zwick) with a $10kN$ load cell and pneumatic grippers equipped with an environmental chamber were used to stretch the strips up to 100% at a deformation rate of 10 mm/min. The strains were measured based on the movement of crosshead. Figure S1 illustrates the effect of temperature on the mechanical behaviour of different polymers. In ambient temperature, soft PVC is the stiffest material. Rise in temperature to 100 ℃ softens PVC very much such that this material shows the lowest stiffness compared to the other polymers. The stiffness of soft PVC drops to 3.2% of its stiffness in the ambient temperature as a result of increasing the temperature to 100 ℃. Natural rubber does not show significant change in its mechanical properties within the range of temperatures used here. The NR/SBR rubber exhibits 50% reduction in its stiffness as temperature is increased to 100 ℃. The initial Young's modulus of the three types of hyperelastic polymers are listed in Table S1. In addition, Polyolefin heat shrink polymer used in this study were tested to estimate the actual shrinkage ratio at different temperatures.

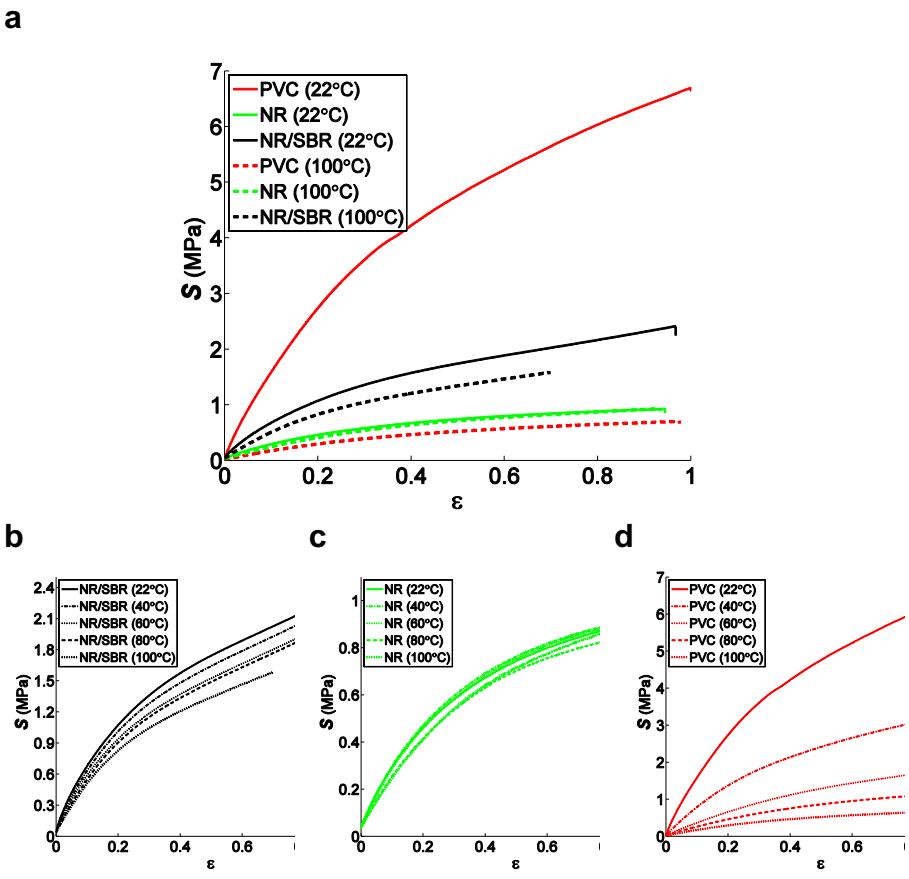

Figure S1. The thermomechanical behaviour of various hyperelastic polymers used in the current study.

Table S1. The initial Young's modulus of three different hyperelastic polymers used as the passive layer of self-rolling and self-twisting bilayers at ambient temperature and 100°C.

Material	E_0 **at 22**°C (MPa)	E_0 **at 100**°C (MPa)
NR/SBR	12.45	5.72
NR	3.83	2.40
Soft PVC	23.83	0.77

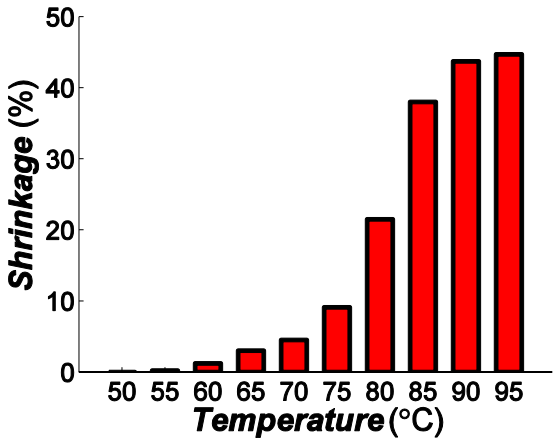

Figure S2. The shrinkage in the polyolefin SMP strips measured at different temperatures. The programmed SMP strips show a 4.5% shrinkage at 70°C.

Chapter 8

Programming 2D/3D shape-shifting with hobbyist 3D printers

Materials Horizons (2017,4, 1064)

Materials and devices with advanced functionalities often need to combine complex 3D shapes with functionality-inducing surface features. Precisely controlled bio-nanopatterns, printed electronic components, and sensors/actuators are all examples of such surface features. However, the vast majority of the refined technologies that are currently available for creating functional surface features only work on flat surfaces. Here we present initially flat constructs that upon triggering by high temperatures change their shape to a pre-programmed 3D shape, thereby enabling the combination of surface-related functionalities with complex 3D shapes. A number of shape shifting materials have been proposed during the last few years based on various types of advanced technologies. The proposed techniques often require multiple fabrication steps and special materials, while being limited in terms of the 3D shapes they could achieve. The approach presented here is a single-step printing process that only requires a hobbyist 3D printer and inexpensive off-the-shelf materials. It also lends itself to a host of design strategies based on self-folding origami, instability-driven pop-up, and 'sequential' shape shifting to unprecedentedly expand the space of achievable 3D shapes. This combination of simplicity and versatility is a key to widespread applications.

Materials that are programmed to develop 3D configurations from initially flat states propound a revolutionary approach with applications in biotechnology[1], electronics[2], and engineering of complex metamaterials[3]. Combining passive and stimuli-triggered active layers into a multilayer construct is often used for programming the basic modes of shape-shifting such as bending and twisting[4-8]. Swellable and shape memory polymers (SMP) are widely used as the active elements in such designs. Triggered by different stimuli such as increase in temperature, humidity, or light, active elements can drive the process of shape-shifting[9-12]. Temporal shape transition of programmed SMP without any external stimuli is reported as well[13]. Dimensional parameters and programming procedure as well as the activation conditions can control the quality of the deformations[8]. Complex 3D structures are then obtained through the rational arrangement of active elements in multi-ply constructs[4]. For example, active hinges can control the folding state of origami[5,14]. As an alternative to multi-layers, compressive stresses generated in swellable polymers could be used to induce complex shape-shiftings[15,16]. The sequence of folding may be tuned to avoid locking and could be used as a tool to drive the folding kinematics of highly complex structures and improve the integrity of the target configurations[17,18].

3D printing provides an alternative route to the programming of shape shifting: spatial arrangement of active (and passive) elements. In particular, sophisticated multi-material printing techniques could be used to combine different materials (e.g. hydrogel/polymer or polymer/polymer) to achieve multi-shape[19] or reversible shape-shifting[19,20]. Anisotropic addition of properties (e.g. swelling ratio or stiffness) can include a fourth dimension into 3D printing techniques to achieve the so-called 4D printing[19,21]. In a sharp contrast to the previously proposed techniques that require sophisticated or custom-made printers and spatial materials, here we present a versatile approach that requires no more than a hobbyist 3D printer and inexpensive off-the-shelf materials to implement many of the above-mentioned design routes and more.

Hobbyist 3D printers generally work on the basis of extrusion of polymeric filaments, a technology called fused deposition modeling (FDM) (Figure 1a). During the printing process, the filament experiences temperatures above its melting temperature while being stretched. The high temperature allows for stretching and alignment of polymer chains along the direction of extrusion, which due to the constraints applied during the printing process (see the supplementary document), is stored in the material as memory. Polylactic acid (PLA), a shape memory polymer with a melting temperature >180° C, is the most widely used material in hobbyist FDM printers. 3D printed (i.e. extruded) PLA filaments simultaneously decrease in length and thicken once heated above their glass transition temperature, T_g (Figure 1a). The percentage of decrease in the filament length could be controlled through

adjustment of the printing parameters including the extrusion and activation (i.e. triggering) temperatures as well as the layer thickness (Figure 1c-e). The flat surfaces are made of a number of layers with small thicknesses (50-200 μm). We used layers with identical patterns as well as stacks of layers with different patterns (Figure S2) to fabricate flat surfaces that show different combinations of directional strains (ε_1 and ε_2) upon exposure to temperatures exceeding T_g (Figure 1b). The negative planar strains are quite large (up to 0.27) while smaller positive strains (up to 0.06) are possible too (Figure 1b).

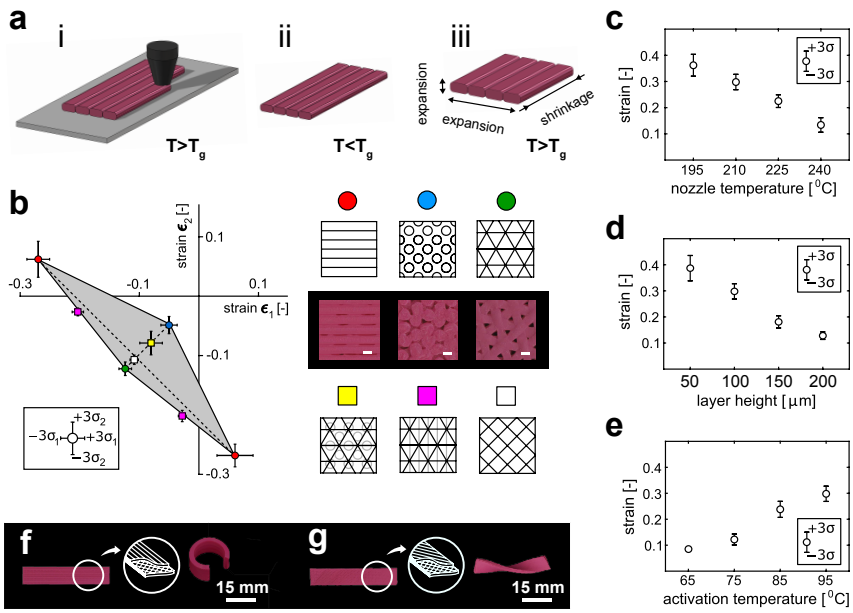

Figure 1
(a) As the filament is extruded during the printing process, it stretches and bonds with the previously printed layer. After cooling down below T_g, the stretching of the filament is stored as memory in the material. Upon heating above T_g, the material relaxes, resulting in shrinkage in the longitudinal direction and expansion in both other directions. (b) The printing pattern of multi-ply square panels regulates their in-plane strains. The grey area shows the range of possible directional strains that we measured for multipattern panels. (c-e) Both printing and activation parameters control the shrinkage of multi-ply panels. (f) Basic shape shifting in self-bending strips made by combining a longitudinal shrinking toplayer with a semi-passive bottom layer. (g) Changing the orientation of the toplayer results in self-twisting.

Flat surfaces (plies) with the desired deformation characteristics (i.e. ε_1, ε_2 duos) were then printed on top of each other for programming the desired shape transformation in the final multi-ply flat construct. The most basic mode of shape-shifting, i.e. a self-bending (self-rolling) strip, is achieved when a ply with relatively large anisotropic

deformation characteristics (e.g. ε_1 = -0.27, ε_2 = 0.06) is printed on top of a ply with relatively small isotropic deformation characteristics (e.g. ε_1 = -0.11, ε_2 = -0.11) (Figure 1f). The main straining direction of the ply with large deformation characteristics must be chosen to be in parallel with the length of the strip. The out-of-plane deformation occurs due to the resistance of the semi-passive ply against deformation of the active ply. If the main straining direction makes an angle with the length of the strip, a self-twisting (self-helixing) strip is made (Figure 1g). Both self-bending and self-twisting elements were used as actuating elements in the shape-shifting designs described below.

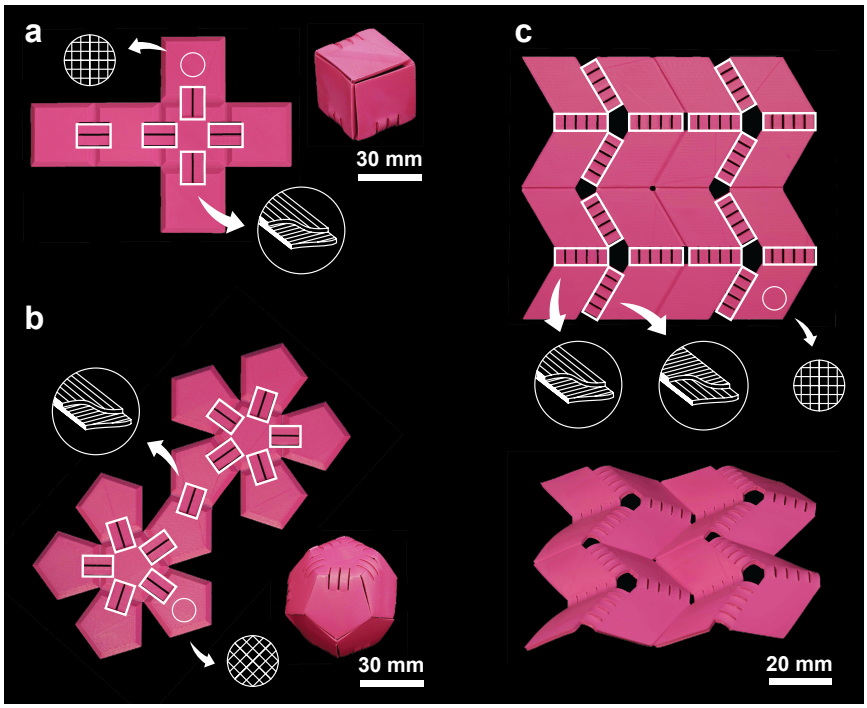

Figure 2
Self-bending elements (annotated on the figure as white rectangles) connect the semi-passive panels of origami structures. (a) A flat printed construct, consisting of 6 square panels connected by a thin layer to preserve the integrity of the structure, is folded into a cubic box upon activation (supplementary video 1). The printing patterns of the active bilayers and semi-passive panels are shown schematically. (b) Using the same method, a self-folding dodecahedron folds to it 3D shape (supplementary video 2). (c) The well-known Miura-ori folding pattern was printed and activated using two different types of self-bending elements (with different bending directions). The initially flat structure made of four Miura-ori units transforms its shape to the desired folded state upon activation (supplementary video 3).

Self-folding origami is one of the areas where semi-passive multi-ply panels with minimal deformation characteristics (e.g. ε_1 = -0.11, ε_2 = -0.11) that represent the rigid parts of the origami are combined with actuating elements that exhibit large out-of-plane deformations (Figure 2). The self-bending elements described above are the simplest types of such actuators. The width and thickness of the strips strongly affect the deformation characteristics (e.g. radius of curvature, Figure S4) and could therefore be used to adjust the actuation behavior of self-bending elements, thereby enabling a wide range of 3D shapes. Using multiple actuating elements -with different widths and thickness- in the same joint of a rigid origami not only allows for achieving different ultimate positions but also enables separation of the actuations kinematics from the actuation kinetics (i.e. actuation force). A self-folding box is the simplest type of self-folding origami that can be made with the above-mentioned techniques (Figure 2a). These design principles were found to be highly scalable and were, thus, applied to shapes with larger number of folds and more complex topologies such as a self-folding dodecahedron (Figure 2b). An example of a technically relevant 3D shape is the Miura-ori origami that has received much attention recently[22,23] and is studied as a model of rigid origami. Manual folding of Miura-ori origami is challenging, making it difficult to perform extensive and consistent experiments. We combined two types of self-bending actuators, which bend in different directions, with semi-passive panels representing the rigid parts of the design to make a self-folding Miura-ori origami (Figure 2c). Four actuators were used at each joint to increase the bending moment and overcome the locking caused by slight asynchronicities in the start of the bending of two or more actuators.

Derivatives of the basic shape-shifting modes could be used for obtaining more complex shapes. For example, two narrow self-helixing strips connected by a number of semi-passive horizontal elements were used to fabricate a DNA-inspired structure (Figure 3a).

Every shape-shifting design demonstrated so far has been based on combination of semi-passive panels with actuators. An alternative approach is to combine active panels that shrink in one direction and expand in another. In such a scenario, exposure to high temperatures creates compressive stresses that force some of the panels to buckle out of plane. The active panels are connected via thin printed layers that act as joints and folding lines. The buckling caused by externally applied compressive forces have been recently proposed as an effective way for transforming 2D shapes to complex 3D shapes[24,25]. The methodology we present here preserves the versatility of the buckling-induced 2D/3D shape transformations while taking it one step further by incorporating active elements, meaning not only that no external compressive forces are required but also that the number and complexity of the applied compressive forces could be drastically increased. To demonstrate some of the shapes that could be achieved through this approach, we designed self-folding

pyramids (Figure 3b), saddle shapes (Figure 3c), and boats (Figure 3d). To control the direction of the out-of-plane buckling, the thin connection between the panels could be replaced by some active bending elements. Using that approach, we assembled four pyramids (similar to Figure 3b) of which, after activation, two popped-up in one direction and the other two in the other direction (Figure 3e).

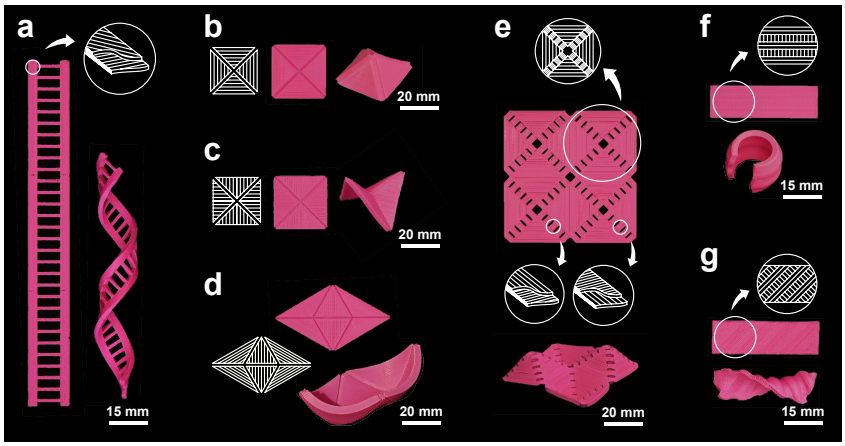

Figure 3
(a) Two initially flat self-twisting (bilayer) strands together with semi-passive connectors result in a DNA-inspired shape after activation (supplementary video 4). (b-d) The schematic of the monolayer panels with small grooves that were used to determine the folding lines. Compressive stresses generated by the anisotropic in-plane shrinkage of the panels result in out-of-plane buckling patterns that create the desired 3D shapes (supplementary video 5-6). (e) Self-bending elements were placed at the folding lines of a shrinking panel to control the direction of buckling (i.e. upward vs. downward) (supplementary video 8). (f) Parallel arrangement of expanding and shrinking strips results in a monolayer self-rolling element (supplementary video 7). (g) Arrangement of the expanding and shrinking strips with a 45° angle with respect to the longitudinal direction results in a monolayer self-twisting element (supplementary video 7).

In an alternative approach to multi-ply panels, we used single-ply strips to induce out-of-plane shape shifting. As opposed to the through-the-thickness arrangement of semi-passive and active plies used so far, the side-by-side alignment of shrinking and expanding monolayer strips can achieve self-bending (Figure 3f) and self-twisting when the direction of monolayer strips is oblique (Figure 3g). After activation, parallel buckling lines appear on the surface of these monolayer strips as a consequence of energy minimization in their constituting micro-elements. This single-ply approach provides an additional shape-shifting avenue that could be potentially integrated into multi-ply designs to extend the space of achievable 3D shapes.

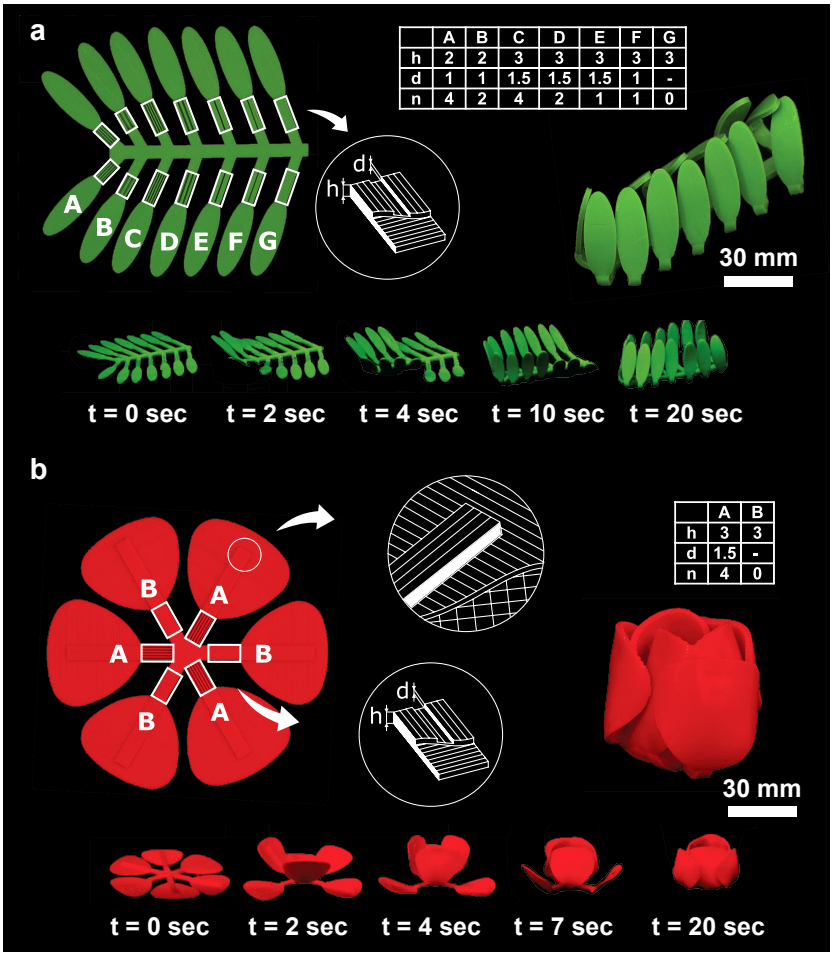

Figure 4
Sequential shape-shifting in two nature-inspired design. The active regions in both structures are highlighted by white rectangles while the geometry and printing patterns are shown schematically. Dimensions (*h*: thickness, *d*: groove depth) and number of grooves, *n* of the active elements are tabulated for both structures. (a) Gradual closure of the leaves of a structure resembling the shy plant. Sequential shape shifting was controlled by the thickness and the dimensions of the grooves in the bilayers (supplementary video 9). (b) Two-step folding of the initially flat petals to create a tulip. The time-lapses illustrate the sequence of folding for both designs (supplementary video 10).

The most complex types of 2D/3D shape shifting need to be performed in an ordered sequence of steps. In self-folding origami, for example, some folds need to occur before others, necessitating the ability to program 'sequential folding'. We used two strategies, namely variable porosity and variable thickness, to adjust the activation times of the active elements. Porosity was introduced to the panels by printing an

array of grooves. We changed the depth and number of grooves to make panels with different porosities. Heat transfer occurs more readily in panels with higher porosity, which in turns results in faster activation. Thickness variation could be also used to adjust the time of activation, because it takes more time for the thicker panels to reach T_g and go into the soft glassy state. Activation will not commence before almost the entire thickness of the panel has reached the glass transition temperature, as the stiffness of the panel is much higher at low temperatures[26]. Using both above-mentioned strategies, we incorporated sequential folding into two designs. The first design imitates the gradual closing of the leaves of the shy (i.e. Mimosa pudica) plant (Figure 4a). The second design (Figure 4b) is a self-folding tulip with initially flat petals that sequentially fold to create the multiple layers seen in natural tulips. When incorporated into the previously discussed design paradigms, time delays could tremendously enrichen the programmability of initially flat constructs by enabling multiple shape-shifting steps.

A number of points need to be discussed with respect to the shape-shifting behaviour of the structures developed here. First, the results of the current study clearly show that different printing parameters results in different shape-shifting behaviours (Figures 1b and S3). Changing the printing parameters could, among other effects, result in altered microstructure. Somewhat similar effects have been found in other studies[27]. The micro-architectural parameters of the printed structures such as the porosity could also affect the shape-shifting behaviour and were, for example, used for creating sequential folding. Second, the shape shifting behaviour of 3D printed PLA is activated by exposure to high temperatures. However, the homogeneity of the temperature field as well as the specific heat transfer conditions might be different based on the surrounding media. In addition, the other conditions of the surrounding environment such as humidity, pH, or liquid type could potentially affect the shape-shifting behaviour by changing the microstructure of the printed material. Similar effects have been observed in other kinds of shape-shifting materials[28]. Third, we used different in-plane arrangements of the 3D printed shrinking polymer to create shrinkage or expansion in lattice structures in response to the activation stimulus (e.g. Figure S5b-c). It would be also interesting to expand the current designs to create other kinds of negative/positive structural expansions similar to those reported in the literature[29]. There are, however, some limitations such as the resolution of FDM printing and the layer-by-layer manner of printing that could limit the range of achievable structural expansion coefficients. Finally, although the approach presented here is aimed at achieving permanent shape-shifting, similar designs based on multiple responsive materials could be also used for programming reversible shape transformations[30].

Given that a host of inexpensive 3D printers and PLA filaments similar to the ones used here are available in the market and that very complex 3D shapes could be

achieved, there is no to little practical barrier to the widespread application of the proposed shape shifting techniques. Advanced technologies that primarily work in 2D such as nanolithography, electron beam induced deposition[31], microarray printing[32], and direct-write electrospinning[33] together with the functionalities they offer could then be easily incorporated into 3D devices. The design principles and fabrication techniques presented here could be transferred and scaled to serve as a general platform for programming the shape shifting of flat materials and address the requirements of other printing technologies and materials.

References

[1] C. L. Randall, E. Gultepe, and D. H. Gracias, *Self-folding devices and materials for biomedical applications*, Trends Biotechnol **30**, 138 (2012).

[2] D. H. Gracias, J. Tien, T. L. Breen, C. Hsu, and G. M. Whitesides, *Forming electrical networks in three dimensions by self-assembly*, Science **289**, 1170 (2000).

[3] F. N. Xia, H. Wang, D. Xiao, M. Dubey, and A. Ramasubramaniam, *Two-dimensional material nanophotonics*, Nat Photonics **8**, 899 (2014).

[4] Y. Liu, J. Genzer, and M. D. Dickey, *" 2D or not 2D": Shape-programming polymer sheets*, Prog Polym Sci **52**, 79 (2016).

[5] S. M. Felton, M. T. Tolley, B. Shin, C. D. Onal, E. D. Demaine, D. Rus, and R. J. Wood, *Self-folding with shape memory composites*, Soft Matter **9**, 7688 (2013).

[6] G. Stoychev, S. Turcaud, J. W. C. Dunlop, and L. Ionov, *Hierarchical Multi-Step Folding of Polymer Bilayers*, Adv Funct Mater **23**, 2295 (2013).

[7] J. Mu, C. Hou, H. Wang, Y. Li, Q. Zhang, and M. Zhu, *Origami-inspired active graphene-based paper for programmable instant self-folding walking devices*, Sci Adv **1**, e1500533 (2015).

[8] S. Janbaz, R. Hedayati, and A. A. Zadpoor, *Programming the shape-shifting of flat soft matter: from self-rolling/self-twisting materials to self-folding origami*, Mater Horiz **3**, 536 (2016).

[9] Y. Liu, J. K. Boyles, J. Genzer, and M. D. Dickey, *Self-folding of polymer sheets using local light absorption*, Soft Matter **8**, 1764 (2012).

[10] M. Jamal, A. M. Zarafshar, and D. H. Gracias, *Differentially photo-crosslinked polymers enable self-assembling microfluidics*, Nat Commun **2**, 527 (2011).

[11] Q. Zhao, H. J. Qi, and T. Xie, *Recent progress in shape memory polymer: new behavior, enabling materials, and mechanistic understanding*, Progress in Polymer Science **49**, 79 (2015).

[12] L. Huang, R. Jiang, J. Wu, J. Song, H. Bai, B. Li, Q. Zhao, and T. Xie, *Ultrafast digital printing toward 4D shape changing materials*, Advanced Materials, 1605390 (2016).

[13] X. Hu, J. Zhou, M. Vatankhah-Varnosfaderani, W. F. Daniel, Q. Li, A. P. Zhushma, A. V. Dobrynin, and S. S. Sheiko, *Programming temporal shapeshifting*, Nat Commun **7**, 12919 (2016).

[14] J. H. Na, A. A. Evans, J. Bae, M. C. Chiappelli, C. D. Santangelo, R. J. Lang, T. C. Hull, and R. C. Hayward, *Programming reversibly self-folding origami with micropatterned photo-crosslinkable polymer trilayers*, Adv Mater **27**, 79 (2015).

[15] J. Kim, J. A. Hanna, M. Byun, C. D. Santangelo, and R. C. Hayward, *Designing responsive buckled surfaces by halftone gel lithography*, Science **335**, 1201 (2012).

[16] Z. L. Wu, M. Moshe, J. Greener, H. Therien-Aubin, Z. Nie, E. Sharon, and E. Kumacheva, *Three-dimensional shape transformations of hydrogel sheets induced by small-scale modulation of internal stresses*, Nat Commun **4**, 1586 (2013).

[17] Y. Mao, K. Yu, M. S. Isakov, J. Wu, M. L. Dunn, and H. Jerry Qi, *Sequential Self-Folding Structures by 3D Printed Digital Shape Memory Polymers*, Sci Rep **5**, 13616 (2015).

[18] Q. Ge, A. H. Sakhaei, H. Lee, C. K. Dunn, N. X. Fang, and M. L. Dunn, *Multimaterial 4D Printing with Tailorable Shape Memory Polymers*, Sci Rep **6**, 31110 (2016).
[19] J. Wu, C. Yuan, Z. Ding, M. Isakov, Y. Mao, T. Wang, M. L. Dunn, and H. J. Qi, *Multi-shape active composites by 3D printing of digital shape memory polymers*, Sci Rep **6**, 24224 (2016).
[20] D. Raviv *et al.*, *Active printed materials for complex self-evolving deformations*, Sci Rep **4**, 7422 (2014).
[21] A. S. Gladman, E. A. Matsumoto, R. G. Nuzzo, L. Mahadevan, and J. A. Lewis, *Biomimetic 4D printing*, Nature Materials **15**, 413 (2016).
[22] Y. Chen, R. Peng, and Z. You, *Origami of thick panels*, Science **349**, 396 (2015).
[23] M. Schenk and S. D. Guest, *Geometry of Miura-folded metamaterials*, Proc Natl Acad Sci U S A **110**, 3276 (2013).
[24] S. Xu *et al.*, *Assembly of micro/nanomaterials into complex, three-dimensional architectures by compressive buckling*, Science **347**, 154 (2015).
[25] Z. Yan *et al.*, *Controlled mechanical buckling for origami-inspired construction of 3D microstructures in advanced materials*, Adv Funct Mater **26**, 2629 (2016).
[26] D. Ratna and J. Karger-Kocsis, *Recent advances in shape memory polymers and composites: a review*, J Mater Sci **43**, 254 (2008).
[27] M. Malinauskas *et al.*, *3D microporous scaffolds manufactured via combination of fused filament fabrication and direct laser writing ablation*, Micromachines **5**, 839 (2014).
[28] S. Rekštytė, D. Paipulas, M. Malinauskas, and V. Mizeikis, *Microactuation and sensing using reversible deformations of laser-written polymeric structures*, Nanotechnology **28**, 124001 (2017).
[29] J. Qu, M. Kadic, A. Naber, and M. Wegener, *Micro-Structured Two-Component 3D Metamaterials with Negative Thermal-Expansion Coefficient from Positive Constituents*, Sci Rep **7**, 40643 (2017).
[30] Y. Mao, Z. Ding, C. Yuan, S. Ai, M. Isakov, J. Wu, T. Wang, M. L. Dunn, and H. J. Qi, *3D Printed Reversible Shape Changing Components with Stimuli Responsive Materials*, Sci Rep **6**, 24761 (2016).
[31] W. F. van Dorp, B. van Someren, C. W. Hagen, P. Kruit, and P. A. Crozier, *Approaching the resolution limit of nanometer-scale electron beam-induced deposition*, Nano Lett **5**, 1303 (2005).
[32] T. M. Harris, A. Massimi, and G. Childs, *Injecting new ideas into microarray printing*, Nat Biotechnol **18**, 384 (2000).
[33] J. Lee, S. Y. Lee, J. Jang, Y. H. Jeong, and D.-W. Cho, *Fabrication of patterned nanofibrous mats using direct-write electrospinning*, Langmuir **28**, 7267 (2012).
[34] F. S. Senatov, K. V. Niaza, M. Y. Zadorozhnyy, A. V. Maksimkin, S. D. Kaloshkin, and Y. Z. Estrin, *Mechanical properties and shape memory effect of 3D-printed PLA-based porous scaffolds*, J Mech Behav Biomed Mater **57**, 139 (2016).
[35] S. Timoshenko, *Analysis of bi-metal thermostats*, JOSA **11**, 233 (1925).

Supplementary information

General methods

3D printers (Ultimaker 2+, Ultimaker, The Netherlands) working on the basis of fused deposition modelling (FDM) and polyactic acid (PLA) polymeric filaments (Ultimaker, diameter = 2.85 mm, T_g = 60-65 °C) were used for fabrication of all designs presented in this work. PLA generally has good shape memory properties[34]. Samples were produced in the room temperature while the temperature of the glass print bed was set to 60 °C in order to improve the adhesion between the samples and the print bed. The PLA filaments were extruded through a standard 0.4 mm nozzle. A nozzle temperature of 210 °C, printing speed of 60 mm/s, filament flow of 2.1 mm^3/s, and layer thickness of 0.1 mm were used. Good adhesion between the fixed print bed and extruded material and the small gap between the nozzle and print bed, which result in swiping of the extruded filament by the moving nozzle tip, make sure that the melted material is stretched during printing. The stretched state of the melted filament will be frozen after cooling down and remains as memory in the body of the printed constructs. Should it not have been for the combined effects of swiping and material adhesion, no stress would have been accumulated and stored in the material. That was confirmed by a simple experiment in which PLA filaments extruded through the 3D printer nozzle using the same parameters as described above exhibited no memory.

The memory stored in the materials can be released by increasing the temperature above T_g while not constraining the printed structure at its boundaries. Printing patterns prescribe the directions of shrinkage and expansion into the body of printed constructs, which could be used as a tool for programming the shape-shifting of polymeric structures. A cubic glass water bath suitable for temperatures higher than T_g was used for activation of the printed structures, allowing us to track the deformations of the structures. The temperature of the water was controlled using a heating immersion circulator (CORIO CD, Julabo, Germany). Digital cameras were used to track the deformation of the studied specimens and a Matlab (Mathworks, version R2016b) code was used for image processing.

Effects of printing parameters on the directional strains of flat specimens

A number of test specimens (30×10×2 mm) were 3D printed with PLA filaments (color: silver). The extruded filaments were aligned in the longitudinal direction (the print path is shown in Figure S1a). The specimens were activated at 95 °C for at least 2 min to ensure the completion of the shape-shifting process. To provide free boundary conditions at both ends of the specimens, a weak connection was printed between the testing part of the specimen and its fixed end, which was attached to a

gripper to keep the specimen in place (Figure S1b). The specimens were marked with black dots in order to easily track the change in length with image processing. The effects of nozzle temperature, printing speed, filament flow, and layer thickness were experimentally studied where each parameter was independently varied from the standard settings set by the manufacture (see Section 1). In addition, the effects of activation temperature were experimentally investigated.

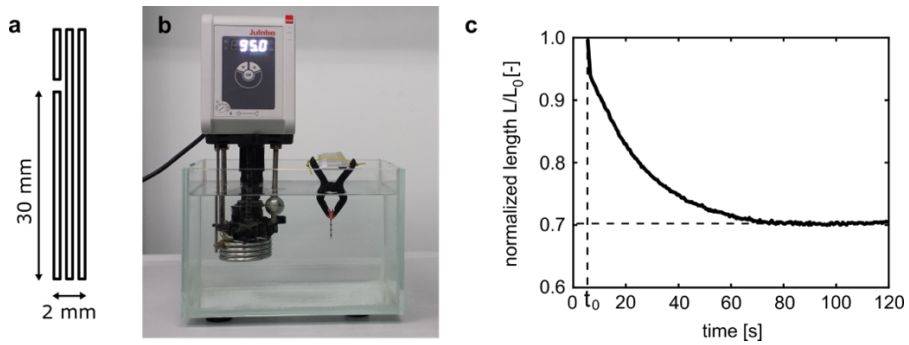

Figure S1
(a) The print path of each printed layer of the specimens. (b) The experimental setup used for activation of the specimens. The specimens were held by a gripper. (c) Change in the length of one sample specimen. The deformation starts at time t_0 after activation.

The strain vs. time curves followed similar paths (Figure S1c) but with different onset times, t_0, and maximum strains. Three of the five studied parameters were found to highly influence the strain induced in the specimens (Figure S2). Both reduction in the nozzle temperature and layer thickness increase the maximum strain. The maximum strain could be increased from 13% to 36% by lowering the nozzle temperature from 240 °C to 195 °C (Figure S2a). Decreasing the layer thickness from 0.2 mm to 0.05 mm results in a 3-fold increase in the maximum strain (38% for 0.05 mm, Figure S2b). The activation temperature also strongly affected the contraction in the longitudinal direction (Figure S2c). The amount of shrinkage increased from about 13% to 29% when the activation temperature increased from 65 °C to 95 °C. The printing speed and filament flow did not significantly influence the shrinkage of the specimens (Figure S2d-e). The filament flow is expressed as a percentage of the standard material flow of 2.1 mm^3/s (at a printing speed of 60 mm/s).

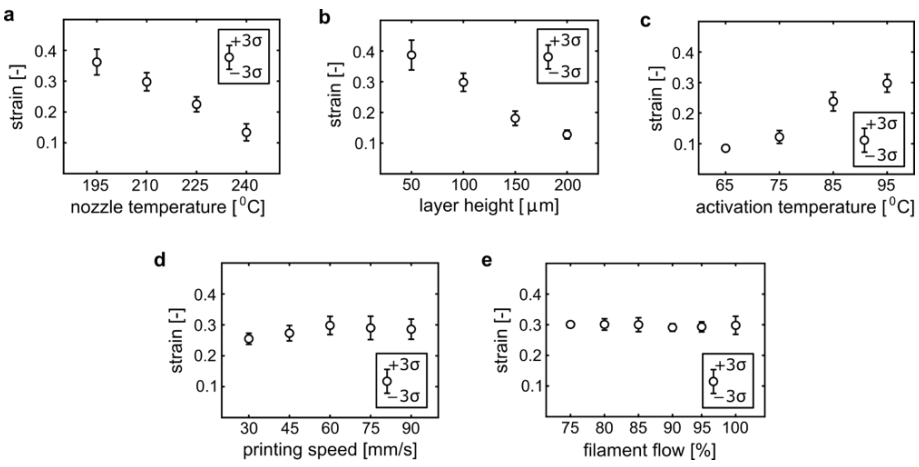

Figure S2
The effects of the printer settings and activation temperature on the shrinkage of the specimens. The average shrinkage over four tested specimens is plotted with the error bars representing three times the standard deviation from the mean.

The nozzle temperature highly influenced the shrinkage of the specimens. As the extruded filament cools down, some relaxation of the stretched polymeric chains happens before the temperature drops below T_g. Printing at higher temperatures gives more time for relaxation and less stress will be stored inside the printed samples. Increasing the layer thickness has a similar effect, because it increases the cooling time. Moreover, reducing the layer thickness enhances the level of stretching of the polymer chains during the printing process.

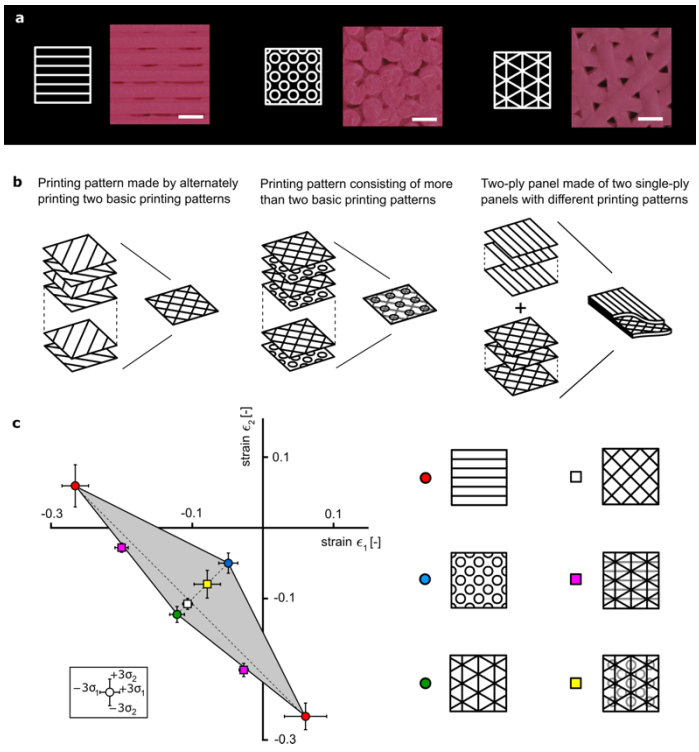

Figure S3
(a) Schematic representation and detailed images of the three basic printing patterns (scale bar = 0.5 mm). (b) Complex printing patterns and two-ply structures were made by combining basic patterns. (c) The effects of printing pattern on in-plane deformation. The average of four tested specimens is plotted and the error bars represent three times the standard deviation.

Effects of the printing pattern on the in-plane deformation of rectangular specimens

Different printing patterns were used for production of rectangular specimens (30×30×2 mm) from PLA filaments (color: silver). Three basic pattern designs, made by printing a stack of layers with identical patterns, were used (Figure S3a) together with a number of composite patterns, which were produced by printing a stack made of layers with different patterns (Figure S3b). The standard printer settings (see Section 1 of this document) were used. Activation was done at 95 °C for at least 2 min to ensure shape-shifting was complete. The length and width of the specimens before and after activation were measured using a caliper.

The deformation duos (normalized change in the length of the specimens in both in-plane directions) are plotted in Figure S3c. The alignment of the filament in one direction resulted in 27% shrinkage and 6% expansion in both orthogonal in-plane directions. Both circular and triangular printing patterns showed isotropic in-plane

shrinkage (5% and 12%, respectively). Alternating the printing direction between consecutive layers resulted in 11% shrinkage in both directions. Combining linear and triangular printing patterns resulted in highly anisotropic strains (ε_1 = -0.20, ε_2 = -0.03). On the other hand, the composite of triangular and circular printing patterns resulted in isotropic contractions equal to 8%.

A wide range of both isotropic and anisotropic in-plane deformation duos could be achieved by varying the printing pattern. Anisotropic deformations predominantly require layers with filaments aligned in one direction. Printing small circles severely limits the amount of stored deformation, reducing the shrinkage to only 5% in both directions. The triangular printing pattern shows the largest isotropic shrinkage of 12%. These three cases show some of the extremes of anisotropic and isotropic in-plane deformation that could be achieved by combining basic printing patterns into a composite pattern. The tested composite patterns showed in-plane deformations that were in-between those of the basic patterns they were made of.

The triangular pattern could be seen as a composite of three linear patterns rotated by 120°, although the triangular pattern is printed within one layer instead of printing three separate linear patterns on top of each other. However, the shrinkage is significantly different from the grid infill pattern (composite of two orthogonal linear patterns). The insets of Figure S3a show that the triangular pattern is more porous as compared with the grid infill pattern, which was confirmed by comparing the weights of both types of specimens. The average mass of a 30×10×2 mm specimen with triangular pattern and grid infill pattern were respectively 2.0 and 2.3 g. The larger porosity of the triangular infill pattern allows for more deformation (shrinkage) as compared with the grid pattern. Further increasing the porosity might result in larger deformations but will also reduce the stiffness of the panels.

Parametric study on two-ply strips

Two-ply specimens with a length of 30 mm were 3D printed from PLA (color: silver) to study the effects of dimensions (thickness, width) on their final shape. The printing patterns of the top and bottom plies are schematically shown in Figure S4a. The thickness of both plies was equal. Activation was done at 95 °C for at least 2 min to make sure the activation process was complete. One end of each specimen was fixed using a gripper and the free boundary was provided by a weak connection between the self-bending specimen and the fixed end. Marking the specimen with black dots allowed us to use image processing techniques for tracking the changes in the radius of curvature during the experiment.

Experimentally determined changes in the radius of curvature of one of the specimens is plotted in Figure S4b. The other specimens exhibited similar trends of deformation with the main difference being in their onset time, t_0, and minimum radius of curvature, r_{min}. Both thickness and width of the specimens significantly influenced the

shape-shifting of the two-ply specimens (Figure S4c). The results show radii of curvature in the range of 4.3 mm – 14.9 mm. The slender specimens (width = 5-10 mm) showed a 2-fold increase in their radius of curvature by increasing the thickness from 1.5 mm to 3 mm. Increasing the width from 5 mm to 10 mm did not change the results. Further increasing the width to 15 mm resulted in a 30% - 100% increase in the radius of curvature, dependent on the thickness.

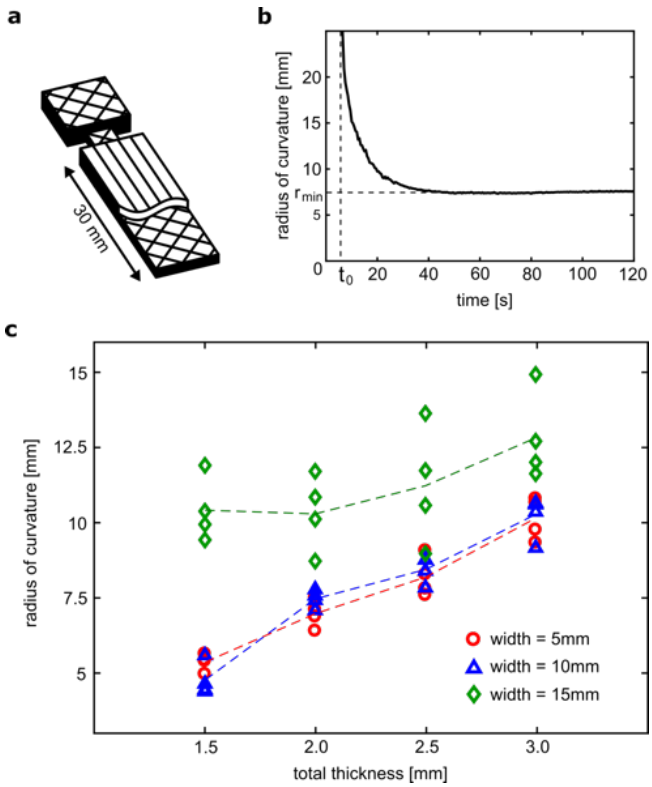

Figure S4
(a) Schematic representation of the two-ply specimen. A cut-out of the top layer is made to show the printing pattern of the bottom ply. (b) A sample curve representative of the tested specimens showing the change in the radius of curvature with time. The onset time of bending is denoted by t_0 and the minimum radius of curvature is denoted by r_{min}. (c) Experimental results show the radius of curvature of two-ply specimens with different sizes. Four specimens from each configuration were tested.

Increasing both the thickness and width of the two-ply strips resulted in larger radii of curvature after activation. According to the Timoshenko's bilayer bending model, the radius of curvature increases linearly as the thickness increases[35]. Fitting this linear relation between the radius and thickness to the experimental data showed that

the experiments are in good agreement with the model for slender specimens (R^2 = 0.99 and R^2 = 0.97 for widths of 5 mm and 10 mm, respectively). By further increasing the width to 15 mm, the edge effects, which are not captured by the Timoshenko's bilayer model, started to become more prominent. The Poisson's effect causes the difference in the longitudinal strains of the top and bottom plies to be accompanied with an opposite difference in the transverse strains of both plies, resulting in the transverse bending of the two-ply strips. This double curvature increases the bending moment of inertia in the longitudinal direction, thereby increasing the radius of curvature.

Shape-shifting of cellular structures

Cellular 2D structures were printed from PLA (color: magenta) using the standard printing settings. All specimens were produced with an edge thickness of 3.2 mm and a height of 7.5 mm. Two mechanisms of shape-shifting in the cellular structure were used to program both 2D to 2D and 3D to 3D shape-shifting. Printing of a 5×1 square array was performed with filament extrusion along the edge to program reduction in the edge length or in transverse direction to program increase in the edge length (Figure S5a). The programmed expansion and shrinkage of the edges results in the bending of the structure. Alternative to programming the change in the length of the edges, bending of the edges can be programmed by printing an expanding and shrinking strip side-by-side in one edge. This method is illustrated by a 3 x 3 array which shows pattern transformation from rectangular cells to hour-glass-shaped cells (Figure S5b). Expansion of a 2×2 cellular structure is achieved by straightening some initially curved edges using the same method (Figure S5c). 3D to 3D shape-shifting is illustrated with a cellular cubic structure made through manual assembly of 2D cellular unit-cells, which shows volumetric expansion upon activation (Figure S5d). Both the 5×1 and 3×3 square arrays were activated at 95 °C while other cellular structures were activated at 85 °C to avoid excessive deformations. Movies capturing the shape-shifting of the cellular structures were recorded and can be found as electronic supplementary material.

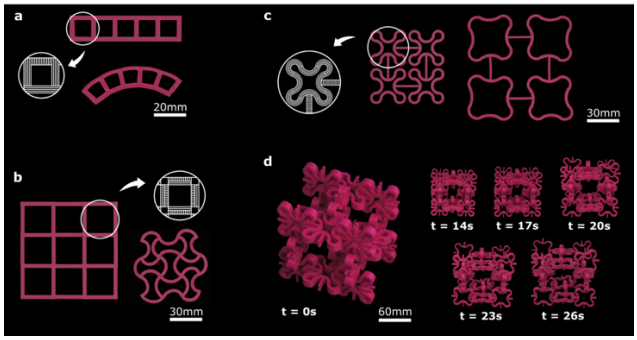

Figure S5
2D to 2D and 3D to 3D shape-shifting of cellular structures. (a) Bending of a 5×1 square array upon activation (supplementary video 11). (b) Pattern transformation from a 3×3 square array to a 3×3 hourglass-shaped array (supplementary video 12). (c) A 2×2 expanding cellular structure (supplementary video 13). (d) The volumetric expansion of an assembly of 20 expanding unit-cells (supplementary video 14). Unit-cells with the same printing patterns as the expanding structure (Figure S5c) were used.

Printing and activation parameters

Table S1
The printing parameters and activation conditions which were used for production and activation of the designs presented in this work.

Structure	Figure	Printing speed [mm/s]	Nozzle temperature [°C]	Layer height [μm]	Activation temperature [°C]
Box	2a	60	210	100	95
Dodecahedron	2b	60	210	100	95
Miura-ori	2c	60	210	100	95
DNA	3a	60	210	100	95
Pyramid	3b	60	210	100	95
Saddle	3c	60	210	100	95
Boat	3d	60	210	100	95
4 pyramids	3e	60	210	100	95
Bending strip	3f	60	195	50	95
Twisting strip	3g	60	195	50	95
Mimosa pudica	4a	60	210	100	90
Tulip	4b	60	210	100	90
5 x 1 array	S5a	60	210	100	95
3 x 3 array	S5b	60	210	100	95
2 x 2 array	S5c	60	210	100	85
3Dcellular structure	S5d	60	210	100	85

Chapter 9
Concluding remarks

Overview

With the main purpose of presenting guidelines for designing advanced engineering materials, this thesis was focused on rationality in the design of specific types of functional materials. Geometrical design of soft mechanical metamaterials and origami-based designs were presented as some examples of applicable strategies. The thesis was organized in two parts namely '***Soft cellular materials***' and '***From flat shapes to 3D geometries***'. While the proposed approaches have clear applications in the design of biomaterials and implants, there are numerous other areas where they could be of value.

In the first part, the main focus was on how instability could be harnessed to create materials with advanced functionalities. Tuning the instability behavior of the designed cellular materials is crucial for unlocking the world of possibilities that these materials offer. In particular, it is important to be able to adjust the thresholds and patterns of instability. We therefore explored a number of design strategies that could help in tuning the instability behavior of cellular materials. We started off by numerically exploring a wide range of symmetric 2D void shapes and determined how they affected their associated patterns of instability (i.e., critical strains and buckling modes, **chapter 2**). We found that while the geometry determines the critical strain, the total stiffness and, thus, critical stress could be adjusted independently. In the next step (**chapter 3**), the effects of the spatial distribution of material properties on the instability behavior of cellular materials were examined. Multi-material 3D printing (additive manufacturing) based on photopolymerization of liquid polymers was used to fabricate specimens with soft and stiff elements. The results of the study indicated that the spatial distribution of material properties could substantially change the instability thresholds in 2D soft mechanical metamaterials. Computational analysis showed that combining the spatial distribution of material properties with geometry not only allows for adjusting the onset of instability within wider ranges, but could also be used to change the instability mode (e.g., from symmetric compaction to side-buckling). Power-law relationships between the critical strain and total stiffness of the cellular structures on the one hand and the ratio of the material properties of the soft and stiff phases on the other hand (ranging from 0.1 to 10) were observed. The concepts of geometrical and multi-material design of soft mechanical metamaterials were then expanded to 3D cellular structures (**chapter 4**). A new class of soft mechanical metamaterials were introduced as buckling-driven soft actuators that are actuated through uniaxial compression. The 3D cellular structures were designed based on the projection of 2D void shapes into the 6 orthogonal tangential planes of spheres. BCC arrangement of porous balls formed the 3D structure of the soft actuators. The structures were split into ligament and connector elements with different material properties. Experiments and simulations revealed that while the

geometry plays a major role in determining the instability patterns, the spatial distribution of material properties could greatly enhance the tunability of these cellular materials. The new design of cellular materials also gave rise to a new mode of buckling, namely double-side buckling. Finally, we proposed a general approach for reliable activation of the higher modes of instability without any need for additional boundary conditions. In this approach, computational models were used to predict the shapes of those higher modes of instability. The calculated mode shapes were then introduced to the geometry of the cellular materials as imperfections. The magnitude of the introduced imperfections could be used to adjust the instability behavior of the resulting cellular structures. The advantages of this approach were demonstrated by designing a rotating actuator that reliably actuates its third instability mode. This unprecedented freedom in tuning the instability behavior of mechanical metamaterials is promising for fabrication of complex compliant systems with many potential applications in soft robotics and medical devices. The final chapter (**chapter 5**) of the first part of this thesis dealt with shape morphing. We showed how simple arrangement of auxetic (re-entrant) and conventional (honeycomb) unit cells could be used to enable arbitrary shape morphing. Upon stretching, the designed cellular structures morphed the arbitrary shapes defined by random Fourier's series as well as the shapes of a number of real-world objects.

The second part of this thesis was focused on creating 3D geometries from flat sheets. This is a novel approach for designing metamaterials that combine surface-related functionalities with the functionalities originating from the 3D geometry of the metamaterial. Starting from a flat shape allows for full access to the surface of what will ultimately become the metamaterial. Surface (bio-)functionalization therefore becomes possible. In the first chapter of this part (**chapter 6**), strategies were proposed for folding lattice structures from flat sheets taking the thickness of flat material into account. Three well-known space-filling polyhedra (i.e., cubic, truncated octahedron, and rhombic dodecahedron) were chosen to show-case the capabilities of the proposed folding strategies. These practical folding strategies pave the way for scalable real-world application of origami lattices with free-form surface ornaments. As demonstrated here, the surface ornaments may be created using currently available technologies such as electron beam induced deposition and micro-machining. Moreover, we showed how mechanical metamaterials such as auxetics could be folded from flat sheers using the proposed folding strategies simply by changing the dihedral angel of truncated octahedron. We also demonstrated the sequential self-folding of some of the proposed lattices. However, the self-folding demonstrated here is limited to macro-scale. Other approaches may be needed to extend this to micro- and nano-scales.

Both following chapters focused on shape shifting and self-folding, thereby providing some basis for some of the alternative techniques that could be used for self-folding of

regular polyhedral shapes from flat surfaces. In the first chapter (**chapter 7**), a simple approach (i.e., combination of active and passive polymers) was employed to program simple modes of deformation in bi- and multi-layer flat materials. Basic forms of shape transformation (e.g., rolling and twisting) were achieved by combining active and passive layers and using anisotropic strain recovery in active layers. It was shown that complex shape-shifting recipes could be realized by proper arrangement of the basic shape shifting elements in the structure of a flat material. Several examples such as pattern transformation in cellular structures and self-folding of origami structures were presented as possible examples of programmed shape shifting in soft matter. Moreover, experiments were conducted to evaluate the effects of geometrical parameters such as the thickness of the passive layer and the width of bilayer strips on the radius of curvature and the pitch size in self-rolling and self-twisting specimens. The geometrical parameters were found to remarkably influence the shape shifting behavior and the final shape of the material. Using UV-curable photopolymers, we also showed how the surface of the shape shifting materials could be decorated with arbitrarily complex patterns.

In the last chapter of the second part (**chapter 8**), a single-step 3D printing technique was proposed for programming shape shifting in flat materials. The main advantages of the proposed approach are its simplicity and versatility. Fused deposition modeling is perhaps the cheapest and most widely available 3D printing technique, while the material used in the study (i.e., polylactic acid) is biocompatible, ubiquitous, and extremely inexpensive. Once triggered by external stimuli (i.e., high temperatures), printed shape memory filaments tend to shrink longitudinally and expand radially. A range of possible strain recoveries from anisotropic shrinkage (up to 27 percent) to semi-passive response was achieved by using different patterns (orientation) of material printing (filament deposition). The effects of parameters such as nozzle temperature, layer height, and activation temperature on the level of anisotropic shrinkage were experimentally studied to evaluate the achievable range of strain recovery in single-ply panels. Differently programmed plies were combined to create the basic modes of shape shifting. The basic active elements and (semi-) passive elements were then used to create more complex shape shifting. Examples included Miura-ori origami and a number of polyhedral geometries. Additionally, internal stresses were used to create buckling and, thus, out-of-plane shape shifting. To overcome the blockages of origami structures during the process of self-folding, sequential folding was introduced. The required time delays in the shape transformations were introduced using porosity as the major factor that controls heat transfer trough the thickness of the polymeric designs. Sequential folding was then demonstrated in the leaves of Mimosa pudica and in a tulip-like structure that folded from a flat 3D printed sheet.

Potential applications

Both cellular and origami-based metamaterials studied here have numerous applications in various areas of engineering and medicine. As for the cellular materials, soft robotics in general and soft actuators in particular are among the most important areas of potential applications. These applications are emphasized in chapter 5, where the ultra-tunability of the actuation behavior of these structures is discussed. Soft actuators based on cellular material could have applications also in the development of wearable robotics, as their looks and feels are not too far from fabrics. In the same line of applications, soft cellular materials may find applications in exoskeleton and exo-suits used for human mobility augmentation. Shape-morphing and buckling-driven metamaterials could be also useful for the design of (low-force) precision grippers, for robotic assisted surgery, or for design of consumer products (e.g., fashion products).

The applications of origami-based designs are numerous as well. In this thesis, development of meta-biomaterials that combine functionalities originating from the surface with those rooted in the 3D geometry were extensively discussed. However, there are many more areas where such combinations of functionalities could be useful including devices that incorporate controllers, sensors, actuators, antennas, and other types of electronics. In general, many technologies developed since the mid 20th century have been limited to planar constructs (i.e. flat substrates). Transforming the shape of flat constructs to 3D allows for direct integration of already available technologies into advanced materials and devices. This encompasses many types of technologies (e.g., microarray printing) and various types of industries from consumer products to high-tech industry. Other applications such as smart packaging could be also envisaged for shape shifting and shape morphing metamaterials.

In general, both cellular and origami-based design approaches may serve as guidelines for designing variety of advanced materials with particular functionalities. The proposed approaches tie the physical and mechanical functionalities that can lead to multifunctional metamaterials with tunable properties. For instance, a material can be passively programmed to switch its physical properties raising from its periodic design based on the deformation patterns in their structures. While multi-material additive manufacturing makes the fabrication of soft and rigid elements in one structure possible, advanced 4D printing techniques may help us to produce high-tech products as they enable one to include stimuli-responsive elements and electronics inside the structure of soft matter.

Future directions

Regarding the soft cellular materials, two major fronts for future research include extending the tunability of their behavior and evaluating their structural performance

under repetitive mechanical loading (i.e., fatigue behavior). Moreover, actual designs employing these structures in real-world applications are expected in the coming years and will be the ultimate test for their potential.

As for origami-based designs, extending the self-folding techniques to smaller scales (i.e., micro- and nano-scales) remains to be challenging, as many of the already existing techniques either do not work at those scales or are difficult to precisely control. Expanding the range of the geometries that could be folded from flat sheets is another important challenge. Finally, the fabrications techniques should be upscaled to enable the production of folded metamaterials at a level (i.e., magnitude, speed, cost) that is practical for real-world applications.

Summary

Nature is full of materials that exhibit astonishing properties that are not available in engineering materials. The study of the underlying structure of such materials has revealed that geometry plays an important role in achieving such properties. Unusual physical and mechanical properties such as structural coloring in butterfly wings and shock absorption in woodpecker skull are examples of how geometry could be used for functionalization of materials. At the same time, recent advancements in (additive) manufacturing techniques have enabled us to fabricate engineering materials whose ultrastructure is geometrically very complex. It is therefore now possible to design engineering materials with unusual properties. In this dissertation, two types of geometrical designs are used for development of mechanical metamaterials with unusual properties. That includes 1. Cellular structures working on the basis of mechanical instability, and 2. Origami-based designs. The dissertation has been organized in two parts each covering one of the above-mentioned design types.

In the first part, soft cellular materials with tunable instability behavior are presented. We use computational modeling and experiments to study how geometrical design and the spatial distribution of material properties could be exploited to tune the instability behavior of such mechanical metamaterials. The effects of a wide range of geometrical designs on the onset of instability, instability pattern (mode), and instability force are studied. In the first step, we show that geometrical design could be used to adjust the critical strain independently from mechanical properties of bulk material. In the next step, the effects of the spatial distribution of material properties on the critical behavior of 2D soft mechanical metamaterials are studied. We found that that spatial distribution of mechanical properties could substantially change the thresholds of instability in 2D soft mechanical metamaterials. Furthermore, we show that combining the multi-material designs with geometry may also change the instability mode (buckling mode). In the third step, the concepts of geometrical and multi-material design were expanded to 3D cellular structures. We propose a new class of ultra-tunable buckling-driven soft actuators working on the basis of mechanical instability. To include the concept of multi material design, the structures are split into ligament and connector elements. Experimental and computational analyses indicate that while the geometry plays a major role in determining the instability patterns, the spatial distribution of material properties could greatly enhance the tunability of these cellular materials. In addition, we proposed a general approach to reliably activate the higher modes of instability in soft mechanical metamaterials. In this approach, the higher modes of instability in soft actuators could be activated when geometrical imperfections from first order buckling analysis has been introduced into the geometry of the cellular structure. We found that the magnitude of the introduced imperfections could be used to adjust the instability

behavior of the resulting cellular structures. To demonstrate the power of this approach, a rotating actuator that reliably actuate its third instability mode was fabricated. In the final step, we show how simple arrangement of auxetic and conventional unit cells could be used to design shape-morphing 2D structures that morph the shape of real objects upon stretching.

In the second part, we propose origami as a strategy that could be used to fabricate 3D porous structures from flat geometries. The benefit of this approach is that the flat geometry could be initially functionalized using the existing nanopatterning techniques such as nanolithography to guide stem cell fate and kill bacteria. We present strategies for folding complex lattices from space-filling polyhedra such as cubic, truncated octahedron, and rhombic dodecahedron. We also demonstrate how this could be used to fold mechanical metamaterials (e.g., auxetic). An important aspect of such origami-based designs is self-folding. We therefore present two approaches for programing self-folding in flat materials. The first approach is based on combining active and passive polymers in different ways. We show that complex shape shifting recipes could be realized by proper arrangement of basic shape-shifting elements in the structure of the flat material. In the second approach, we propose a single-step 3D printing technique for programming shape shifting in flat materials. The presented technique works with inexpensive fused deposition modeling printers and the most widely available 3D printing material (i.e. polylactic acid). We demonstrate how different combinations of 3D printed plies could be used for programming complex shape shifting using either active-passive combinations or the out-of-plane buckling approach. Finally, we demonstrate the incorporation of time delays in the shape transformations using heat-transfer principles, thereby giving rise to sequential shape shifting.

Samenvatting

De natuur herbergt tal van materialen met uitzonderlijke eigenschappen die niet gebruikelijk zijn in technische materialen. Door de onderliggende structuur van deze materialen te bestuderen wordt duidelijk dat geometrie een belangrijk rol speelt in het verwezenlijken van dit soort bijzondere eigenschappen. Ongewone fysische en mechanische eigenschappen zoals structurele kleurvorming in vlindervleugels en schokdemping in de schedel van de specht zijn voorbeelden van hoe geometrie gebruikt kan worden om extra functionaliteiten toe te voegen aan de materialen. Tegelijk hebben recente vooruitgangen in (additieve) productietechnieken het mogelijk gemaakt om technische materialen te vervaardigen met een hele complexe onderliggende structuur. Bijgevolg is het nu mogelijk om technische materialen te ontwerpen met ongewone eigenschappen. In dit proefschrift worden twee types geometrische ontwerpen gebruikt voor de ontwikkeling van mechanische metamaterialen met ongebruikelijke eigenschappen: ten eerste cellulaire structuren die gebruik maken van mechanische instabiliteit en ten tweede op origami gebaseerde ontwerpen. Dit proefschrift is bijgevolg opgedeeld in twee delen waarin elkeen van de bovengenoemde ontwerpen behandeld worden.

In het eerste deel worden zachte cellulaire materialen met aanpasbaar instabiliteitsgedrag voorgesteld. We gebruiken computermodellen en experimenten om te bestuderen hoe het geometrisch ontwerp en de ruimtelijke verdeling van materiaaleigenschappen geëxploiteerd kunnen worden om het instabiliteitsgedrag van dit soort mechanische metamaterialen aan te passen. De effecten van een breed scala aan geometrische ontwerpen op de start van instabiliteit, het instabiliteitspatroon (modus), en de instabiliteitskracht worden onderzocht. In de eerste stap tonen we aan dat het geometrische ontwerp gebruikt kan worden om de kritieke rek aan te passen, onafhankelijk van de mechanische eigenschappen van het bulkmateriaal. In de volgende stap worden de effecten van de ruimtelijke verdeling van materiaaleigenschappen op het kritieke gedrag van 2D zachte mechanische metamaterialen bestudeerd. We observeren dat de ruimtelijke verdeling van de mechanische eigenschappen substantieel de aanvang van instabiliteit kan veranderen in 2D zachte mechanische metamaterialen. Vervolgens tonen we aan dat de combinatie van multi-materiaal ontwerp met geometrie ook de instabiliteitsmodus kan veranderen. In de derde stap worden de concepten van geometrisch en multi-materiaal ontwerp uitgebreid naar 3D cellulaire structuren. We stellen een nieuwe klasse van extreem aanpasbare, door knik aangestuurde, zachte actuators voor. Om het multi-materiaal concept toe te passen worden de structuren opgesplitst in ligamenten en verbindingselementen. Ondanks het feit dat geometrie een belangrijke rol speelt in het bepalen van de instabiliteitspatronen tonen experimentele en computeranalyses aan dat de ruimtelijke verdeling van materiaaleigenschappen de

aanpasbaarheid van deze cellulaire materialen erg kunnen versterken. Bovendien stellen we een algemene methode voor om op betrouwbare wijze de hogere instabiliteitsmodi in zachte mechanische metamaterialen te activeren. In deze methode kunnen de hogere instabiliteitsmodi geactiveerd worden wanneer geometrische imperfecties van de eerste orde knikanalyse geïntroduceerd worden in de geometrie van de cellulaire structuur. We observeren dat de grootte van de geïntroduceerde imperfecties gebruikt kan worden om het instabiliteitsgedrag van de resulterende cellulaire structuren aan te passen. Om deze methode te illustreren werd een roterende actuator gefabriceerd waarbij de derde instabiliteitsmodus geactiveerd wordt. In de laatste stap tonen we aan hoe een simpele schikking van auxetische en conventionele eenheidscellen gebruikt kan worden om vorm-veranderende 2D structuren te ontwerpen die zich aanpassen naar de vorm van reële objecten wanneer ze uitgerekt worden.

In het tweede deel stellen we origami voor als een strategie om 3D, poreuze structuren te fabriceren uit vlakke geometrieën. Het voordeel van deze methode is dat de vlakke geometrie eerst van functionaliteit voorzien kan worden met behulp van bestaande nanotechnieken zoals nanolithografie om het gedrag van stamcellen te beïnvloeden en bacteriën te doden. We presenteren strategieën voor het vouwen van complexe roosterstructuren van ruimtevullende polyhedra zoals de kubus, de afgeknotte octaëder en de rhombische dodecaëder. We tonen ook aan hoe dit gebruikt kan worden voor het vouwen van mechanische metamaterialen (bijv. auxetisch). Belangrijk bij zo'n op origami gebaseerd ontwerp is het zelfvouwende aspect. We stellen daarom twee methodes voor om het zelfvouwen te programmeren in vlakke materialen. De eerste methode is gebaseerd op het op verschillende manieren combineren van actieve en passieve polymeren. We tonen aan dat complexe vormveranderingen gerealiseerd kunnen worden door de specifieke schikking van basis vormveranderende elementen in de structuur van het vlakke materiaal. In de tweede methode stellen we een 3D-print techniek voor om vormverandering in vlakke materialen te programmeren in een enkele productie stap. De voorgestelde techniek werkt met goedkope "fused deposition modeling" printers en het meest voorkomende 3D-print materiaal (i.e. polymelkzuur). We tonen aan hoe verschillende combinaties van 3D geprinte lagen gebruikt kunnen worden voor het programmeren van complexe vormveranderingen met ofwel een actieve-passieve combinatie ofwel door middel van knik uit het vlak. Tenslotte tonen we aan hoe vertragingen in de vormverandering verwerkt kunnen worden door middel van warmteoverdracht principes, wat leidt tot tijdsafhankelijke vormverandering.

Acknowledgment

This thesis is the collection of a series of studies published during my PhD research. All these studies are the results of brainstorming meetings and vivid discussions I had with my promoter Prof. Amir A. Zadpoor. I would like to thank him for all his support and encouragement. It was indeed not possible for me to complete this project without his excellent guidance and involvement.

I would also like to thank Prof. Harrie Weinans for his support, guidance and critical feedbacks. I would like to thank Prof. Kees Hagen and Dr. Lidy Fratila-Apachitei for their support and involvement in the project of origami lattices. I would like to thank Sander for his technical support and all the colleagues at Materials Science Lab and technical workshops. I am very thankful of our department managers Dineke and Mirjam and the secretary team Sabrina, Anouk, Angelique, Nancy, Hanneke and Karin for providing all the supports during the last five years.

I would also like to thank Vahid, Saber, Mohammad Ahmadi, Sina, Nazli, Gianni, Reza, Teunis, Francoise, Ingmar, Sebastien, Mohammad Mirzaali, Budi, Yageng, Eline, Mahya, Mahdieh, Khashayar, Marike, and all my colleagues at the department of biomechanical engineering and all my dear friends at 3ME for sharing enjoyable time during the last five years.

I would like to thank Elham, Mohammad and daei Abdol for their friendship and kindness which started from when we arrived in the Netherlands and has continued till now.

Finally, I must express my gratitude to my wife Mehranoosh for her support and patience during last years. Mehranoosh, thank you for your love and caring about family. Tina and Tania thank you for making our life more beautiful and meaningful.

Shahram
Delft, October 2018